Towards the Extension of the Substrate Spectrum of the [Fe]-Hydrogenase Hmd

Dissertation

zur Erlangung des Grades eines

Doktor der Naturwissenschaften

(Dr. rer.nat.)

des Fachbereichs Biologie der Philipps-Universität Marburg

Vorgelegt von

Manuel Gehl

Aus Merzig

Marburg, 2023

Die vorliegende Dissertation wurde von August 2019 bis Mai 2023 am Max-Planck-Institut für terrestrische Mikrobiologie in der Abteilung „Microbial Protein Structure“ unter Leitung von Dr. Seigo Shima angefertigt.

Vom Fachbereich Biologie der Philipps-Universität Marburg (Hochschulkennziffer 1180) als Dissertation angenommen am: 23.05.2023

Erstgutachter: Dr. Seigo Shima

Zweitgutachter: Prof. Dr. Tobias Erb

Weitere Mitglieder der Prüfungskommission:

Prof. Dr. Lennart Randau

Prof. Dr. Annette Borchers

Tag der Disputation: 25.07.2023

Table of contents

Abstract

In hydrogenotrophic methanogenesis, methenyl-tetrahydromethanopterin (methenyl-H_4MPT^+) is sequentially reduced to methylene-H_4MPT and methyl-H_4MPT. The H_2-forming methylene-H_4MPT dehydrogenase Hmd catalyzes the reduction of methenyl-H_4MPT^+ to methylene-H_4MPT using H_2 as electron donor. The reduction of methylene-H_4MPT to methyl-H_4MPT is catalyzed by the F_{420}-dependent methylene-H_4MPT reductase Mer using reduced F_{420} ($F_{420}H_2$) as electron donor. Despite the very similar structure of the H_4MPT derivatives and the fact that Hmd can bind methylene-H_4MPT and generate H_2 by oxidation of the methylene group, Hmd is unable to reduce methylene-H_4MPT. The question that arises is what are the structural features that allow Hmd to reduce only methenyl-H_4MPT^+ but not methylene-H_4MPT. To this end, the catalytic mechanism of Hmd was first investigated to determine whether the H_2 activation reaction requires the presence of methenyl-H_4MPT^+. In collaboration with researchers at the MPI Göttingen, an NMR method based on the parahydrogen induced polarization (PHIP) effect was applied to study the trajectories of H_2, hydrides and protons during the catalytic cycle of Hmd. For the first time, significant PHIP-NMR signals of H_2 and hydride binding to Hmd were obtained, supporting the proposed catalytic mechanism that does not involve the methenyl group in hydride formation. Following this finding, the catalytic mechanism of Mer and the flavin-independent methylene-tetrahydrofolate reductase Mfr, which catalyzes the analogous reduction of methylene-tetrahydrofolate (methylene-H_4F) to methyl-H_4F, was investigated. Mer from *Methanocaldococcus jannaschii* (jMer) and Mfr from *Mycolicibacterium hassiacum* (hMfr) were heterologously produced in *Escherichia coli* and the crystal structures of the apoenzymes of jMer and hMfr as well as the binary complex of jMer with F_{420} were solved. Since no ternary complex of jMer or hMfr including the C_1 carrier and reducing agent could be obtained, a functional alignment approach was used to derive information on the geometry of the ternary complex. The structure of jMer complexed with F_{420} was aligned with the published ternary complex structure of the FAD-dependent methylene-H_4F reductase from *E. coli* (eMTHFR) in such a way that the proteins were first manually aligned using the hydride-carrying atoms of the electron carriers as a fixed point. In a second step, the apoenzyme structure of hMfr was incorporated into the model by manually aligning it with the structure of eMTHFR. Amino acids found at equivalent positions in all three reductases were mutated to investigate their putative function. The mutational analysis indicated that although eMTHFR, hMfr and jMer share a limited degree of sequence identity, the active site amino acid residues and their

geometries are very similar and may serve the same function. Furthermore, a glutamate was found as the key catalytic residue at the equivalent position in all three enzymes, suggesting that they share a common catalytic mechanism, which involves the formation of a 5-iminium cation intermediate. This knowledge was used to construct a docking model of hMfr in complex with NADH and methylene-H_4F. A phylogenetic analysis indicated that the three reductases do not share a common ancestor and the conserved active site structures of the three reductases may be the result of divergent evolution. Through this series of studies, it was suggested that if the active site of Hmd could be modified to carry out the desired protonation of methylene-H_4MPT, it would be possible to construct an Hmd mutant capable of reducing methylene-H_4MPT to methyl-H_4MPT using H_2. Some possible mutations to form such a methylene-H_4MPT-reducing Hmd are suggested.

Zusammenfassung

Bei der hydrogenotrophen Methanogenese wird Methenyl-tetrahydromethanopterin (Methenyl-H_4MPT^+) nacheinander zu Methylen-H_4MPT und Methyl-H_4MPT reduziert. Die H_2-bildende Methylen-H_4MPT-Dehydrogenase Hmd katalysiert die Reduktion von Methenyl-H_4MPT^+ zu Methylen-H_4MPT unter Verwendung von H_2 als Elektronendonor. Die Reduktion von Methylen-H_4MPT zu Methyl-H_4MPT wird von einem anderen Enzym katalysiert, der F_{420}-abhängigen Methylen-H_4MPT-Reduktase Mer, die reduziertes F_{420} ($F_{420}H_2$) als Elektronendonor verwendet. Trotz der sehr ähnlichen Struktur der H_4MPT-Derivate und der Tatsache, dass Hmd Methylen-H_4MPT binden und durch Oxidation der Methylengruppe H_2 erzeugen kann, ist Hmd nicht in der Lage, Methylen-H_4MPT zu reduzieren. Es stellt sich die Frage nach den strukturellen Merkmalen, die es Hmd ermöglichen, nur Methenyl-H_4MPT^+ zu reduzieren. Zu diesem Zweck wurde zunächst der katalytische Mechanismus von Hmd untersucht, um festzustellen, ob die H_2-Aktivierungsreaktion die Anwesenheit von Methenyl-H_4MPT^+ erfordert. In Zusammenarbeit mit Forschern des MPI Göttingen wurde eine NMR-Methode angewandt, die auf dem parahydrogen induced polarization (PHIP)-Effekt basiert, um die Trajektorien von H_2, Hydriden und Protonen während des katalytischen Zyklus von Hmd zu untersuchen. Zum ersten Mal wurden signifikante PHIP-NMR-Signale für die Bindung von H_2 und Hydrid an Hmd erhalten, die den vorgeschlagenen katalytischen Mechanismus unterstützen, bei dem die Methenylgruppe nicht an der Hydridbildung beteiligt ist. Daraufhin wurde der katalytische Mechanismus von Mer und der Flavin-unabhängigen Methylen-Tetrahydrofolat-Reduktase Mfr, die die analoge Reduktion von Methylen-Tetrahydrofolat (Methylen-H_4F) zu Methyl-H_4F katalysiert, untersucht. Zu diesem Zweck wurden Mer aus *Methanocaldococcus jannaschii* (jMer) und Mfr aus *Mycolicibacterium hassiacum* (hMfr) heterolog in *Escherichia coli* produziert und die Kristallstrukturen der Apoenzyme und des binären Komplexes von jMer mit F_{420} gelöst. Da kein ternärer Komplex von jMer oder hMfr einschließlich des C_1-Trägers und des Reduktionsmittels erhalten werden konnte, wurde ein funktioneller Alignment-Ansatz verwendet, um Informationen über die Geometrie des ternären Komplexes zu erhalten. Dazu wurde die Struktur von jMer im Komplex mit F_{420} mit der veröffentlichten ternären Komplexstruktur der FAD-abhängigen Methylen-H_4F-Reduktase aus *E. coli* (eMTHFR) so ausgerichtet, dass die Proteine zunächst manuell an den Hydrid-tragenden Atomen der Elektronenträger als Fixpunkt ausgerichtet wurden. In einem zweiten Schritt wurde die Apoenzymstruktur von hMfr in das Modell aufgenommen, indem sie manuell an der Struktur von eMTHFR ausgerichtet wurde. Aminosäuren, die in allen drei Reduktasen an

äquivalenten Positionen gefunden wurden, wurden mutiert, um ihre mutmaßliche Funktion zu untersuchen. Die Mutationsanalyse ergab, dass eMTHFR, hMfr und jMer zwar nur ein begrenztes Maß an Sequenzidentität aufweisen, die Aminosäurereste im aktiven Zentrum und ihre Geometrien jedoch sehr ähnlich sind und möglicherweise dieselbe Funktion erfüllen. Darüber hinaus findet sich in allen drei Enzymen ein Glutamat als katalytischer Schlüsselrest an der entsprechenden Position, was darauf hindeutet, dass sie einen gemeinsamen katalytischen Mechanismus haben, der die Bildung eines 5-Iminiumkation-Zwischenprodukts beinhaltet. Dieses Wissen wurde genutzt, um ein Docking-Modell von hMfr im Komplex mit NADH und Methylen-H_4F zu erstellen. Eine phylogenetische Analyse ergab, dass die drei Reduktasen keinen gemeinsamen Vorfahren haben und die konservierten Strukturen des aktiven Zentrums der drei Reduktasen das Ergebnis einer divergenten Evolution sein könnten. Aus dieser Reihe von Studien ging hervor, dass es möglich wäre, eine Hmd-Mutante zu konstruieren, die in der Lage ist, Methylen-H_4MPT mit Hilfe von H_2 zu Methyl-H_4MPT zu reduzieren, wenn das aktive Zentrum von Hmd so verändert werden könnte, dass es die gewünschte Protonierung von Methylen-H_4MPT durchführt. Es werden einige mögliche Mutationen zur Bildung eines solchen Methylen-H_4MPT-reduzierenden Hmd vorgeschlagen.

Publications

Parts of the studies presented in this thesis have been published, are in preparation, or have been submitted for publication:

Gehl, M, Demmer, U., Ermler, U., Shima, S. (2023). Crystal structure of FAD-independent methylene-tetrahydrofolate reductase from *Mycobacterium hassiacum*. *Proteins*. 2023; 1-12.

Kaltschnee, L., Pravdivtsev A., **Gehl, M.**, Huang, G., Stoychev, G., Riplinger, C., Neese, F., Keitel, M., Hövener, J., Auer, A., Griesinger, C., Shima, S., Glöggler, S. (2023). Hydrogen intermediates of active [Fe]-hydrogenase catalysis detected by sensitivity-enhanced NMR. (Under review).

Gehl, M., Demmer, U., Ermler, U., Shima, S. A common catalytic mechanism for methylene-tetrahydropterine reductases. (In preparation).

Awards

Winner of the Best Scientific Presentation Award at the Gordon Research Seminar on Molecular Basis of Microbial One-Carbon Metabolism (07 August 2022 in Southbridge, MA, USA): "*Iminium Ion Hypothesis - How Different Reductases Share One Common Catalytic Mechanism*". This award gave me the opportunity to give an oral presentation at the Gordon Research Conference on Molecular Basis of Microbial One-Carbon Metabolism (11 August 2022 in Southbridge, MA, USA).

Winner of the Best Presentation Award at the retreat of the International Max Planck Research School for Environmental, Cellular and Molecular Microbiology (27-29 March 2023 in Vogelsbergdorf, Hesse, Germany): "*The Iminium Cation Hypothesis: How Different Reductases Share one Common Catalytic Mechanism*"

Introduction

Hydrogenotrophic methanogenesis and the reduction of bound carbon units

Methanogens are a diverse group of anaerobic microorganisms that produce methane through primary metabolism. They are found exclusively in the domain of archaea and are responsible for an estimated 70% of global methane emissions (*1*). Methanogenic archaea occur in habitats with low levels of electron acceptors such as molecular oxygen, nitrate, iron(III) and sulfate (*2*). They can be divided into acetoclastic, methylotrophic and hydrogenotrophic methanogens based on their substrate (*3*). Acetoclastic methanogens split acetate produced by fermentative anaerobes into CO_2 and CH_4 (*4*). Methylotrophic methanogens grow on various methylated compounds such as methanol and methylamines, and recently methanogens capable of growing on methoxylated aromatic compounds have been described (*5*–*7*). Hydrogenotrophic methanogenesis is based on the reduction of one molecule of CO_2 by the oxidation of four molecules of H_2 and is equivalent to chemical methanation, also known as the Sabatier process (*8*, *9*):

$$CO_2 + 4\,H_2 \rightleftharpoons CH_4 + 2\,H_2O \quad \Delta G^{0\prime} = -131\ kJ/mol$$

One of the key features of the methanogenic pathway is the fixation of CO_2 and the stepwise reduction of the bound carbon unit (C_1 unit) as transition from a formyl to a methyl group involving several intermediates. A similar pattern of C_1 reduction can be observed in many organisms (Figure 1A and B). This allows the transformation of C_1 units from oxidation states of formic acid (+II, methenyl group) to formaldehyde (0, methylene group) to methanol (-II, methyl group) without the functional groups of these compounds (*10*, *11*). Specialized C_1 carriers are required for this purpose. In nature, two C_1 carriers in particular have evolved, which use a reduced pterin to bind the C_1 units and can therefore be called tetrahydropterin carriers. Methanogenic, methylotrophic and sulfate-reducing archaea utilize tetrahydromethanopterin (H_4MPT) as a C_1 carrier, whereas in most bacteria and eukaryotes the main C_1 carrier is tetrahydrofolate (H_4F) (*12*). However, this demarcation is not strict. For example, the methylotrophic bacterium *Methylobacterium extorquens* AM1 contains H_4MPT (*13*), and in the methanogenic archaeon *Methanosarcina barkeri* H_4F-specific enzymes have been found (*14*). Both C_1 carriers consist of tetrahydropterins, a *para*-aminobenzoate (PABA) ring and a tail region attached to the ring. The N5 and/or N10 of the tetrahydropterins carry the respective C_1 units. The main structural differences are found in the tail region. H_4F has a

variable number of glutamate residues attached to the PABA ring, whereas H_4MPT has a ribitol residue attached to a ribose-5-phosphate group linked to a hydroxyglutarate (Figure 1C and D) (*12*). The most important functional difference is the carbonyl group adjacent to the PABA ring in H_4F, which is absent in H_4MPT. This electron withdrawing group results in a lower electron density at N10 of H_4F, leading to increased electrophilicity. This effect is transmitted to the bound C_1 units resulting in a more positive redox potential of the H_4F derivatives compared to the corresponding H_4MPT derivatives (*12*). In contrast to the striking structural similarities, both the C_1 carriers and the underlying reduction patterns are thought to have evolved separately (*15*). This is reflected in the enormous diversity of physiological functions of this pathway (*12*). In heterotrophic, eukaryotic organisms, including humans, the pathway is used for anabolic purposes. C_1 units are most commonly introduced by the conversion of serine to glycine, yielding methylene-H_4F. This compound is then interconverted into various H_4F derivatives, which are used for biosynthesis. For example, thymidine monophosphate and α-oxopantoate are synthesized from methylene-H_4F, purine synthesis is dependent on N10-formyl-H_4F and methionine and S-adenosylmethionine are synthesized from methyl-H_4F (*12*). In CO_2-fixing acetogenic bacteria, the C_1 reduction pathway is also known as the methyl branch of the Wood-Ljungdahl pathway and is involved in catabolism. The methyl group of methyl-H_4F is used for the synthesis of acetyl-CoA, which links catabolism to anabolism (*16*). In methanogenesis, the pathway is also involved in catabolism and, analogous to acetogenic bacteria, methyl-H_4MPT is used to synthesize acetyl-CoA, which is required for biomass formation (*17*). Depending on the methanogenic species, fluxes are directed towards the oxidation of C_1 units or towards the reduction of C_1 units, as in hydrogenotrophic methanogenesis (*4–6*).

In the initial reaction of hydrogenotrophic methanogenesis, a formylmethanofuran dehydrogenase Fwd/Fmd reduces and fixes CO_2 as a formyl group bound to the C_1 carrier methanofuran using reduced ferredoxin as electron donor (*18*, *19*) (Figure 1A). The formyl group of formyl-methanofuran is then transferred to the main C_1 carrier H_4MPT to form formyl-H_4MPT, which is then condensed to methenyl-H_4MPT$^+$ (*20*, *21*). The second reduction step is the reduction of the methenyl group to a methylene group. This reaction can be catalyzed by two different enzymes: the F_{420}-dependent methylene-H_4MPT dehydrogenase Mtd or the H_2-forming methylene-H_4MPT dehydrogenase Hmd, which is a [Fe]-hydrogenase. Hmd uses a hydride derived directly from H_2 while Mtd uses $F_{420}H_2$ as reducing agent (*22*, *23*). F_{420} is a deazaflavin structurally similar to FAD, but unlike FAD where the redox active atom is N5, the redox active atom in F_{420} is a carbon. This makes F_{420} an obligate hydride carrier that can only accept or donate two electrons in the form of a hydride H^- (*24*). Reduced $F_{420}H_2$ is produced by

the F_{420}-reducing [NiFe]-hydrogenase Frh (*25–27*). In the subsequent reduction step, the F_{420}-dependent methylene-H_4MPT reductase Mer reduces methyl-H_4MPT (*28*). The methyl group is then transferred to the thiol cofactor coenzyme M (CoM-SH) in an energy-conserving reaction. The corresponding enzyme, methyl-H_4MPT:coenzyme M methyltransferase Mtr, couples the exergonic methyl transfer to the efflux of Na^+ cations trough the cytoplasmic membrane (*29*). This Na^+ gradient is used by an ATP synthase to generate ATP (*30*). The resulting methyl-CoM is then the substrate for the methyl-CoM reductase Mcr, which catalyzes the final reduction step of the C_1 unit in the pathway. In the Mcr reaction, the methyl group of methyl-CoM is reduced to CH_4 using reduced coenzyme B (CoB-SH). The so-called heterodisulfide CoM-S-S-CoB is hereby formed as a by-product (*31*). To recycle CoM-SH and CoB-SH, hydrogenotrophic methanogens have evolved an energy-coupling step to couple the exergonic reduction of CoM-S-S-CoB with the endergonic reduction of the low-potential redox carrier ferredoxin. A multi-enzyme complex formed by the [NiFe]-hydrogenase Mvh and the heterodisulfide reductase Hdr uses flavin-based electron bifurcation to split two molecules of H_2 into four electrons (*32*, *33*). Two electrons are transferred to the heterodisulfide and two electrons to ferredoxins. These ferredoxins are used to fix a molecule of CO_2 in the first step of the pathway (*34*). Taken together, the pathway consists of several hydrogenases that oxidize H_2 to drive anaerobic respiration. One of these hydrogenases, Hmd, has attracted particular interest because it transfers a hydride directly to the organic substrate, rather than extracting electrons from H_2 like all other known hydrogenases (*35*).

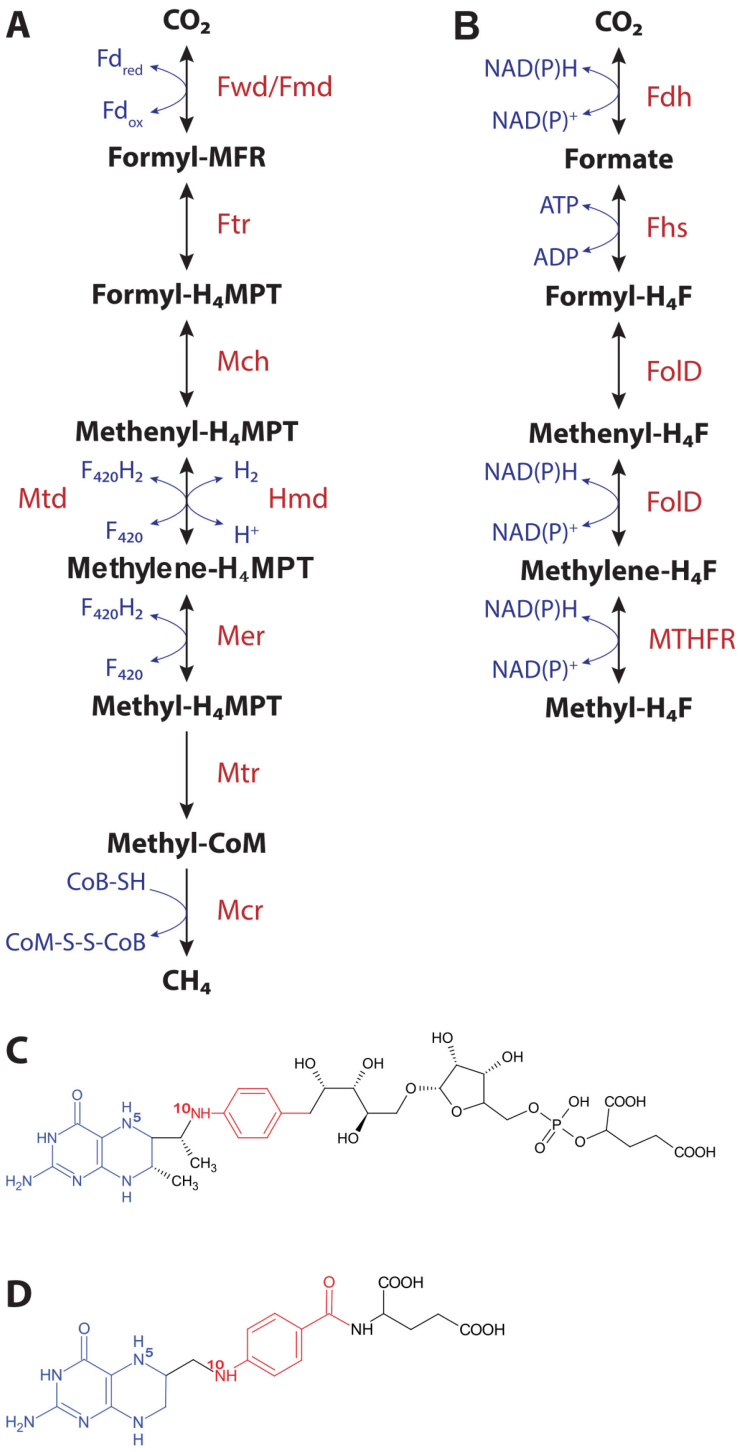

Figure 1: **(A)** Schematic representation of the fate of fixed carbon in methanogenesis. Enzymes involved are shown in red and reducing agents in blue. **(B)** Schematic representation of the analogous reduction of C_1 units bound to H_4F. Not all steps occur in every organism and the source of C_1 units varies. Enzymes involved are shown in red and reducing agents in blue. In acetogens, CO2 is reduced to formate by a formate dehydrogenase (Fdh), and formate is then converted to N10-formyl-H_4F by a formyl-H_4F synthetase (Fhs) at the expense of one ATP. FolD is a bifunctional enzyme found in most organisms that converts N10-formyl-H_4F to methylene-H_4F. The analogous reaction to the Mer reaction is carried out by methylene-tetrahydrofolate reductases (MTHFR) using NAD(P)H as a reducing agent. **(C)** Structure of H_4MPT. **(D)** Structure of H_4F. The pterin ring system is colored blue and the para-aminobenzoate (PABA) group is colored red.

The [Fe]-hydrogenase Hmd carries out one reduction step

Hmd catalyzes the heterolytic cleavage of H_2 and the stereospecific hydride transfer to C14a of methenyl-H_4MPT$^+$. The reaction is reversible, so that Hmd can also oxidize methylene-H_4MPT to methenyl-H_4MPT$^+$ with simultaneous formation of H_2 (Figure 2A) (*36*, *37*). The physiological role of Hmd is postulated to replace the [NiFe]-hydrogenase Frh in conditions where nickel is not readily available. In this case, Hmd reduces methenyl-H_4MPT$^+$ and the resulting methylene-H_4MPT is oxidized by the F_{420}-dependent methylene-H_4MPT dehydrogenase Mtd with concomitant reduction of F_{420} (*38*, *39*). The catalytic activity of Hmd is based on its unique iron cofactor, the iron-guanylylpyridinol (FeGP) cofactor (Figure 2B). This molecule consists of a low-spin iron coordinated to the guanylylpyridinol via a nitrogen and an acyl ligand. In addition, two carbon monoxide ligands are coordinated to the iron and a thiol derived from an essential cysteine of the protein part occupies the fifth coordination site. In the resting state, the sixth coordination site is occupied by a water molecule and is thought to be replaced by H_2 prior to catalysis (*40–44*).

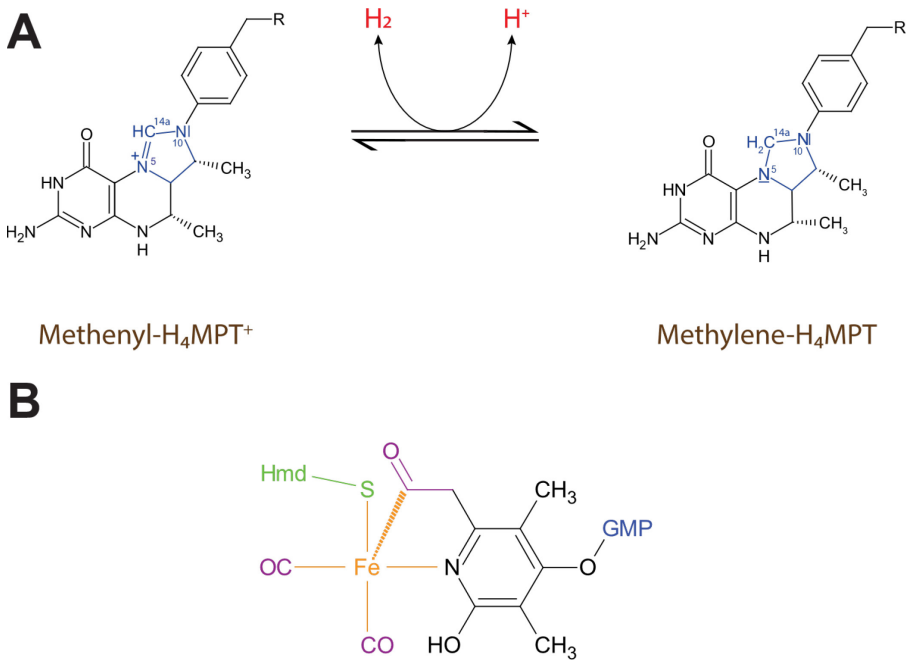

Figure 2: **(A)** Reaction catalyzed by Hmd. Hmd catalyzes a reversible heterolytic cleavage of H_2 with subsequent hydride transfer to the C14a of methenyl-H_4MPT$^+$. The imidazoline ring containing the C14a is colored blue. **(B)** Structure of the FeGP cofactor. The cofactor consists of an organic guanylylpyridinol moiety ligated to the central Fe ion by an acyl and a nitrogen bond. Two CO ligands and a thiolate of Hmd are coordinated and the sixth coordination site is occupied by a water molecule in the resting state (not shown) and is thought to be the H_2 binding site during catalysis.

The catalytic mechanism of Hmd is not fully understood and two different mechanistic models have been postulated. The first catalytic mechanism was proposed based on the dependence of H_2/H^+ and para/ortho-H_2 exchange reactions on the presence of methenyl-H_4MPT^+ (*23*, *45*). When Hmd was discovered, the existence of the FeGP cofactor was unknown. Therefore, the first proposed catalytic mechanism does not take into account the metal cofactor and considers the activation of methenyl-H_4MPT^+ rather than H_2 as the key step (Figure 3A). The imidazoline ring of methenyl-H_4MPT^+ in solution is flattened and therefore unable to react with H_2. Hmd must modulate the conformation of the substrate to activate it for H_2 cleavage. In the activated conformation, the electrophilicity of the cation at C14a should be greatly enhanced, allowing it to abstract a hydride from H_2 with the help of an acidic function in the enzyme (*46–48*). Similar reactions are observed in organic chemistry for the reversible formation of alkanes in superacidic solution involving carbocations (*49*). This scenario implies two necessary characteristics. Firstly, the substrate must be a carbocation and secondly, Hmd must be very specific to methenyl-H_4MPT^+ in order to activate the substrate.

Following the discovery of the FeGP cofactor, analyses of several crystal structures of Hmd (*41*, *50*), an inactive Hmd mutant (*40*), and an Hmd inhibitor complex (*51*) helped to suggest an alternative mechanism. Recently, atomic resolution structures of the binary complex of Hmd with the FeGP cofactor and the ternary complex of Hmd with the FeGP cofactor and methenyl-H_4MPT^+ were solved (*41*). The two complexes exhibited two different protein conformations. While the binary complex without substrate was found in an open conformation, the ternary complex was found in a closed conformation. In the open conformation, the sixth coordination site of FeGP was occupied by a water molecule which was absent in the closed conformation, suggesting that the movement upon binding of methenyl-H_4MPT^+ is responsible for the exclusion of this water molecule and that this site is probably the H_2 binding site (Figure 3B) (*41*). In the closed conformation, the 2-hydroxy group of the FeGP cofactor is deprotonated, resulting in a negatively charged 2-O^- ion. H_2 binds to the open coordination site of the FeGP cofactor and H_2 is cleaved into a hydride H^- and a proton H^+, with the 2-O^- ion acting as a catalytic base. The proton is transiently accepted by the hydroxyl ion and the hydride is transferred to C14a of methenyl-H_4MPT^+, resulting in the formation of methylene-H_4MPT. In the final step, the protein conformation is opened and a water molecule replaces methylene-H_4MPT (*41*). Another interesting feature found in the crystal structure is that the N5-C14a bond length of 1.23 Å does not support the presence of a carbocation as proposed for the first mechanism. Thus, the experimental data provide a clearer picture of the catalytic mechanism of Hmd. (*41*). However, several crucial questions regarding the catalytic mechanism remain

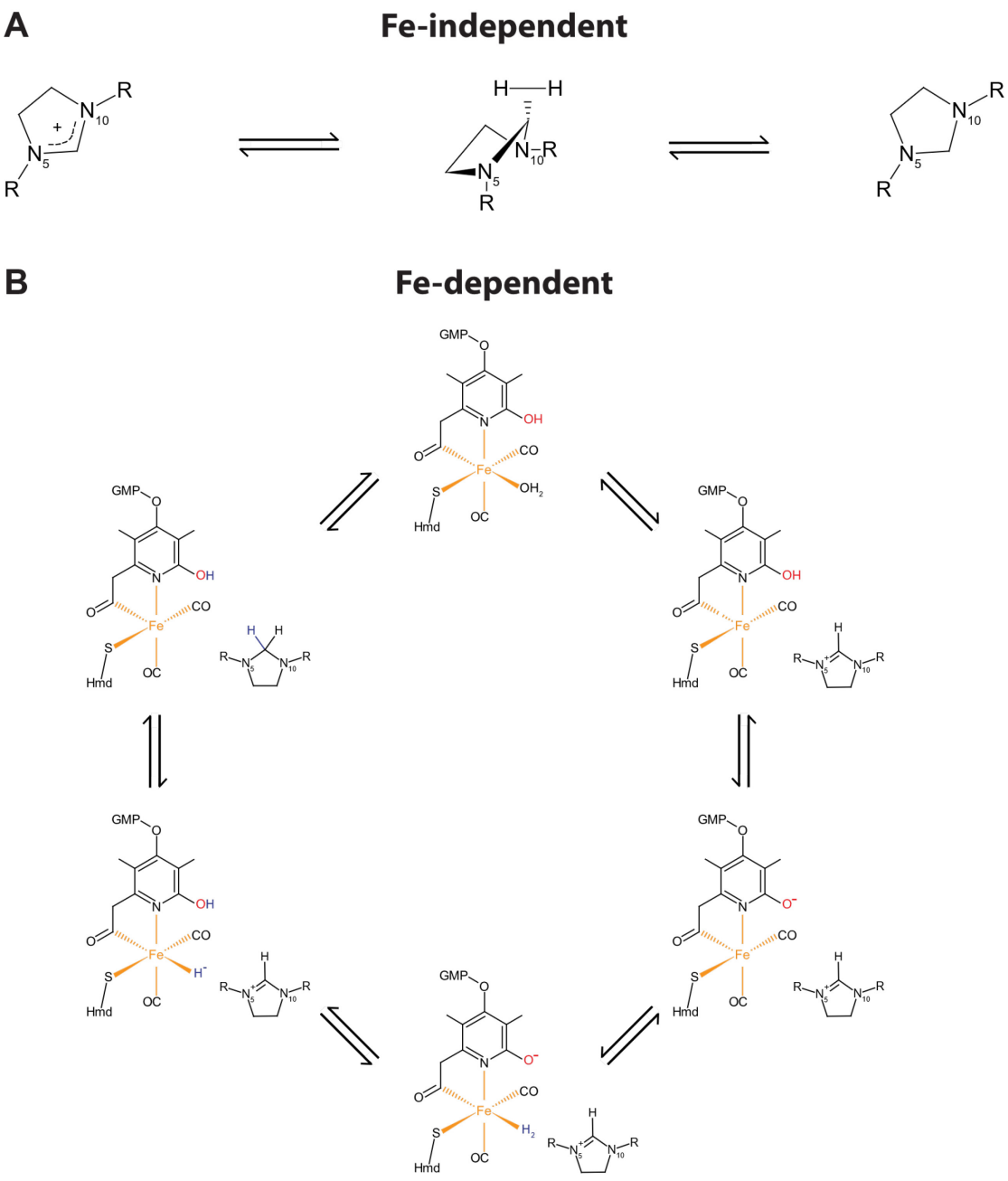

Figure 3: Comparison of the different proposed catalytic mechanisms of Hmd. **(A)** The Fe-independent catalytic mechanism. In the first step the carbocationic methenyl-H_4MPT^+ has to be distorted and destabilized. In this envelope conformation the electrophilicity should be increased to a point where molecular hydrogen can bind and a hydride is abstracted by the C14a atom. Hence, in this scenario catalytic species and hydride acceptor are both methenyl-H_4MPT^+. **(B)** The Fe-dependent catalytic mechanism. Binding of methenyl-H_4MPT^+ induces a transition from open to closed protein conformation, while H_2O is removed. The 2-hydroxyl group of the FeGP cofactor (colored red) is deprotonated and act as a proposed catalytic base. After binding of H_2 (colored blue) to the Fe site, H_2 is cleaved to H^- and H^+, the latter of which is transiently accepted by the deprotonated 2-hydroxyl group, and H^- is transferred to the C14a position of methenyl-H_4MPT^+. In this scenario, H_2 is activated at the Fe and the deprotonated carboxyl group rather than at methenyl-H_4MPT^+.

unanswered. In the proposed catalytic mechanism, the open site of the iron complex is postulated as the H_2 activation center, but the interaction of H_2 or a hydride with the iron site has not been experimentally demonstrated. There are two possible catalytic bases, the thiolate of the FeGP-binding cysteine and the 2-hydroxy group of the pyridinol, but it is not known which one actually functions as the catalytic base.

One question that the proposed catalytic mechanisms cannot answer is why Hmd is not capable of a second reduction step that reduces methylene-H_4MPT to methyl-H_4MPT. This question is based on three observations. First, Hmd binds methylene-H_4MPT to oxidize the substrate in the reverse direction (*37*). This eliminates the inability to accept methylene-H_4MPT as a substrate. Secondly, there are no theoretical thermodynamic constraints. The standard redox potential ($\Delta E^{0'}$) of the methenyl-H_4MPT$^+$/methylene-H_4MPT pair is –390 mV and that of the methylene-H_4MPT/methyl-H_4MPT pair is –320 mV (*3*). Consequently, the reduction of both methenyl-H_4MPT$^+$ and methylene-H_4MPT by splitting H_2 ($\Delta E^{0'}$ = –414 mV) (*3*) is thermodynamically favorable, and the reduction of methylene-H_4MPT is more favorable than that of methenyl-H_4MPT$^+$. Third, the redox reactions of methenyl/methylene-H_4MPT and methylene/methyl-H_4MPT are very similar. In both reactions a hydride is added to either a methenyl group part of an imidazoline ring or a methylene group part of an imidazolidine ring (*36*, *52*, *53*). Therefore, the question arises whether Hmd has evolved a mechanistic feature that actively suppresses the second reduction step or whether some other chemical reason prevents this reaction. The reduction of methylene-H_4MPT is actually already present in the methanogenic pathway. After reduction of methenyl- to methylene-H_4MPT, the methylene group is further reduced by the F_{420}-dependent methylene-H_4MPT reductase Mer (Figure 1A) (*28*).

The catalytic mechanism of the F_{420}-dependent methylene-H_4MPT reductase

Mer is involved not only in the C_1 unit reduction pathway of methanogenic archaea, but also in the methyl group oxidation of methanotrophic and sulfate-reducing archaea, where it catalyzes the reversible reduction of methylene-H_4MPT using $F_{420}H_2$ as reductant (Figure 4) (*54*, *55*). A study has also reported that Mer from *Methanocaldococcus jannaschii* is involved in the reduction of methylglyoxal (*56*). Over the decades, Mer proteins from *Archaeoglobus fulgidus* (*54*), *Methanopyrus kandleri* (*57*), *Methanosarcina barkeri* (*28*), *Methanothermobacter marburgensis* (*58*) and *Methanothermobacter thermautotrophicus* (*59*)

have been purified from the corresponding organism. Heterologous expression in *Escherichia coli* was unsuccessfully attempted (*60*) until 2017, when Miller et al. reported soluble expression of Mer from *M. jannaschii* (jMer) (*56*). All these Mer enzymes have been extensively characterized, showing that Mer does not contain a chromophoric prosthetic group and catalyzes the reduction of methylene-H_4MPT by a ternary complex mechanism. All Mer enzymes are cytosolic and oxygen stable. The reaction does not proceed with other electron donors such as FAD, FMN, NADH, NAPH or single electron donors (*28*, *54*, *57–59*). Only Mer from *M. thermautotrophicus* has been reported to exhibit 16% of its native activity using the F_{420} fragment F^+ (*59*), which lacks the γ-polyglutamate tail (*61*). Size-exclusion chromatography indicated that Mer forms different oligomeric states of 35 kDa monomers depending on the organism. Mer from *A. fulgidus* forms a homopentamer (*54*), Mer from *M. kandleri* forms a homooctamer (*57*), Mer from *M. thermautotrophicum* (*59*, *62*), *M. barkeri* (*28*) and *M. marburgensis* (*58*) form a homotetramer and Mer from *M. jannaschii* (*56*) forms a homodimer. Since Mer is also involved in the oxidation of methyl groups, it is not surprising that the catalyzed reaction is to some extent reversible. However, since the free energy change of the reduction of methylene-H_4MPT is −5.2 kJ/mol, the oxidation of methyl-H_4MPT only proceeds completely in the presence of Mtd or Hmd, which oxidize methylene-H_4MPT to methenyl-H_4MPT$^+$ (*59*).

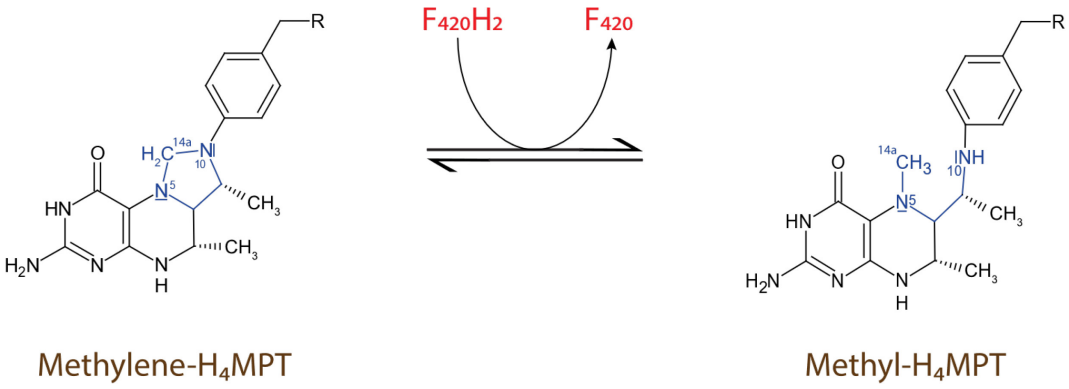

Figure 4: Reaction catalyzed by the F_{420}-dependent methylene-H_4MPT reductase Mer. Mer transfers a hydride derived from reduced F_{420} to the C14a position of methylene-H_4MPT to produce methyl-H_4MPT.

The crystal structures of the Mer apoenzymes from *M. kandleri* and *M. marburgensis* (*55*) and the F_{420}-containing binary complex of Mer from *M. barkeri* (*52*) have been solved. Mer has a characteristic $(\beta\alpha)_8$ or so-called TIM barrel fold, formed by eight parallel β-strands

surrounded by eight α-helices (*63*). Based on sequence motifs and structural classification, Mer belongs to the superfamily of bacterial luciferases or luciferase-like hydride transferases (LLHT), which consists of FMN- and F_{420}-dependent oxidoreductases (*64–66*). Other exemplary members are FMN-dependent luciferases (LuxAB), FMN-dependent alkanesulfonate monooxygenases (SsuD), F_{420}-dependent alcohol dehydrogenases (Adf) and F_{420}-dependent glucose-6-phosphate dehydrogenases (FGD). An exhaustive list is shown in Table S4. Another notable feature of Mer is a non-prolyl *cis*-peptide (NPCP) bond adjacent to the *Re*-site of F_{420} (*52*, *55*). These *cis*-peptide bonds are very rare because they greatly restrict conformational space (*67*, *68*). Approximately 0.3% of all bonds are *cis*-peptide bonds, of which only 13% are NPCP bonds. In particular, they occur close to active sites or are related to the function of the enzyme (*69*). In Mer the NPCP bond presumably acts as a backstop and is thought to be essential for the correct placement of F_{420} in the active site (*52*). Notably, this NPCP bond is not a common feature of all members of the bacterial luciferase superfamily and has only been found in the structures of Mer (*52*, *55*), LuxA (*70*), Adf (*71*) and FGD (*72*). Crystal structures of other members clearly show the absence of such an NPCP bond (*73–77*). The F_{420} molecule found in the binary complex of Mer from *M. barkeri* has a curved so-called butterfly conformation (*52*), which is typical of flavins. It has been shown that the N5-N10 axis in oxidized and reduced flavins is flexible and that both semiquinones and fully reduced flavins tend to form this butterfly conformation (*78*, *79*). Enzymes were postulated to manipulate the biochemical properties of flavins by stabilizing either the bent or planar conformation (*80*). There is no such evidence for the deazaflavin F_{420}, and since F_{420} is unable to form semiquinone forms, it acts more like nicotinamide cofactors (*81*). However, F_{420} is found in the butterfly conformation in all known F_{420}-containing crystal structures of bacterial luciferase superfamily members and in most structures of unrelated F_{420}-dependent enzymes (*52*, *71*, *72*, *82*, *83*).

It has not yet been possible to obtain a ternary complex structure of Mer with F_{420} and either methylene- or methyl-H_4MPT, or to perform mutation experiments to establish a catalytic scenario. It is therefore of great interest to look at enzymes that catalyze similar reactions. Fortunately, an analogous reaction occurs in many organisms, namely the reduction of methylene-H_4F to methyl-H_4F (*12*) (Figure 1B).

Methylene-tetrahydrofolate reductases catalyze a similar reaction to Mer

The similar reduction of methylene-H_4F to methyl-H_4F is catalyzed by a class of enzymes called methylene-H_4F reductases (MTHFRs) (*11*). This class can be subdivided into several groups and it is currently debated whether this classification is complete and how the different subgroups are distributed in different lineages of organisms. As many of these subgroups have only recently been discovered and most of them do not yet have a clearly assigned function, there is still no universally valid classification (*84*, *85*). For this work, MTHFR enzymes are divided into two classes based on the presence of flavin as a cofactor (Figure 5). While there is only one type of flavin-independent MTHFR (Mfr) (*86*, *87*), the flavin-dependent MTHFRs can be further divided into subclasses depending on whether they carry FAD or FMN as a prosthetic group (*84*, *88–91*). The FMN-dependent MTHFRs include the 2S-, 3S- and 6S-types according to the number of subunits in the complexes (*85*).

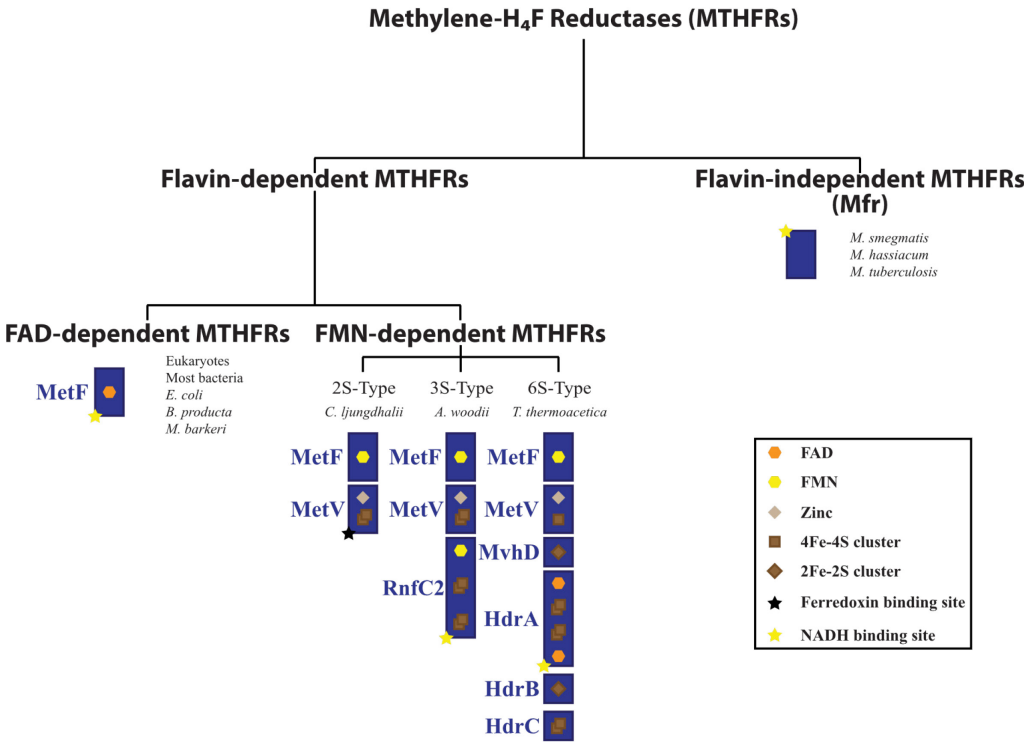

Figure 5: Classification scheme for methylene-H_4F reductases (MTHFRs). Based on the absence or presence of flavin cofactors, MTHFRs can be divided into two classes of which the flavin-dependent MTHFRs can be further subdivided dependent on the harboring flavin species. The classification scheme is based purely on physical aspects and does not represent any evolutionary relationships.

The FAD-dependent MTHFR was identified in 1961 and has attracted much attention because defects in the human MTHFR gene are the most common congenital disorder of folate metabolism (*92*, *93*). The folate cycle consists of the interconversion of the tetrahydrofolate derivatives formyl-H_4F, methenyl-H_4F, methylene-H_4F and unsubstituted H_4F (*11*, *16*). The folate cycle is linked to the methionine cycle via MTHFR and the cobalamin-dependent enzyme methionine synthase. MTHFR is responsible for reducing methylene-H_4F to methyl-H_4F, which is the primary circulating form of folate in the human body and the predominant form used for DNA synthesis. The methionine synthase transfers the methyl group of methyl-H_4F to homocysteine to form methionine (*94*). Methionine is then used for anabolic purposes, but also to produce S-adenosylmethionine (SAM), an important substrate for radical SAM reactions and methyl donor for several methylation reactions in the cell (*95*, *96*). The product of the methylation reactions, S-adenosylhomocysteine, is finally converted to homocysteine, which completes the methionine cycle (*97*). Defects in MTHFR are linked to a wide range of conditions, including vascular disease, depression, spontaneous pregnancy loss, chronic kidney disease, schizophrenia and neural tube defects (*97–108*)

MTHFR has a ping-pong reaction mechanism, which is different from the ternary complex mechanism of Mer (*52*, *109*) (Figure 6). The tightly bound FAD acts as a prosthetic group for MTHFR. In the reductive half-reaction, NAD(P)H reduces FAD and in the oxidative half-reaction, $FADH_2$ reduces methylene-H_4F (*109*). It has also been shown that MTHFR is in principle able to oxidize methyl-H_4F, effectively reversing the reductive half-reaction (*110*). However, the overall reaction *in vivo* is considered irreversible due to an standard free energy change of –21.6 kJ/mol and a high intracellular NADH/NAD^+ ratio (*11*, *111*). Evidence was found that the catalytic mechanism of MTHFR involves the formation of an iminium cation. Since the imidazolidine ring in methylene-H_4F is a poor acceptor for the negatively charged hydride, it was suggested that the substrate must first be activated to an iminium cation to accept the hydride (*112*). This process is similar to the chemical condensation of formaldehyde and H_4F to form methylene-H_4F (*113*). Moreover, in the crystal structure of the methylene-H_4F-utilizing enzyme thymidylate synthase, a hydroxymethylene-tetrahydrofolate molecule was found which is formed by the reaction of the proposed iminium cation and water (*114*).

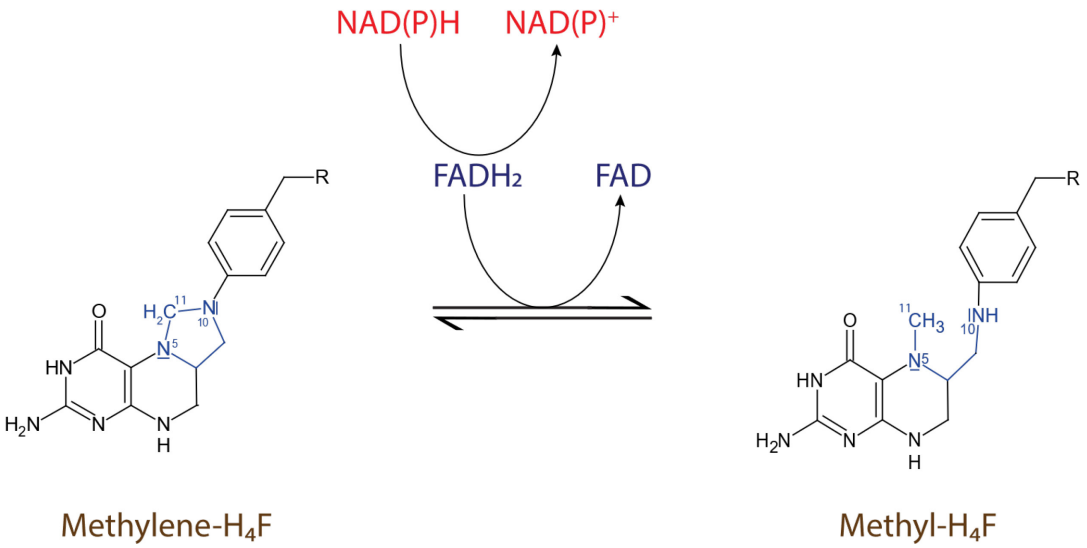

Figure 6: Reaction of the FAD-dependent methylene-H_4F reductase. This enzyme first reduces a non-covalently bound FAD using a hydride from NAD(P)H. In a second half reaction, the hydride is transferred from $FADH_2$ to C11 of methylene-H_4F to give methyl-H_4F.

The FAD-dependent MTHFR is the most common type of MTHFR and is widely found in eukaryotes and bacteria (*91*, *115–117*). While bacterial MTHFRs consist of a single catalytic domain, eukaryotic MTHFRs are extended by a regulatory domain. The regulatory domain binds S-adenosylhomocysteine and regulates MTHFR in a negative feedback loop (*110*, *118*, *119*). Several structures have been solved, including the structure of MTHFR from *E. coli* (eMTHFR) (*118*), *Haemophilus influenza* (PDB: 5UME), and *Neisseria meningitidis* (PDB: 7RML). The structures of MTHFR from *Saccharomyces cerevisiae* and *Homo sapiens* in complex with S-adenosylhomocysteine (*119*) and the structure of MTHFR from *Thermus thermophilus* in complex with the inhibitor formyl-H_4F were solved (*110*, *120*). Furthermore, the ternary complex of a Glu28Gln mutant of *E. coli* MTHFR with FAD and either NADH or methyl-H_4F was determined (*121*). The MTHFR structures showed that the catalytic domains of all enzymes are TIM barrel folds with the non-covalently bound FAD in the center of the barrel structure (*118*). The structures also explain why MTHFR has a ping-pong mechanism rather than a ternary complex mechanism. This is because NAD(P)H and methylene-H_4F bind to the same position (*121*). In the reductive half-reaction, NAD(P)H forms a four-layer sandwich, allowing the electron transfer to FAD. After $NAD(P)^+$ leaves the active site, methylene-H_4F binds to the same position, presumably undergoing protonation to form a positively charged iminium cation. This iminium cation is proposed to be the reactive species that accepts the hydride from $FADH_2$, ultimately forming methyl-H_4F in the oxidative half-

reaction of MTHFR. (*121*, *122*). Decades of research have led to a good understanding of the FAD-dependent MTHFR. In contrast, the FMN-dependent and flavin-independent MTHFR types are still poorly understood.

FMN-dependent MTHFRs are diverse multi-enzyme complexes found exclusively in acetogens (Figure 5). So far, however, only a small number of enzymes have been characterized. The MTHFR from *Clostridium ljungdahlii* consists of the FMN-harboring subunit MetF and the [4Fe-4S] cluster-harboring subunit MetV. The latter uses reduced ferredoxin as reducing agent to convert methylene-H_4F to methyl-H_4F *in vitro* (*85*), but this is probably not the physiological reaction (*84*). In *Acetobacterium woodii*, the MTHFR consists of MetF, MetV and RnfC2 and can reduce methylene-H_4F using NADH. Interestingly, the NADH binding site in this MetF is altered and NADH binds to RnfC2 (*88*). MTHFR from *Moorella thermoacetica* is a heterohexamer consisting of MetF, MetV, HdrA, HdrB, HdrC and MvhD. The complex catalyzes the reversible reduction of methylene-H_4F using the one-electron mediator benzyl viologen, and it also catalyzes the reduction of benzyl viologen by NADH, but the physiological activity is not known (*90*). It is noteworthy that the MTHFR from the acetogen *Blautia producta*, however, is an FAD-dependent and not an FMN-dependent MTHFR (*123*) and that the MTHFR from *Clostridium formicaceticum* was found to be a heterooctamer consisting of two different subunits and containing iron-sulfur-clusters and FAD rather than FMN (*89*). In summary, neither the physiological activity, the metabolic function nor the distribution of FMN-dependent MTHFRs in different organisms is fundamentally understood and their role remains elusive.

Flavin-independent MTHFRs (Mfr) are monomeric enzymes found only in mycobacteria. Homologs of the FAD-dependent MTHFR have not been annotated in most mycobacterial genomes (*124*). A first indication of the presence of Mfr was provided by structure modelling of a gene product from *Mycobacterium tuberculosis*. The modelled structure and the known *E. coli* MTHFR structure showed similarities (*124*). Recently, the enzymes encoded by *MSMEG_6596* and *MSMEG_6649* in *Mycobacterium smegmatis* were found to have MTHFR activity (*86*). Notably, both enzymes do not contain FAD or any other prosthetic group and therefore catalyze the reaction by a ternary complex mechanism (Figure 7). A knockout strain of *M. smegmatis* showed impaired growth in the absence of methionine, suggesting that the mycobacterial Mfr is also involved in the methionine cycle (*86*). Furthermore, the corresponding gene *Rv2172c* in *M. tuberculosis* was shown to be essential for the growth of the organism, as no colonies grew after knockout (*87*). Replacement of the native

gene with less active point mutants resulted in growth defects that could be rescued by exogenous methionine supply. Overexpression of *Rv2172c* increased resistance to the antitubercular drug para-aminosalicylic acid (*87*).

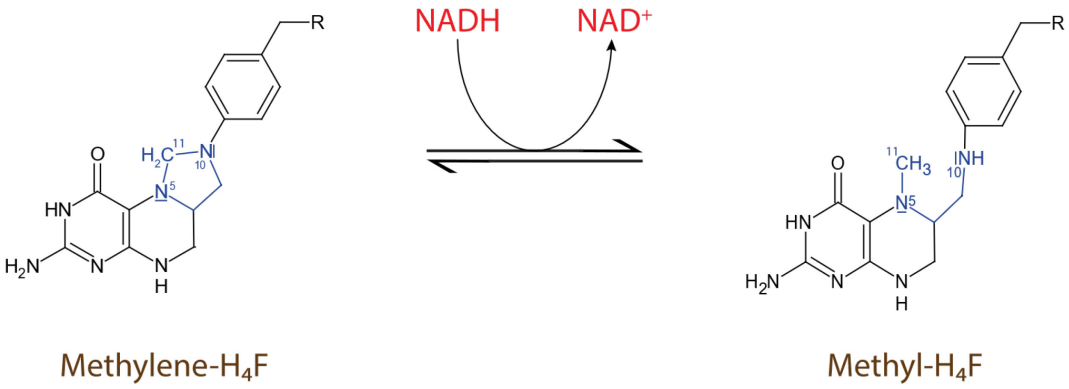

Figure 7: Reaction of the flavin-independent methylene-H_4F reductase Mfr. In contrast to the FAD-dependent MTHFR, this enzyme directly transfers a hydride derived from NADH to C11 of methylene-H_4F, resulting in the formation of methyl-H_4F.

The fact that the mycobacterial Mfr is fundamentally different from the human FAD-dependent MTHFR makes it an attractive enzyme for the development of anti-mycobacterial drugs. These are urgently needed given that an estimated one-third of the world's population is infected with tuberculosis and an estimated 10 million people developed tuberculosis in 2019 alone, with multi-drug resistant strains emerging (*125*, *126*).

Aim of this work

The aim of this work is to elucidate why Hmd is unable to reduce methylene-H_4MPT and to use this knowledge for the future construction of an Hmd mutant capable of reducing methylene-H_4MPT with H_2. The engineered Hmd enzyme will contribute to the future construction of a synthetic F_{420}-independent methanogenic pathway. The first step is to rule out the possibility that the methenyl group is a key element for the H_2 cleavage, as proposed in the first catalytic mechanism of Hmd. Although the catalytic mechanism of Hmd has been extensively studied in the past using infrared spectroscopy (*44*, *127*), Mössbauer spectroscopy (*42*), X-ray crystallography (*40*, *41*, *43*, *50*, *128*), X-ray absorption spectroscopy (*129*) and

classical NMR spectroscopy (*130*, *131*), crucial information on the fate of hydrogen atoms during catalysis and the function of the possible catalytic base is still lacking. Therefore, I was part of a multi-institute collaboration led by Dr. Lukas Kaltschnee, Dr. Christian Griesinger and Dr. Stefan Glöggler from the Max-Planck-Institute for Multidisciplinary Sciences in Göttingen. We developed a novel NMR method based on the so-called parahydrogen induced polarization (PHIP) effect and identified new intermediates in the catalytic cycle of Hmd and obtained valuable information about the trajectory of the hydride and protons during catalysis. The second step of the project is to find out how the catalytic mechanism of the F_{420}-dependent methylene-H_4MPT reductase Mer works and extract the information with the aim of constructing Hmd mutants capable of a second reduction step. This requires the ternary complex crystal structure of Mer. Since previous attempts to crystallize Mer in complex with F_{420} and a substrate were unsuccessful, the flavin-independent methylene-H_4F reductase Mfr is being used in parallel to crystallize the corresponding ternary complex. Based on the structural information, mutational experiments were performed to elucidate the catalytic mechanism of Mer and Mfr. This information is used to construct Hmd mutants that will be tested for their ability to reduce methylene-H_4MPT.

Results and Discussion

Parahydrogen-enhanced NMR studies of the Hmd catalytic cycle

Since the fate of H_2 during Hmd catalysis remains elusive, a novel nuclear magnetic resonance (NMR) method using parahydrogen (p-H_2) has been applied as part of a collaborative effort. p-H_2 is a spin isomer of H_2 in which the total nuclear spin is zero. "Normal" hydrogen (n-H_2) is a mixture of p-H_2 and orthohydrogen (o-H_2), which has a total nuclear spin of one (*132*). p-H_2 is not visible in NMR spectroscopy and can only be made visible by breaking the symmetry of the molecule. This symmetry break results in the so-called parahydrogen induced polarization (PHIP) effect, which is often accompanied by a strong signal enhancement (*132*, *133*). To test whether a PHIP effect occurs when Hmd catalyzes the reaction, reconstituted Hmd from *M. jannaschii* and methylene-H_4MPT were placed in an NMR tube. Methylene-H_4MPT was then converted to methenyl-H_4MPT^+ and the reaction was started by adding H_2.

Only p-H_2 in combination with Hmd and methylene-H_4MPT in deuterated buffer resulted in the appearance of two types of PHIP effects (Figure 8A). Using n-H_2 with Hmd and methylene-H_4MPT (Figure 8B) did not change the spectrum compared to n-H_2 with deuterated buffer only (Figure 8D). The negative control using p-H_2 and deuterated buffer only (Figure 8C) clearly shows that the reaction of Hmd is responsible for the observed change in spectrum. The first effect is called H_2-PHIP and manifests itself as an altered line shape in the enhanced H_2 signal. This type of PHIP effect has been described as partially negative line shape (PNL) and is based on the reversible binding of H_2 to a catalyst (*134*). The second effect, HD-PHIP, is seen as an enormous increase in intensity, resulting in a three-fold split HD signal.

Based on these PHIP experiments, together with chemical exchange saturation transfer (CEST) experiments on the PHIP signals (Figure S1), kinetic modelling and quantum chemical calculations, several conclusions can be drawn (Figure 9A). The PNL signal, resulting from the reversible binding of H_2 to the active site, suggests a hydride bound laterally to the Fe of the FeGP cofactor (*134*). Furthermore, a rapid exchange with solvent H_2 must occur to explain the resulting spectra. This implies that in the closed conformation of Hmd, H_2 reversibly binds to the Fe as a so-called non-classical hydride (or dihydrogen complex) and dissociates again (*135*). The HD-PHIP results from hydrogen isotope exchange with the solvent, as previously reported (*45*), which occurs at the 2-OH group of the FeGP cofactor (Figure 9B). Both H_2-PHIP and HD-PHIP can only be described with at least two different intermediate states, suggesting that

first the thiol linking FeGP to Hmd polarizes H_2 and then the 2-hydroxy group of the pyridinol ring is deprotonated. The latter acts as a stronger base and polarizes H_2, which is then cleaved into a classical terminal hydride (*135*).

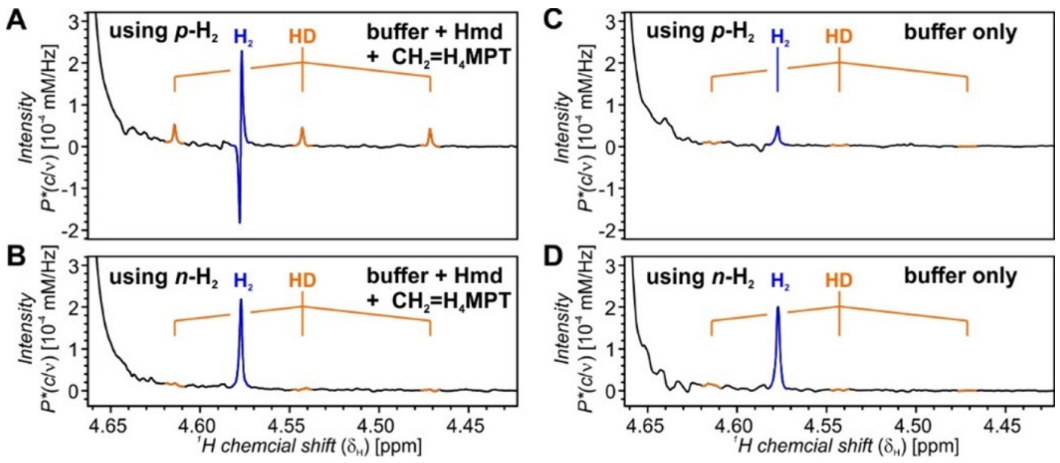

Figure 8: Occurrence of PHIP effects in the Hmd catalyzed reaction. **(A)** The use of parahydrogen in combination with methylene-H_4MPT (CH_2=H_4MPT) and Hmd results in two strong PHIP signals. The H_2-PHIP signal (blue) manifests as a PNL shape, while the HD-PHIP signal (orange) manifests as a tree-fold split signal. **(B)** "Normal" hydrogen does not promote PHIP signals in the presence of the Hmd reaction. **(C)** Negative control using only parahydrogen. The small signal in the H_2 region is due to orthohydrogen contamination. **(D)** Negative control using "normal" hydrogen and buffer only. Figure adapted from (*135*).

Taken together, these results extend the previously proposed mechanistic model by changing the order of 2-hydroxy deprotonation and H_2 binding and by adding a novel transient intermediate to the mechanism (Figure 9). In the modified mechanism, H_2 first binds as a non-classical hydride, an initial polarization occurs through the thiol group of the Hmd-bound cysteine, and then the 2-hydroxy group is deprotonated and polarizes the non-classical hydride. It is worth noting that these results do not necessarily exclude the involvement of a carbocation in catalysis. However, as they fit so well with the carbocation-independent mechanism, the probability that the carbocation is essential for the mechanism is low and that, in principle, the reduction of methylene-H_4MPT by H_2 should be possible. Therefore, the next step was to investigate the catalytic mechanism of the F_{420}-dependent methylene-H_4MPT reductase Mer in order to obtain valuable information on the mechanism of methylene-H_4MPT reduction for the construction of Hmd mutants.

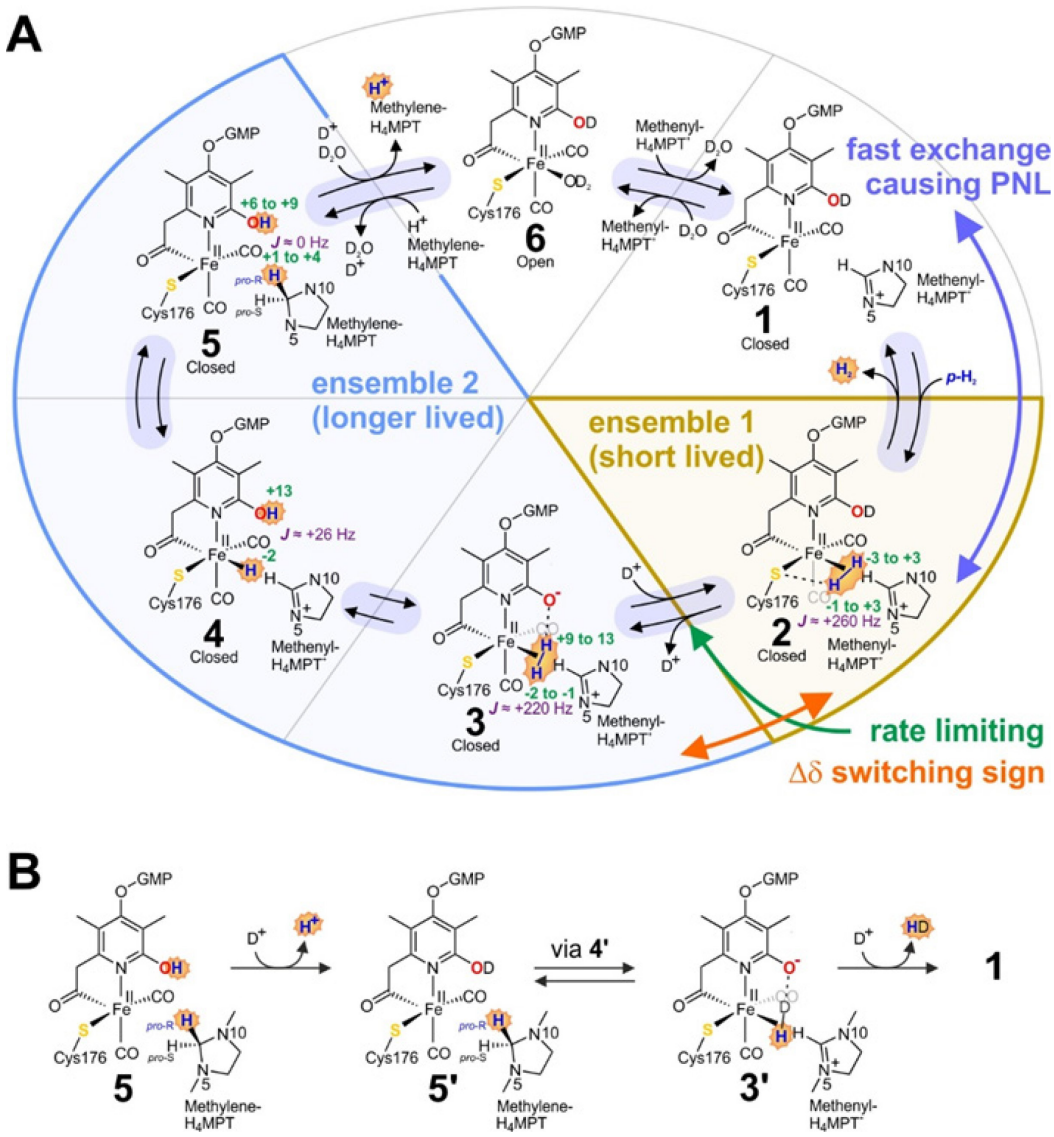

Figure 9: **(A)** Updated catalytic cycle of Hmd for the usage of *p*-H_2 in deuterated buffer. In contrast to the aforementioned catalytic cycle, H_2 enters the active site and binds to the Fe ion before the 2-hydroxy group is deprotonated. In this state (2) H_2 is first polarized by the thiol group of the FeGP binding cysteine. After deprotonation of the 2-hydroxy group, the resulting group is the stronger base and contributes to the main polarization of H_2 (3) ultimately leading to the splitting of H_2. The fast exchange between state (1) and state (2) is responsible for the PNL signal observed. The transition between state (2) and state (3) is responsible for the observed sign switch of the chemical shifts and is the rate limiting step. **(B)** Proposed mechanism for generating the HD-PHIP signal. As a prerequisite, the proton at the 2-hydroxy group of the FeGP cofactor must be exchanged for a deuterium ion. During the oxidation of methylene-H_4MPT, a HD molecule is formed which, after release from Hmd, produces the HD-PHIP effect. Figure adapted from (*135*).

Expression and characterization of jMer

Despite the fact that Mer is a relatively simple protein with no cofactor or prosthetic group, attempts to express Mer proteins from different organisms in *E. coli* have failed in the past because Mer formed inclusion bodies (*60*). However, in 2018, Robert White's research group successfully expressed Mer from *Methanocaldococcus jannaschii* (jMer) in *E. coli* and showed that jMer uses NADPH to reduce methylglyoxal in addition to its primary function (*56*). The corresponding plasmid pT7-7_jMer was kindly provided by the authors.

The expression protocol was optimized and a purification method was developed, as it was not possible to reproduce the method described by Miller et al. In the previous study, the jMer encoding gene *MJ1534* was amplified from genomic DNA of *M. jannaschii*, cloned into pT7-7 and transformed into *E. coli* BL21-CodonPlus (DE3)-RIL, which expresses rare tRNAs for arginine, isoleucine and leucine, to overcome limitations due to differences in codon usage between *E. coli* and *M. jannaschii* (*56*). Therefore, initial expression experiments were performed in *E. coli* Rosetta2(DE3) pLysS, which expresses other rare tRNAs in addition to those mentioned above. Moreover, the chaperonine-co-expressing strain *E. coli* ArcticExpress(DE3) was tested for its ability to promote soluble enzyme expression at low temperatures (*136*). Both expression strains were grown at 37 °C until they reached an OD_{600} of 0.6-0.8. Expression in the Rosetta2(DE3) pLysS strain was induced with 1 mM isopropyl-β-D-thiogalactopyranoside (IPTG) and further cultivated for 3 h at 37 °C. For the ArcticExpress(DE3) strain, the method was adapted according to the manufacturer's manual, i.e. after reaching an OD_{600} of 0.6-0.8, the culture was cooled in an ice bath for 10 min prior to the addition of 1 mM IPTG. The expression was performed at 20 °C for 3 h. Comparison of detected jMer activity normalized to harvested cell wet weight showed that expression using the ArcticExpress(DE3) system was approximately 60% higher than the Rosetta2(DE3) pLysS system (Figure 10). It was also found that the units per gram cell wet weight of the ArcticExpress(DE3) system did not change when the expression time was extended to 20 h, and that this approach could yield more cell wet weight per culture. This extended version became the standard method as the expression of soluble jMer molecules was possible but not very high. Around 0.5 mg of jMer per 1 g of cell wet weight could be obtained using this method, which was sufficient for the characterization and crystallization of jMer.

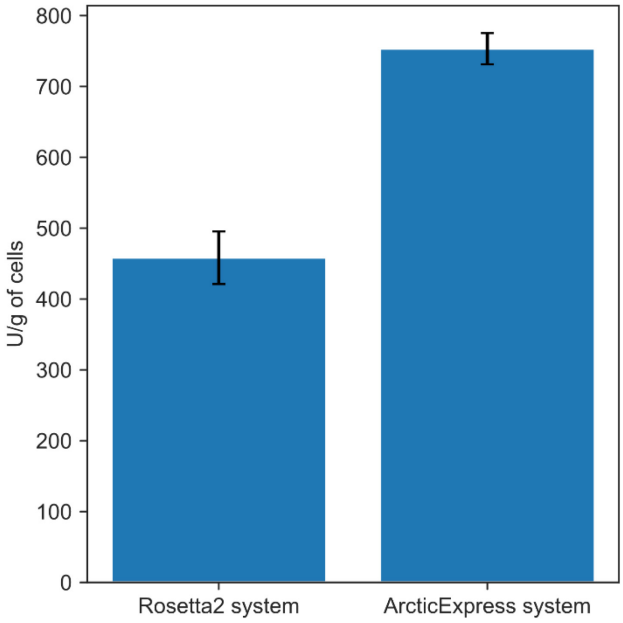

Figure 10: Comparison of different expression systems for the expression of jMer in *E. coli*. The bars show the average enzyme activity (U) per gram of cell wet weight and the error bars represent the standard deviation of two measurements. jMer was expressed using either the *E. coli* strain Rosetta2(DE3) pLysS at 37 °C or ArcticExpress(DE3) at 20 °C.

The biochemical characterization of jMer showed that its properties are consistent with previously reported Mer enzymes. The apparent K_m obtained for methylene-H_4MPT is 58 µM, the K_m for $F_{420}H_2$ is 5 µM and the apparent V_{max} is 500 U/mg (Figure S6). The K_m values are similar to the reported K_m values of all Mer enzymes and the V_{max} is similar to the reported V_{max} of *M. kandleri* and *A. fulgidus* (Table 1). All the above-mentioned Mer enzymes have already been shown to use F_{420}/$F_{420}H_2$ and methylene-H_4MPT/methyl-H_4MPT exclusively as substrates (*28*, *54*, *57–59*). Recently, Miller et al. reported that jMer uses NADPH and methylglyoxal as the substrates (*56*). In order to evaluate the potential of these substrates for the investigation of the catalytic mechanism of jMer, the experiments described by Miller et al. were repeated. Although a slight oxidation of NADPH was detected as indicated by a decrease in absorbance at 340 nm, this decrease was indistinguishable from that of the negative control (Figure S2).

Table 1: Comparison of the catalytic constants of different Mer enzymes. The apparent K_m values for methylene-H_4MPT (H) and $F_{420}H_2$ (F) are shown.

Mer from	Apparent K_m	Apparent V_{max}	Source
Methanosarcina barkeri	15 µM (H) 12 µM (F)	2200 U/mg	(*28*)
Methanothermobacter marburgensis	300 µM (H) 3 µM (F)	6000 U/mg	(*58*)
Methanopyrus kandleri	7 µM (H) 4 µM (F)	435 U/mg	(*57*)
Archaeoglobus fulgidus	16 µM (H) 4 µM (F)	450 U/mg	(*54*)
Methanocaldococcus jannaschii	58 µM (H) 5 µM (F)	500 U/mg	This work

Having succeeded in expressing jMer in *E. coli* at levels that allowed not only crystallization but also mutagenesis experiments, the next step in the project was to determine the structure of the ternary complex in order to obtain information on the catalytic mechanism of Mer.

Determination of the crystal structure of jMer

jMer showed good crystallization properties resulting in relatively large single crystals which diffracted very well to a resolution of 1.8 Å for the apoenzyme. In addition, a binary complex of jMer and F_{420} was also obtained and diffracted to a resolution of 1.9 Å. For the apoenzyme, the best crystal grew in 35% 3,5-methylpropanediol (MPD) and 100 mM sodium acetate pH 4.5. The crystal of the binary complex with F_{420} grew in 25% (v/v) polyethylene glycol (PEG) monomethyl ether 550, 100 mM 2-(N-morpholino)ethanesulfonic acid (MES) pH 6.5 and 10 mM zinc sulfate in the presence of 2 mM F_{420} and 2 mM methylene-H_4MPT. Both phase problems were solved by molecular replacement using the structure of Mer from *M. kandleri* (*55*) as template (Table S1). These are the first structures of the same Mer enzyme with and without F_{420}. In the reported binary complex structure of Mer from *M. barkeri*, an

additional electron density was found attached to F_{420}, which is likely to be an adduct blocking the reactive site of F_{420} (*52*). In the active site of the jMer binary complex an unreacted F_{420} molecule was found.

The overall structure of the jMer apoenzyme is very similar to the previously reported structures of Mer enzymes and shows the characteristic $(\beta/\alpha)_8$- or TIM-barrel fold (Figure 11A). The structural alignment of jMer and the previously reported Mer structures shows no significant differences in the overall protein fold (Figure S3A), which is characterized by root-mean-square deviation (RMSD) values of 1–1.2 Å. In particular, the inner core parts of the enzymes are structurally highly related. The secondary structural elements are connected by loops typically involved in the active site architecture of TIM barrel enzymes (*63*, *137*) and represent the major structural divergences between the aligned Mer structures. The apoenzyme of jMer crystallized as a homotetramer in the asymmetric unit and the binary complex crystallized as a homodimer. Size-exclusion chromatography showed that jMer in solution is a homodimer (~80 kDa) (Figure S4), which is also reported in the literature (*56*). In the dimer, a two-fold rotational axis is located within the protein-protein interface, resulting in an antiparallel orientation of the β-strands of each subunit (Figure S3B). The interface of both subunits is formed by α2, α3 and α4 and the loops after β2, β3 and β4. This shows that the extended loops not only play a functional role in the architecture of the active site, but also in the oligomerization of the enzyme. The structure of jMer in complex with F_{420} revealed the active site as a preformed cleft in which F_{420} is located (Figure 11B). The isoalloxazine ring is located within the β-strands, while the tail protrudes to the surface and is located between the loops after β4 and β5, which split apart to form a cleft. This cleft extends straight across the entire core unit to β8 and β1, forming a cavity rather than a closed active site. The cleft is bounded on both sides by the loops mentioned above. In particular, a rather large segment after β7 forms an open upper part of the cleft. Therefore, it can be assumed that the C_1 carrier will bind opposite F_{420} and in this cleft.

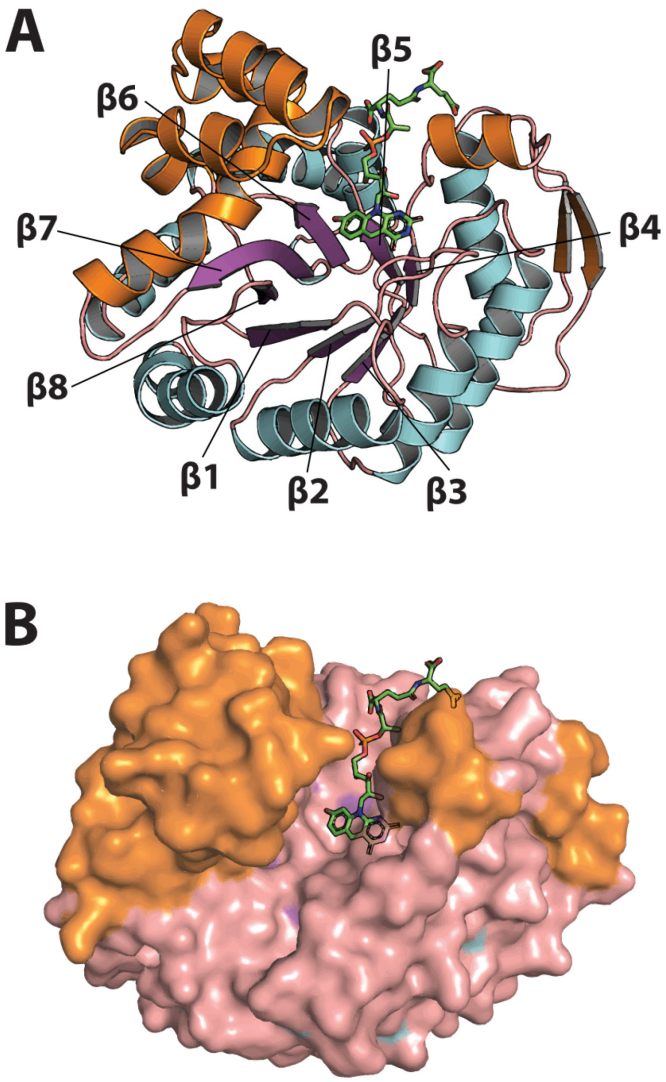

Figure 11: Overall structure of jMer in complex with F_{420}. **(A)** Cartoon representation of the structure. The β-strands of the $(\beta/\alpha)_8$ core unit are labelled and colored purple, while the α-helices of the core unit are colored light blue and the loops are colored salmon. The inserted segments, which form secondary structural elements in addition to the core unit, are colored orange. **(B)** Surface representation of the structure. The color scheme is the same as in panel A, showing that the putative active site cleft is formed exclusively by loop regions that are connecting the α-helices and β-strands of the $(\beta/\alpha)_8$ core unit (colored salmon) and additional secondary structure elements found in these loop regions (colored orange).

F_{420} interacts with jMer mainly by hydrogen bonding and to a lesser extent by hydrophobic interactions (Figure 12A). The hydrophobic interactions are mainly concentrated on the isoalloxazine ring system and are performed by Gly61 and Val62. Hydrogen bonds are distributed throughout the molecule of F_{420}, but are mainly found on the pyrimidine ring of the isoalloxazine ring system. The pyrimidine ring interacts with the backbone of Asp35 and with the carboxamide group of Asn64 (Figure 12A). F_{420} is found in a bent butterfly conformation

and the *Re*-face of F_{420} faces the protein backbone, while the *Si*-face faces the active site. This is not only consistent with the previously reported binary complex structure of Mer (*52*), but it has also been shown in the structures of several other F_{420}-dependent enzymes that F_{420} faces the active site with its *Si*-face (*71*, *82*, *83*) or by isotopic labeling it was determined that they transfer hydrides exclusively from the *Si*-face (*138–144*). The question of why all known F_{420}-dependent enzymes are *Si*-face specific remains unanswered. The fact that the property of *Si*-face specificity is shared by different enzyme families and is even uniform for enzymes from different domains of life suggests that *Si*-face specificity is an intrinsic property of F_{420} and not of the corresponding enzymes (*138*). Interestingly, the finding that flavoenzymes reconstituted with synthetic deaza-flavins can transfer the hydride from either *Si*- or *Re*-face seems to contradict this (*112*). In contrast to F_{420}-dependent enzymes, nicotinamide-utilizing enzymes and FAD- and FMN-dependent enzymes are not restricted to one face and transfer hydrides from their *Si*- or *Re*-face (*144*, *145*). For the purposes of this work, it is assumed that all F_{420}-dependent enzymes are *Si*-face specific and that the reported structure of jMer in complex with F_{420} is undoubtedly consistent with this paradigm.

Structural comparison of the apoenzyme and the binary complex of jMer revealed only minor structural changes upon F_{420} binding, as reflected by an RMSD of 0.24 Å over the complete amino acid sequence (Figure 12B). Notable structural changes in the active site region are found in the movement of the side chains of Tyr211 and Asn178. The sidechain of Tyr211 tilts 1.2 Å away from F_{420} and the side chain of Asn178 moves 4.9 Å out of the active site. These movements indicate slight adaptations to the binding of F_{420}, but are not very profound. Based on comparison of the binary complex structure of *M. barkeri* Mer with F_{420} and the apoenzyme structures of *M. marburgensis* and *M. kandleri* Mer, Aufhammer et al. reported that the carboxyl group of Asp96 in the apoenzyme faces Thr99 and that upon binding of F_{420}, the carboxyl group is reoriented towards the bulk solvent (*52*). These two residues are at the same position in jMer. In contrast to the reported results, no significant change in the conformation of the corresponding aspartate residue was observed, and the side chain in both structures faced the corresponding threonine (Figure 12B). Taken together, the results support the picture of a preformed active site of Mer enzymes that does not undergo substantial conformational changes upon binding of F_{420}.

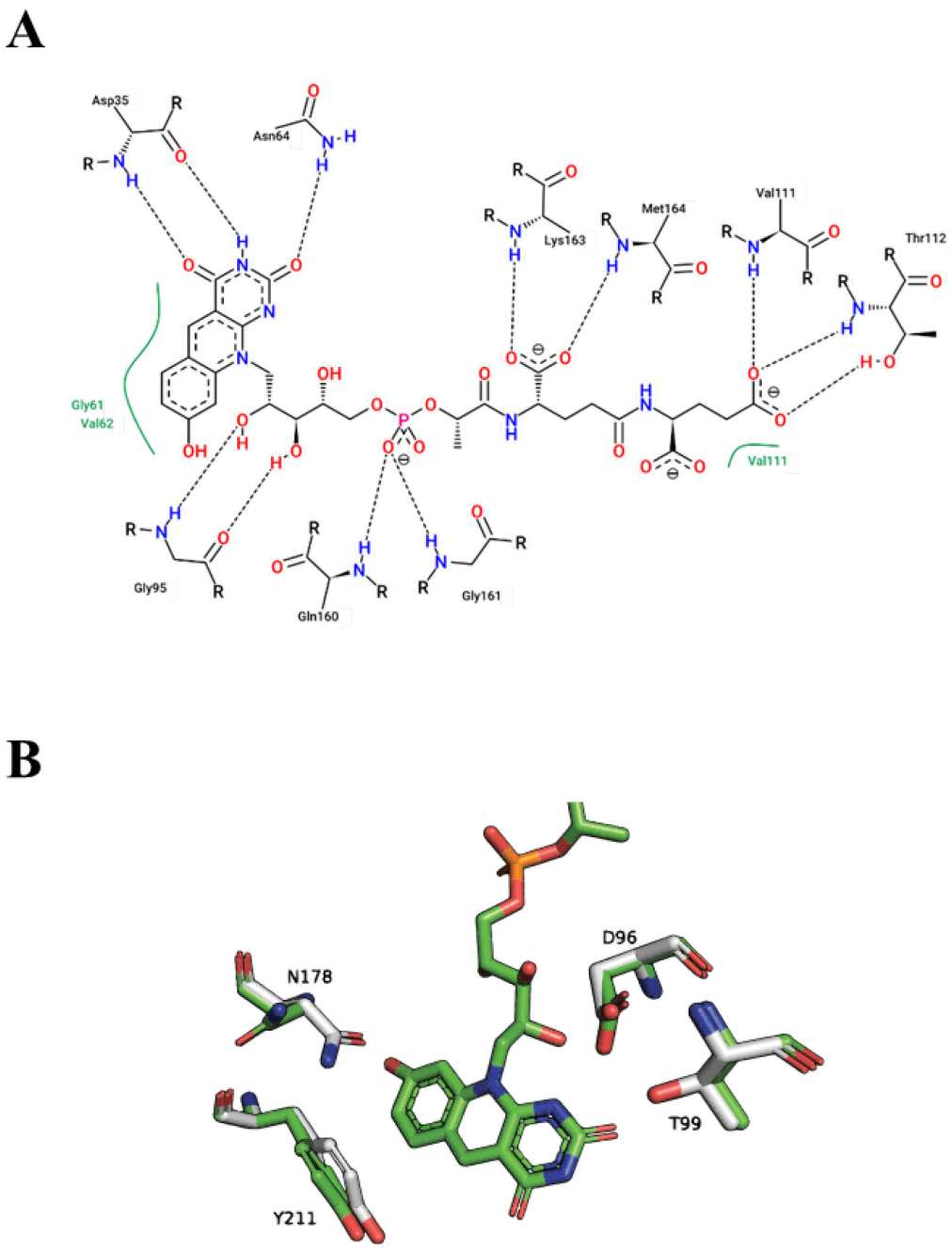

Figure 12: **(A)** Complex diagram showing the interaction between jMer and F_{420}. Polar interactions are shown as dashed lines. Hydrophobic interactions are shown as green lines. Note that the diagram is two-dimensional and therefore does not include information about the relative position of the amino acids to the *Re*- and *Si*-face of F_{420}. The interactions were analyzed using ProteinsPlus and the plot was visualized using the implemented version of PoseView (*146*, *147*). **(B)** Movement of side chains upon binding of F_{420} in jMer. Residues derived from the jMer apoenzyme structure are shown as a ball-and-stick model with grey carbons and residues derived from the binary complex structure of jMer with F_{420} are shown with green carbons. No evidence for the previously reported movement of Asp96 was found in the structures of jMer. The side chain of Tyr211 tilts 1.2 Å away from the F_{420} binding site. The most pronounced movement was observed for the side chain of Asn178, which moves 4.9 Å away from the F_{420} binding site upon binding of F_{420}.

jMer contains a non-prolyl *cis*-peptide (NPCP) bond, which is essential for catalytic activity. These bonds are rare and are typically important for the function of the corresponding enzyme (*68*, *69*). The NPCP bond in jMer is located in the loop after β3, under the central pyridine ring of F_{420}, between Gly61 and Val62 (Figure 13). Furthermore, this NPCP bond has been found at the equivalent position in all known Mer structures and even in other, but not all, enzymes of the bacterial luciferase superfamily, e.g. in the F_{420}-dependent glucose-6-phosphate dehydrogenase (*72*) and the F_{420}-dependent alcohol dehydrogenase (*71*). It has been proposed in the past that the NPCP bond acts as a backstop for the placement of F_{420} in the active site (*52*). The role of this NPCP bond was tested by exchanging Val62 to Pro62, presumably resulting in a prolyl-*cis* peptide bond, and modelling the corresponding mutant structure using AlphaFold (*148*). The specific activity decreased from 160 U/mg under standard assay conditions to 0.09 U/mg when the NPCP bond was replaced by a putative prolyl-*cis* peptide bond. Comparison of the obtained crystal structure of jMer in complex with F_{420} and the AlphaFold model from the AlphaFold Protein Structure Database (identifier: AF-Q58929-F1) showed that AlphaFold's modelling process resulted in a very reliable structural model. The overall RMSD was 0.48 Å for all amino acids and the loop containing the NPCP bond was modelled very accurately with very high confidence scores per residue expressed as pLDDT values above 98. It can therefore be assumed that AlphaFold is capable of predicting the structure of jMer_V62P. The calculated AlphaFold model indicated the formation of a prolyl-*cis* peptide bond in the mutant structure, resulting in a very high pLDDT of over 98 for the region (Figure 13). It has been shown in the past that the exchange of a prolyl-*cis* peptide bond to an NPCP is possible (*149*).

Alignment of the jMer wild type binary complex structure and the mutated jMer_V62P model showed that the backbone of the corresponding loop remains in the same position after exchange to a prolyl-*cis* peptide bond and that the Cβ atoms of Val62 and Pro62 are in the same position (Figure 13). However, Cγ and Cδ of Pro62 occupy space required by F_{420} in the wild type enzyme, resulting in a large overlap of F_{420} and the prolyl ring. This suggests that a prolyl-*cis* peptide bond could also act as a backstop for F_{420}, but that a simple replacement of the existing NPCP bond with a prolyl-*cis* peptide bond would require major structural changes in the F_{420} binding site. This structural alignment suggests that the NPCP bond can be formed by replacing Val62 in the wild type enzyme with a small hydrophobic amino acid. Larger side chains cannot be placed at this position because they would interfere with the loop after α4, which is involved in the binding of the first two hydroxy groups of the F_{420} tail region (Figure 12A). Indeed, valine is not strictly conserved at this position and isoleucine is found in other

Mer enzymes, e.g. in Mer of *M. kandleri* (Figure 13) (*55*). Furthermore, the amino acid side chain at this position may also play an important role in the formation of the pronounced butterfly conformation of F_{420}, as Cβ and Cγ are positioned towards the ring system of F_{420}. This pushing force on the central pyridine ring of the isoalloxazine ring system is accompanied by pulling forces on the pyrimidine ring as described above, probably resulting in the observed butterfly conformation of F_{420}. This also explains why only valine and isoleucine occur in this position in nature. Smaller hydrophobic side chains, such as in alanine, are probably not large enough to generate the pressure needed to push against the central pyridine ring, and larger side chains interfere with the hydrogen bonding network involved in binding the tail region of F_{420} (Figure 12A). Taken together, the mutation experiment supported the proposed role of the NPCP bond as an essential backstop in Mer enzymes and clarified why a more common prolyl-*cis* peptide bond is not used.

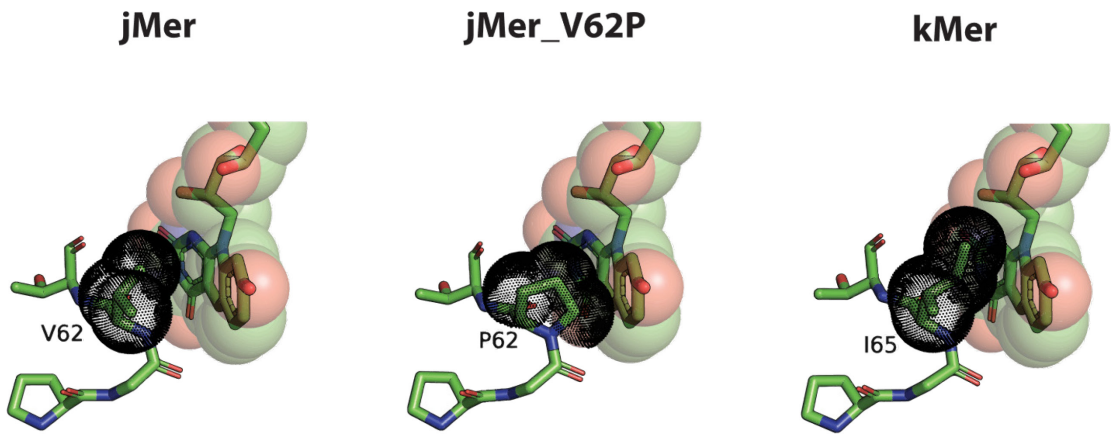

Figure 13: Possible structural variations of the non-prolyl *cis*-peptide bond region of Mer. F_{420} and the amino acids are shown as ball-and-stick models with green carbons. The van der Waals radii are shown as transparent spheres for F_{420} and as black dotted spheres for the corresponding side chain of the amino acids. The NPCP bond of the jMer wild type as found in the binary complex crystal structure (jMer). The AlphaFold model of the variant jMer_V62P and the crystal structure of *M. kandleri* Mer (kMer). The structures were aligned with the binary complex of jMer to model F_{420} into the AlphaFold model of jMer_V62P and the apoenzyme structure of kMer. The side chains of valine and isoleucine do not overlap with F_{420}, whereas the side chain of proline is too bulky and collides with F_{420}.

To study the catalytic mechanism of Mer, an attempt was made to determine the structure of a ternary complex with F_{420}/$F_{420}H_2$ and methylene-/methyl-H_4MPT. However, after numerous attempts to solve the ternary complex structure, the resulting electron densities

revealed only F_{420} as bound ligand and no C_1 carrier. Therefore, a search was made for similar reactions in nature to find a suitable model to study the catalytic mechanism of Mer in an indirect way. FAD-dependent MTHFRs catalyze the analogous reduction of methylene-H_4F, and previous studies have shown that FAD-dependent MTHFRs share structural similarities with Mer (*52*, *55*, *118*). Unlike Mer, the reducing agent NAD(P)H and the C_1 carrier methylene-H_4F bind to the same position resulting in a ping-pong mechanism. In addition, the flavin-independent form of MTHFR (Mfr) has recently been discovered. This enzyme shares a ternary complex catalytic mechanism with Mer (*86*). Both types of MTHFR are promising models for studying the catalytic mechanism of Mer.

Purification and characterization of hMfr

Based on the reported Mfr sequence from *Mycobacterium smegmatis* (MSMEG_6596) (*86*), a BLAST search was performed to find promising candidates. The homolog from *Mycolicibacterium hassiacum* (hMfr, Uniprot accession number: K5BDY6) was selected for the following reasons. First, hMfr shares 80% sequence identity with MSMEG_6596, making it highly likely that it is indeed a flavin-independent MTHFR. Second, hMfr shares 78% sequence identity with the Mfr protein from *Mycobacterium tuberculosis* (*87*). Since Mfr in *M. tuberculosis* has been shown to be essential for its growth, the structure and catalytic mechanism of hMfr provide valuable information for the development of antimycobacterial drugs (*87*). Thirdly, *M. hassiacum* is a thermophilic organism that can grow between 40 °C and 65 °C (*150*, *151*). It is widely accepted that thermophilic proteins are good candidates for protein crystallization.

hMfr was expressed in *E. coli* and a purification procedure was established. Since a heat shock step was planned for purification, the precipitation temperature of hMfr had to be determined first. hMfr was stable up to 50 °C, started to lose activity at 60 °C and no activity could be detected after incubation at 70 °C (Figure 14A). Therefore, 50 °C was used for the heat shock. After the final size exclusion column, hMfr was found to be purified to homogeneity (Table 2, Figure S5A) and this preparation was used for crystallization trials and to investigate the FAD dependency of hMfr. Enzyme loss during hydrophobic interaction chromatography was a major problem for measuring the activity of mutant enzymes with very low enzyme activity, because the enzyme assay requires large amounts of the variants. To overcome this problem, the purification method had to be improved. A shorter method was developed,

omitting ammonium sulfate precipitation and hydrophobic interaction chromatography (Phenyl-Sepharose HP) and applying the heat shock supernatant directly to the Resource Q-column. The specific activity of the shorter method was 14 U/mg and similar to the specific activity of the longer method (Table 2). The SDS-PAGE showed low contamination (Figure S5B). This preparation was used for kinetic analyses. As *E. coli* contains endogenous MTHFR, *E. coli* BL21(DE3) STAR was transformed with an empty pET-24b(+) vector and used as a negative control to test whether MTHFR from *E. coli* was co-purified by the purification methods. The negative control showed that the endogenous MTHFR activity of *E. coli* contributes only 4% to the total activity found in the cell extract and that with the shorter purification method no detectable activity of MTHFR from *E. coli* is found after the Resource Q-column (Table 3). Thus, both purification methods result in activity contributed only by expressed hMfr.

Table 2: Purification of hMfr from 3 g of *E. coli* BL21(DE3) STAR cells. One unit (U) corresponds to the oxidation of 1 µmole of NADH per minute. The standard assay contains 100 µM NADH and 300 µM methylene-H_4F. For crystallization, UV/Vis spectrum and FAD dependency, the Resource Q preparation was subjected to an additional size-exclusion chromatography step. For enzyme assays preparation, a shorter method was used that omitted ammonium sulfate precipitation and hydrophobic interaction chromatography (Phenyl-Sepharose HP).

	Activity (U)	Protein (mg)	Specific activity (U/mg)	Yield (%)	Purification factor (fold)
Cell extract	1200	200	6	100	1.0
50 °C heat treatment	1000	100	10	82	1.6
40% ammonium sulfate	900	86	10	73	1.7
Phenyl-Sepharose HP	500	49	10	43	1.7
Resource Q	300	19	16	25	2.6

Table 3: Negative control for the purification of hMfr. 3 g of *E. coli* BL21(DE3) STAR harboring an empty pET-24b(+) vector were used to investigate the endogenous MTHFR activity of *E. coli*. One unit (U) corresponds to the oxidation of 1 µmole of NADH per minute. The standard assay contains 100 µM NADH and 300 µM methylene-H_4F.

	Activity (U)	Protein (mg)	Specific activity (U/mg)
Cell extract	53	113	0.5
50 °C heat treatment	13	83	0.2
Resource Q flow-through	6	29	0.2
Resource Q (hMfr peak)	0	4	0

Following the establishment of a purification procedure for hMfr, the enzyme was biochemically characterized prior to crystallization trials. The FAD dependency of hMfr was investigated by adding 500 µM FAD to the purified hMfr preparation after size-exclusion chromatography. After incubation for 10 min, the hMfr solutions were used to start the standard assay. The enzyme activity was compared with that of the hMfr preparation without pre-incubation with FAD. No difference in activity was observed between aliquots with and without FAD (Figure 14B). Furthermore, the UV/vis spectra of 2.5 mg/ml enzyme solution showed only one protein peak at 280 nm and, in particular, no peaks at 380 nm and 450 nm, which are characteristic of flavoenzymes (Figure 14C) (*86*). Size-exclusion chromatography showed that hMfr has a molecular mass of ~30 kDa, suggesting that it is in a monomeric state, like the Mfr enzyme from *M. smegmatis* (Figure 14D) (*86*). Although hMfr precipitates during incubation for 20 min at temperatures above 50 °C, the measured temperature dependency of activity suggested an optimum temperature of 70 °C (Figure 14E). The optimum pH is around pH 7. The activity decreases drastically at pH 9. Because NADH is unstable in acidic environments, it was not possible to determine the activity below pH 6 (Figure 14F).

The determination of the kinetic constants showed that hMfr has similar properties to the previously reported Mfr enzymes from *M. smegmatis* and to the FAD-dependent MTHFRs. The K_m for NADH is 16 µM and the K_m for methylene-H_4F is 160 µM (Table 4, Figure S8). Comparison with other Mfrs and MTHFRs shows that the K_m for NAD(P)H lies between 10 µM and 36 µM, with the exception of MSMEG_6649 (Mfr) which has a K_m for NADH of 110 µM. This can be explained by the fact that MSMEG_6649 is a truncated version of MSMEG_6596

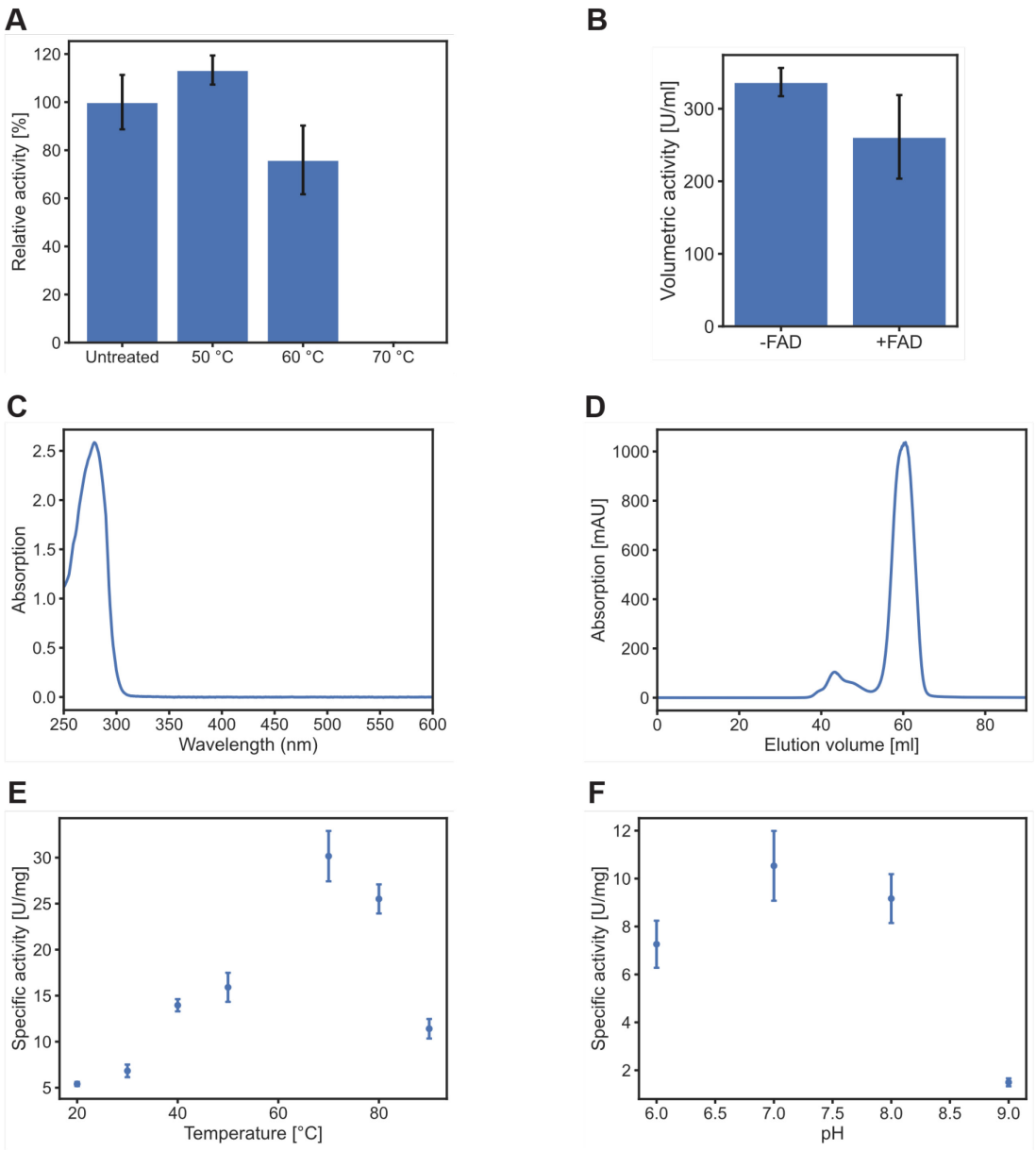

Figure 14: Characterization of hMfr. **(A)** Relative activities of heat-treated aliquots after 20 min incubation at different temperatures. **(B)** Activities of the same aliquots without FAD (-FAD) and with 500 µM FAD (+FAD). The purified hMfr preparation after size-exclusion chromatography was incubated in the presence of 500 µM FAD and then 10 µl of the hMfr solution was assayed in the standard assay. **(C)** UV/vis spectrum of 2.5 mg/ml purified hMfr preparation in 100 mM MOPS/NaOH pH 7.0 using a 1 cm light-path quartz cuvette. **(D)** Size-exclusion chromatography using a HiPrep Sephacryl S-100 HR column. The peak centered around 60 ml elution volume corresponds to the hMfr activity. **(E)** Temperature dependency of the specific activity of hMfr. **(F)** pH dependency of the specific activity of hMfr.

(Mfr), which also has a 5-fold lower activity than MSMEG_6596 (*86*). The K_m values for methylene-H_4F are more variable and typically range from 0.4 µM (eMTHFR) to 180 µM (*T. thermophilus* MTHFR). hMfr is therefore found at the upper end of the K_m values for

methylene-H_4F. The V_{max} of hMfr is 18 U/mg and the k_{cat} is 590 min^{-1}. Both values are similar to the V_{max} and k_{cat} values of MTHFR from *M. smegmatis*, *E. coli* and *T. thermophilus*. The eukaryotic FAD-dependent MTHFR proteins appear to have higher turnover rates, and the activity and turnover rate of the enzyme from *Blautia producta* are remarkably high at 380 U/mg and 12 200 min^{-1}. This can be explained by the fact that *B. producta* is an acetogen and the catalyzed reaction is involved in catabolism, which requires higher enzymatic turnover rates (*88*, *123*).

Table 4: Comparison of catalytic constants of Mfrs and MTHFRs. The K_m values for methylene-H_4F (H) and the K_m values for NAD(P)H (N) are shown. The blue background indicates Mfrs, the red background indicates the prokaryotic FAD-dependent MTHFRs, and the green background indicates the eukaryotic FAD-dependent MTHFRs. Most of the activities shown were measured around 25 °C, with the exception of hMfr (40 °C) and *T. thermophilus* MTHFR (50 °C).

Enzyme	K_m	V_{max}	k_{cat}	Source
hMfr	160 µM (H) 16 µM (N)	18 U/mg	590 min^{-1}	This work and (*152*)
MSMEG_6596 (Mfr)	63 µM (H) 33 µM (N)	11 U/mg	370 min^{-1}	(*86*)
MSMEG_6649 (Mfr)	150 µM (H) 110 µM (N)	2.3 U/mg	79 min^{-1}	(*86*)
Escherichia coli MTHFR	0.4 µM (H) 3.5 µM (N)	4 U/mg	132 min^{-1}	(*153*)
Blautia producta MTHFR	100 µM (H) 10 µM (N)	380 U/mg	12200 min^{-1}	(*123*)
Thermus thermophilus MTHFR	180 µM (H) 10 µM (N)	9 U/mg	290 min^{-1}	(*110*)
Pig liver MTHFR	88 µM (H) 16 µM (N)	22 U/mg	1700 min^{-1}	(*154*)
Homo sapiens MTHFR	22 µM (H) 36 µM (N)	31 U/mg	2440 min^{-1}	(*119*)

There are several NADH analogues in use as antimycobacterial agents, but their mode of action is not yet fully understood. To evaluate the pharmaceutical potential of hMfr, isonicotinic acid, pyrazinoic acid and prothionamide were tested as possible inhibitors. Isonicotinic acid and pyrazinoic acid are the metabolically activated forms of the first-line antibiotics isoniazide and pyrazinamide (*155*, *156*). Prothionamide is thought to be directly active against *M. tuberculosis* and is used as a second-line antimycobacterial agent (*157*). Comparison of untreated aliquots of hMfr and aliquots treated with 1 mM isonicotinic acid, pyrazinoic acid or prothionamide showed no effect on hMfr activity (Figure 15). Thus, Mfr shows great potential for the development of novel antimycobacterial drugs.

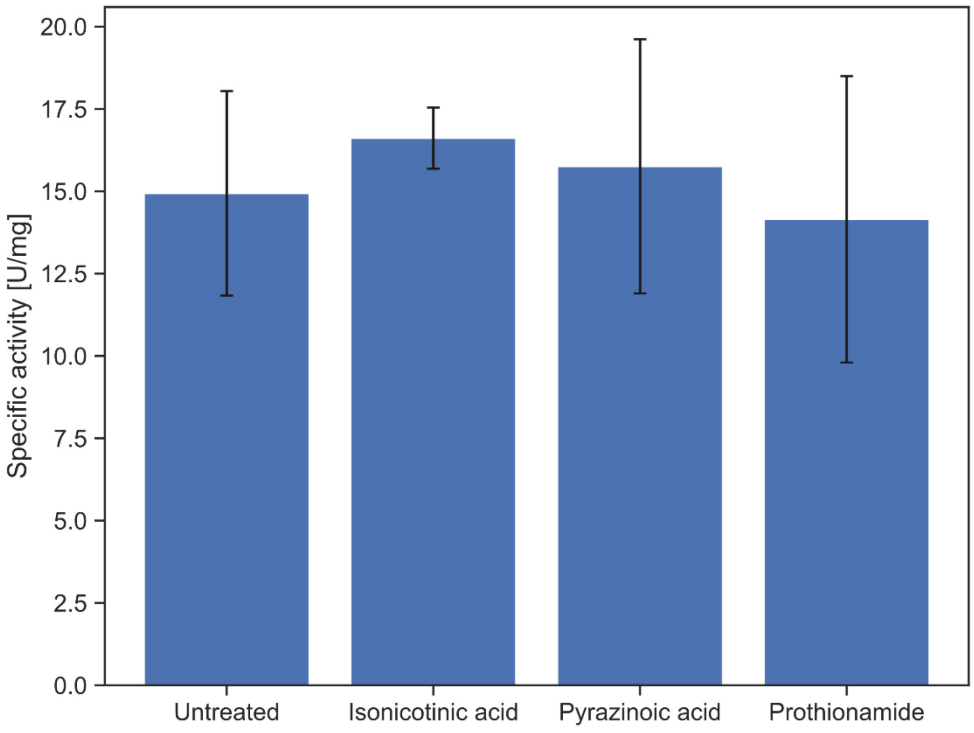

Figure 15: Effects of different antimycobacterial agents on the activity of hMfr. The compounds were added to the standard assay to a final concentration of 1 mM. Each bar represents the mean of three independent measurements and error bars represent the corresponding standard deviation.

The characterization of hMfr showed that it is indeed one of the novel flavin-independent MTHFRs. hMfr catalyzes the reduction of methylene-H_4F using NADH as reducing agent in a ternary complex mechanism. This means that both the C_1 carrier and the reducing agent must bind to the active site at the same time, as is the case with Mer. Therefore, the geometry of the hydride transfer in Mfr and Mer might be similar and the comparison of the

structures should provide valuable information about the active site architecture and catalytic mechanism.

Determination of the crystal structure of hMfr

hMfr did not crystallize easily and formed rather small and interconnected plates under most crystallization conditions. After several rounds of optimization, small rod-shaped crystals and diffracted up to a resolution of 1.8 Å. The structure was solved by molecular replacement using the AlphaFold model of hMfr as search model (Table S2).

The overall structure of hMfr is composed of a TIM barrel fold with a closed cleft in the middle of the C-terminal end of the barrel structure (Figure 16A). The loops after β2 and β6 are quite large and especially the loop after β6 forms several additional α-helical elements. These loops are joined at the C-terminal half of the barrel core, forming a roofed cavity rather than the open cleft found in jMer. The strands of β4 and β5 split apart, as do the loops after β8 and β1, resulting in a cavity that spans the entire core unit (Figure 16B). Since the active site in $(\beta/\alpha)_8$-barrel proteins is always located in the C-terminal half of the β-barrel (*63*, *137*), it is highly likely that this cleft is the active site of hMfr.

It is noteworthy that these structural elements are the same that define the active site of eMTHFR and the putative active site cleft of jMer (Figure 17). In eMTHFR the FAD binding site is located between β4 and β5 and in jMer the F_{420} binding site is located between β4 and β5. In addition, the methyl-H_4F binding site of eMTHFR is located between β7, β8 and β1 (*118*, *121*). In the structure of jMer, the putative active site cleft extends from the F_{420} binding site to β8 and β1, which are likely to form the binding site of the C_1 carrier. The fact that the active site clefts in eMTHFR, jMer and hMfr are built up by the same secondary structures was surprising because the three tetrahydropterin reductases do not share any sequence motif and their sequence identities are low. hMfr shares only 12% sequence identity with jMer and 17% sequence identity with eMTHFR. jMer and eMTHFR share 16% sequence identity. A motif analyses using InterPro (*158*) showed that eMTHFR belongs to the homologous superfamily of FAD-linked oxidoreductase-like proteins (IPR029041) that consist of the two families methylenetetrahydrofolate reductase-like enzymes (IPR003171) and proline oxidase enzymes (IPR015659). hMfr revealed no known sequence motif. jMer belongs to the homologous superfamily of luciferase-like domain enzymes (IPR036661, also referred to as bacterial

luciferases) that consists of various enzyme families comprising a big variety of catalyzed reactions. The low sequence identity of the three methylene-tetrahydropterin reductases and the fact that they do not share a single common sequence motif shows how surprising it is that the possible active sites of the enzymes are formed by the same structural motifs and are possibly located at the same sites in the respective enzymes, since a common ancestor has not been assumed so far.

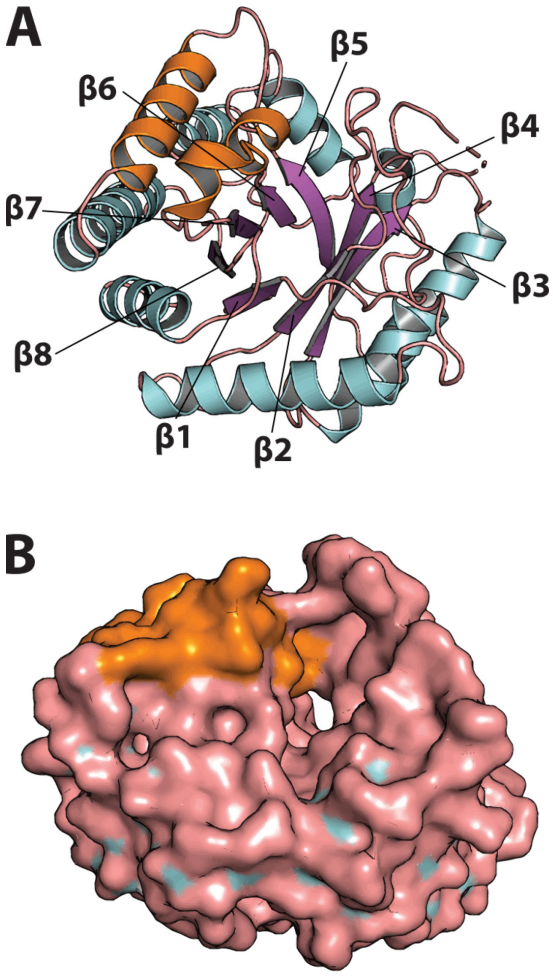

Figure 16: Overall structure of hMfr. **(A)** Cartoon representation of the structure. The β-strands of the $(\beta/\alpha)_8$ core unit are labelled and colored purple, while the α-helices of the core unit are colored light blue and the loops are colored salmon. The inserted segments, which form secondary structural elements in addition to the core unit, are colored in orange. **(B)** Surface representation of the structure. The color scheme is the same as in panel A, showing that the putative active site cavity is formed exclusively by loop regions that are connecting the α-helices and β-strands of the $(\beta/\alpha)_8$ core unit (colored salmon) and additional secondary structure elements found in these loop regions (colored orange).

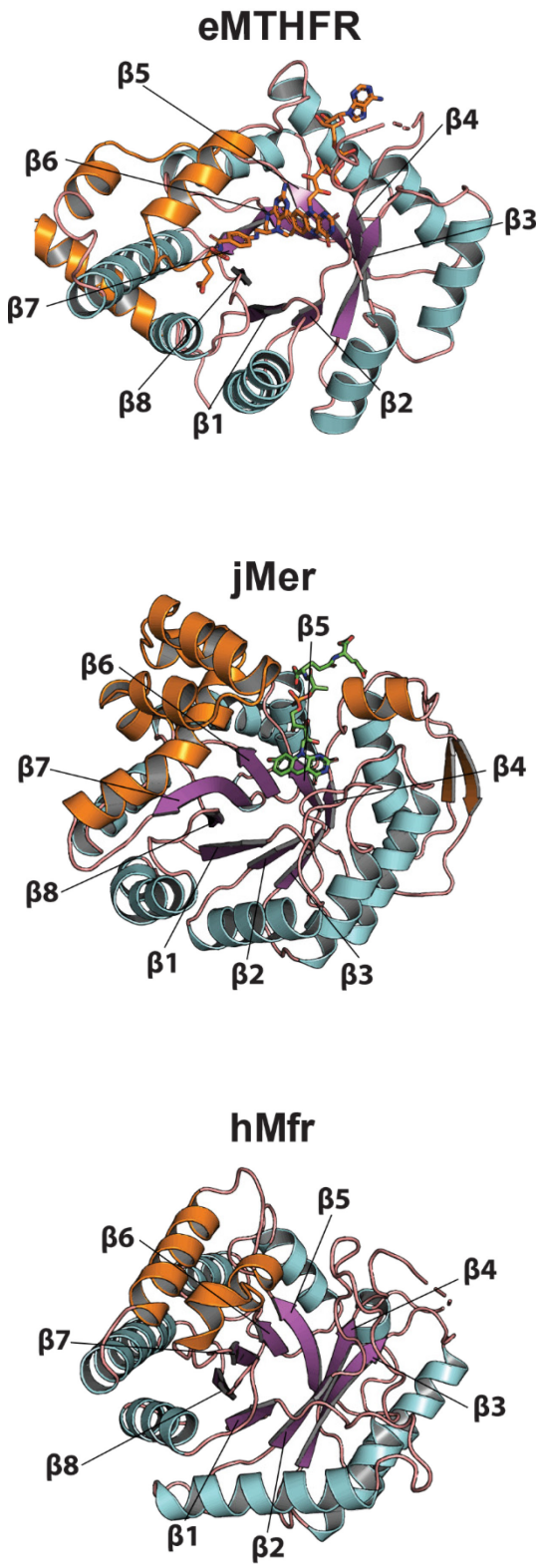

Figure 17: Comparison of the tertiary structures of eMTHFR, jMer and hMfr. The β-strands of the $(\beta/\alpha)_8$ core unit are labelled and colored purple, while the α-helices of the core unit are colored light blue and the loops are colored salmon. The inserted segments, which form secondary structural elements in addition to the core unit, are colored in orange. Methyl-H_4F and FAD are shown in orange and F_{420} is shown in green.

The astonishing similarity between the structures of jMer, hMfr and eMTHFR, together with the fact that no crystals could be obtained in the presence of any ligand combination for hMfr, prompted a more detailed comparative study of the active sites of the three methylene-tetrahydropterin reductases.

Ternary complex model building

To compare the active sites of eMTHFR, jMer and hMfr, a ternary complex model was constructed using a knowledge-based three-dimensional alignment approach. A simple three-dimensional alignment was not successful because of the large differences between the three methylene-tetrahydropterin reductases (Figure 18, step 1). The alignment of jMer with hMfr gave an RMSD of 4.6 Å over 232 amino acids, the alignment of jMer with eMTHFR gave an RMSD of 5.3 Å over 200 amino acids, and eMTHFR and hMfr were aligned with an RMSD of 4.7 Å over 240 amino acids. It was assumed that the hydride transfer process between $FADH_2$ and methylene-H_4F in eMTHFR and the hydride transfer process between $F_{420}H_2$ and methylene-H_4MPT in jMer should be similar, resulting in a similar active site geometry. Therefore, the hydride-bearing atoms of FAD (N5) in the eMTHFR structure and of F_{420} (C5) in the jMer structure were aligned in the same position in space (Figure 18, step 2) and the rest of the proteins was aligned with the constraint that these two atoms must not move (Figure 18, step 3). After this step, the apoenzyme structure of hMfr could be aligned with the structure of eMTHFR (Figure 18, step 4). In these functionally aligned structures amino acids that were in the same position and had similar or even identical chemical properties potentially perform the same or similar functions in all three methylene-tetrahydropterin reductases. This resulted in a functional ternary complex model of all three reductases, representing common patterns of amino acid residues in the active sites (Figure 18, step 5). With this model in hand, the positions of methyl-H_4MPT in jMer and NADH and methyl-H_4F in hMfr could be inferred (Figure 18, step 5) and the similarities of the active site architectures of the three methylene-tetrahydropterin reductases could be investigated.

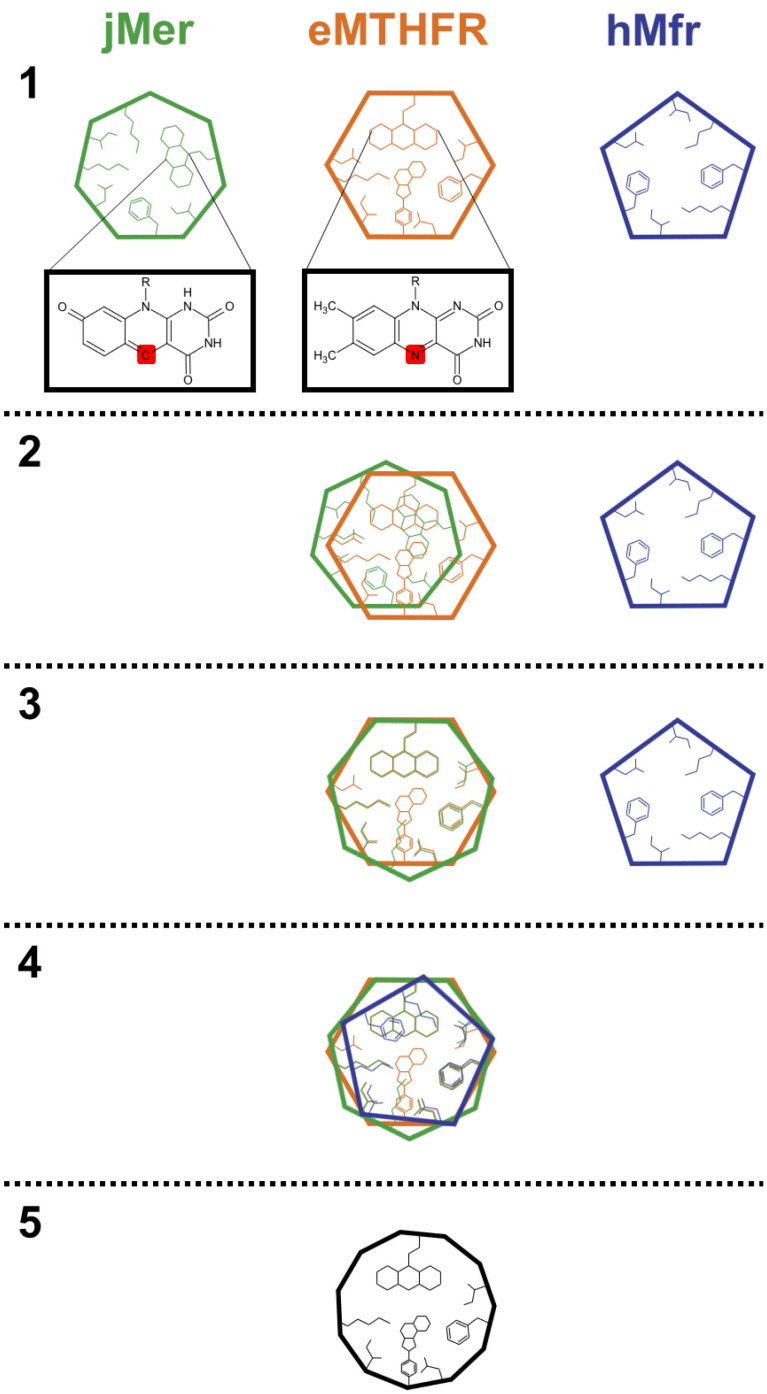

Figure 18: Illustration of the functional alignment process of jMer (green), eMTHFR (orange) and hMfr (blue). **(Step 1)** F_{420} and FAD are shown as a simplified three-membered ring system with a small tail, and methyl-H_4F is shown as a simplified version consisting of two hexagons and a pentagon fused together. The hydride-bearing atoms of the reducing agents are highlighted in red. **(Step 2)** The hydride-bearing N5 of FAD and C5 of F_{420} were aligned. **(Step 3)** Rotation of jMer with simultaneous fixation of the two hydride-bearing atoms resulted in good alignment. **(Step 4)** hMfr was aligned to eMTHFR. **(Step 5)** Extraction of the position of the reducing agent (FAD, F_{420}), the C_1 carrier (methyl-H_4F) and overlapping amino acids with similar physicochemical properties led to a general ternary complex model of the methylene-tetrahydropterin reductases (black). From this general ternary complex model, the positions of the C_1 carriers in jMer and hMfr could be deduced, as well as the position of the reducing agent NADH in hMfr.

The ternary complex models of jMer and hMfr predicted by a knowledge-based three-dimensional alignment approach suggested the binding positions of the different ligands. With these models in hand, the position of methyl-H_4MPT in jMer was deduced first by the position of the modeled methyl-H_4F. The distance between C14a of the modelled methyl-H_4F and C5 of F_{420} is 3.3 Å (Figure 19A and B). This is a suitable distance for a hydride transfer. The surface representation of the modelled ternary jMer complex shows that there is no substantial overlap of methyl-H_4F with amino acids of jMer. Furthermore, the head portion between the pterin ring and the *para*-aminobenzoic acid (PABA) ring aligns well with the active site cleft, whereas the rest of the tail is more detached from the protein (Figure 19A). Presumably, the longer tail of methyl-H_4MPT would be involved in the binding and would therefore be attached to the surface of jMer at a slightly different angle. Notably, there is a hydrophobic pocket consisting of the conserved residues Phe233, Val8 and Val230 just below the modelled PABA ring, which is likely to be the correct binding site for the PABA ring. This suggests that the tail of methyl-H_4MPT should be pointing in this direction.

For the ternary complex model of hMfr, the putative binding site of NADH is represented by the modelled FAD and the putative binding site of methyl-H_4F is represented by the modelled methyl-H_4F (Figure 19C and D). In contrast to the ternary complex model of jMer, the methyl-H_4F in the model of hMfr overlaps somewhat with the protein part. The part around the carbonyl group of the pterin ring overlaps with the loop after β2 and the PABA ring together with the glutamate tail overlaps with the loop after β7, indicating that the methyl-H_4F molecule is rather rotated towards the active site cleft of hMfr. A similar situation is found for the modelled FAD molecule. While the pyrazine and phenyl rings fit well into the putative binding pocket, the pyrimidine ring overlaps with the loop after β2 (Figure 19C and D). This finding suggests that the active site cleft of hMfr is narrowed compared to that of eMTHFR to accommodate the smaller nicotinamide ring of NADH. Thus, the nicotinamide ring of NADH in the structure of hMfr is likely to be located in the position occupied by the pyrazine and phenyl ring. These results suggest that the substrate-NADH pair in hMfr must be rotated relative to the pair in eMTHFR. In a further step, FAD was replaced by NADH and the modelled NADH and methyl-H_4F molecules were rotated together to achieve the least possible overlap of ligand and protein (Figure 19E and F).

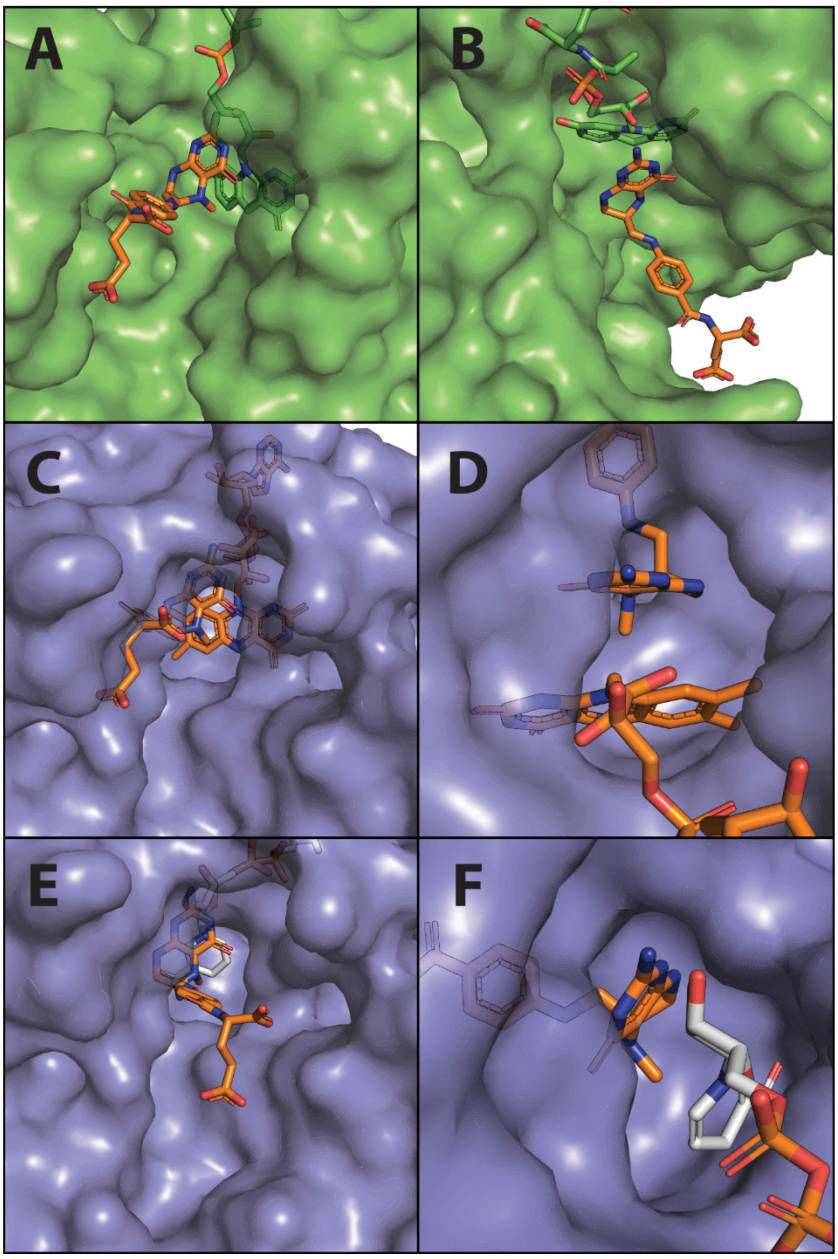

Figure 19: Ternary complex models of jMer and hMfr. The colors indicate the origin of the ligands. Ligands derived from the eMTHFR structure are colored orange, ligands derived from the jMer structure are colored green, and ligands derived from manual modeling are colored gray. **(A + B)** Ternary complex model of jMer built of the binary complex of jMer and F_{420} (green) and methyl-H_4F (orange) from the functional alignment. **(C + D)** Ternary complex model of hMfr with FAD (orange) and methyl-H_4F (orange) derived from the functional alignment. **(E + F)** Refined ternary complex model of hMfr. FAD was replaced by NADH (gray) and both NADH and methyl-H_4F (orange) were rotated together to achieve the lowest possible overlap with hMfr.

Based on these models, residues interacting with the pterin part of the modelled methyl-H_4F were investigated. At first glance, no direct interactions between the protein and methyl-H_4F could be observed in the ternary complex models of jMer and hMfr due to possible

structural changes of the proteins upon ligand binding. However, a careful comparison with the active site structure of eMTHFR showed that most of the residues interacting with methyl-H_4F have an equivalent in the modelled jMer and hMfr structure (Position A-D depicted in Figure 20).

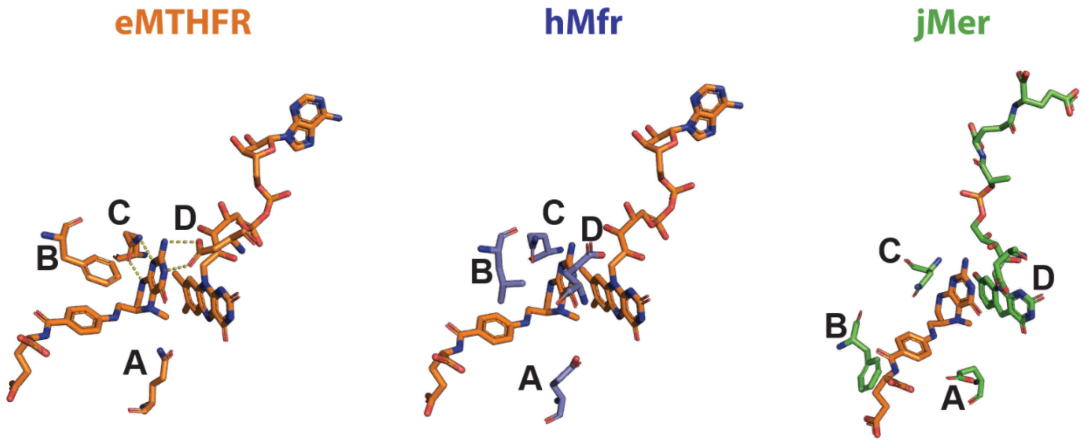

Figure 20: Comparison of the tetrahydropterin binding sites of the crystal structure of eMTHFR and the ternary complex models of hMfr and jMer. Residues from the structure of eMTHFR are colored orange at the carbon atoms, residues from the structure of hMfr are colored blue, and residues from the structure of jMer in complex with F_{420} are colored green. Equivalent positions are indicated by letters.

In all three methylene-tetrahydropterin reductases there is an acidic functionality at position D (Figure 20). In eMTHFR, Asp120 faces the pterin ring of methyl-H_4F and forms two polar bonds with nitrogen atoms of the pterin ring. The equivalent Asp96 in jMer, however, faces the inner core of jMer interacting with Thr99 and therefore cannot form polar contacts with methyl-H_4F in this conformation. This suggests that the side chain of Asp96 changes position upon binding of the C_1 carrier. A similar situation occurs at position D in hMfr, which is occupied by Glu55 that probably also binds the pterin ring of the C_1 carrier. In addition to binding methyl-H_4F, Asp120 in eMTHFR has been proposed to regulate the reactivity of FAD. The carboxyl group of Asp120 is thought to prevent the reduced anionic hydroquinone form ($FADH^-$) of FAD and pushes the equilibrium towards the reduced neutral hydroquinone form ($FADH_2$). The Asp120Asn exchange results in a higher midpoint potential of FAD and a 30% faster reduction of FAD by NADH. On the other hand, the Asp120Asn mutation reduces the overall reaction by 150-fold (*153*).

Position C is occupied by amino acids with a carboxamide group in all three reductases. In eMTHFR, Gln183 forms a polar contact with two nitrogen atoms of the pterin ring. The equivalent Asn178 in jMer and Asn177 in hMfr do not point towards methyl-H_4F in the models. This suggests that the side chains of the two asparagine residues move when the C_1 carrier binds. Notably, Aufhammer et al. described side-chain movement of Asp96 and Asn158 in the Mer structure from *Methanosarcina barkeri* (Asp96 and Asn178 in jMer) upon F_{420} binding. However, comparison of the structure of the apoenzyme and the binary complex structure of jMer did not show any significant changes in the conformation of these two residues (Figure 12B). Therefore, it is most likely that the conformation of Asp96 and Gln178 in jMer changes upon binding of the C_1 carrier and not upon binding of F_{420}.

In all three reductases, a hydrophobic residue of approximately the same volume is found at position B. In eMTHFR and jMer, a phenylalanine is placed (Phe223 in eMTHFR, Phe233 in jMer), whereas this position is occupied by a leucine in the ternary complex model of hMfr (Leu221). For eMTHFR, Phe223 has been shown to be involved in the binding of the C_1 carrier via hydrophobic and aromatic interactions, and the side chain undergoes substantial conformational changes depending on whether the C_1 carrier or NADH is bound (*121*). Notably, the phenylalanine is not strictly conserved among the MTHFRs. In human MTHFR, this position is occupied by a leucine (*159*). Leu221 also occupies this position in hMfr. In the ternary complex model, the PABA ring is located in a hydrophobic pocket formed by Leu221, Ile54 and Val11. In eMTHFR the hydrophobic pocket consists of Phe223, Leu212 and Leu277. In the ternary complex model of jMer, the hydrophobic pocket consists of Phe233, Val8 and Val230. Assuming that the binding mode of the C_1 carrier at positions C and D is the same in all three reductases, the absence of a phenylalanine and the corresponding absence of π-π stacking at position B in hMfr suggests that the binding of the C_1 unit is stronger in eMTHFR than in hMfr. This is reflected in the different K_m values for methylene-H_4F in eMTHFR (0.4 µM) and in hMfr (100 µM).

All three reductases have a glutamate residue at position A. For eMTHFR, Glu28 has been shown to be the key residue for catalysis. The Glu28Gln mutation rendered the enzyme inactive (*122*). The use of this mutant for protein crystallography is the only reported successful method to obtain a ternary complex of MTHFR (*121*). In the wild type eMTHFR, Glu28 is thought to protonate methylene-H_4F via a water molecule to form an iminium cation, which readily accepts the hydride from $FADH_2$ (*122*). In the modelled structures of hMfr and jMer, Glu9 and Glu6 are located at this position, respectively. The similar positions of these glutamate

residues suggest that they have an equivalent function and may be involved in the protonation of the corresponding methylene-tetrahydropterin.

Mutational analyses of the C_1 carrier binding site

The surprisingly common pattern of amino acids in the active sites of the three methylene-tetrahydropterin reductases eMTHFR, jMer and hMfr indicates that the active site geometries are very similar, despite the fact that these three enzymes share only a very limited degree of amino acid sequence identity. In the previous section, it was proposed that the amino acids at positions B, C and D are involved in the binding of the C_1 carrier and that the glutamate residues at position A are the key residues for the protonation of methylene-H_4F and methylene-H_4MPT. To test these hypotheses, systematic mutational analyses were performed and the results were compared with kinetic data of eMTHFR mutants reported in the literature (Table 5).

Mutation of the wild type amino acid residues at position B is associated with an increase in the K_m values for the C_1 carrier and a concomitant decrease in V_{max} values. jMer carries a phenylalanine at position B and exchange to alanine or leucine increased the K_m values for methylene-H_4MPT from 58 µM to 104 µM and 154 µM respectively. The V_{max} value was decreased from about 500 U/mg to 63 U/mg (jMer_Phe233Ala) and to about 370 U/mg (jMer_Phe233Leu). The exchange of Phe223 in eMTHFR to leucine increased the K_m for methylene-H_4F from 0.4 µM to 8 µM, and the exchange to alanine increased the K_m for methylene-H_4F to 93 µM. The V_{max} value for wild type eMTHFR most commonly found in the literature is approximately 4 U/mg (derived from a k_{cat} of 2.2 s^{-1}). However, in the study of the phenylalanine mutants, the authors determined a 5-fold higher k_{cat} of 10.4 s^{-1} (19 U/mg) for the wild type, while they determined a K_m value consistent with previous studies. A comparison of these data shows a slight increase from 10.4 s^{-1} to 14 s^{-1} (25 U/mg) for eMTHFR_Phe223Leu and a decrease to 2.9 s^{-1} (5 U/mg) for eMTHFR_Phe223Ala (*159*). Leucine was chosen as a substitute for phenylalanine because its side chain has almost the same volume (165 $Å^3$) as the phenyl ring of phenylalanine (194 $Å^3$) without being able to promote π-π stacking. In contrast to leucine, alanine has a smaller volume (90 $Å^3$), and the comparison of phenylalanine-leucine and phenylalanine-alanine mutants allowed the contribution of π-π stacking and hydrophobicity to be studied separately (*159*, *160*). This result supports the hypothesis that Phe233 in jMer is involved in the binding of the C_1 carrier, although a strong contribution of π-π interactions

cannot be concluded from the data because the K_m values for methylene-H_4MPT of jMer_Phe233Ala and jMer_Phe223Leu are not substantially different, as is the case for eMTHFR_Phe223Ala and eMTHFR_Phe223Leu. The approximately 5-fold higher V_{max} of jMer_Phe233Leu compared to the V_{max} of jMer_Phe233Ala indicates that the volume of the side chain at this position is important. In hMfr, position B is occupied by a leucine and not by a phenylalanine as in eMTHFR and jMer. This leucine is also strictly conserved in mycobacterial Mfrs. The exchange of Leu221 for phenylalanine or alanine increased the K_m values of methylene-H_4F from 163 µM to 357 µM and 706 µM, respectively. The V_{max} value decreased from about 18 U/mg to about 6 U/mg (hMfr_Leu221Phe) and to about 4 U/mg (hMfr_Leu221Ala). This finding supports the hypothesis that Leu221 is involved in the binding of methylene-H_4F. It also shows that probably no π-π interaction is introduced by the exchange towards phenylalanine, since in this case a higher binding affinity would be expected compared to the wild type. The fact that the K_m for methylene-H_4F of the Leu221Ala mutant is approximately twice that of the Leu221Phe mutant, together with a higher V_{max} value of the Leu221Phe mutant, indicates that the volume of the side chain is the only important parameter for the hydrophobic interaction, which is different from the case in eMTHFR.

Mutation of the wild type amino acid residues at position C is also associated with a large increase in K_m values for the C_1 carriers in eMTHFR and hMfr. In eMTHFR, this position is occupied by Gln183, and its replacement by glutamate or alanine increased the K_m values of methylene-H_4F from 0.4 µM to 108 µM and 104 µM, respectively. The Gln183Glu mutant does not show a substantial difference in the maximal reaction rate while the V_{max} value of the Gln183Ala mutant decreased from 4 U/mg to 0.5 U/mg (*161*). The same behavior was observed for the exchange of Gln177 in hMfr, which increased the K_m values for methylene-H_4F from 163 µM to 384 µM in the Gln177Glu mutant and to 565 µM in the Gln177Ala mutant. The V_{max} value decreased from 18 U/mg to about 3 U/mg in the Gln177Glu mutant and to 1.7 U/mg in the Gln177Ala mutant. Notably, the K_m value for NADH increased from 16 µM to about 120 µM in hMfr_Gln177Glu, indicating that the acidic site chain also has some effect on the binding of the reducing agent. In contrast to these results, the replacement of Gln178 in jMer did not lead to increased K_m values for methylene-H_4MPT. However, V_{max} is reduced from about 500 U/mg to about 14 U/mg (jMer_Gln178Ala) and 0.2 U/mg (jMer_Gln178Ala). The K_m values for F_{420} increased from 5 µM to 61 µM (Gln178Ala) and 27 µM (Gln178Glu). Since the backbone of Gln178 is involved in the formation of the F_{420} binding site, these results indicate a function in the architecture of the active site rather than in the binding of methylene-H_4MPT.

The mutation of the amino acids at position D resulted in an increase of the K_m values for the C_1 carrier in eMTHFR and jMer, but no significant change is observed for hMfr. In eMTHFR, the Asp120Asn mutant shows an increased K_m value for methylene-H_4F of 17 µM compared to the K_m value of 0.4 µM of the wild type and a decreased V_{max} value of 0.01 U/mg compared to 4 U/mg of the wild type V_{max} (*153*). The same result was observed for the exchange of Asp96Asn in jMer, which increased the K_m value of methylene-H_4MPT from 58 µM to 142 µM while the V_{max} decreased from about 500 U/mg to 20 U/mg. In contrast, the Glu55Gln mutant of hMfr did not show a significant increase in the K_m value for methylene-H_4F but a decrease in the maximal reaction velocity from 18 U/mg to 5.5 U/mg. These results support the hypothesis that the aspartate at position D in eMTHFR and jMer has the same function and is involved in the binding of their respective C_1 carrier. For hMfr, the binding mode may be slightly different in this part of the enzyme. For example, by rotating the pterin ring towards Gln178, the C_1 carrier would occupy almost the same position as previously proposed, interacting with the amino acids that have been shown to be involved in the interaction, and would not form a hydrogen bond with Glu55. In this context, it is also not surprising that position 55 is not strictly conserved and that alanine and valine are found at this position in addition to glutamate and aspartate. Taken together, these results show that, with two exceptions, positions B, C, and D have the same function and are involved in the binding of the C_1 carrier in all three reductases.

Position A contains a glutamate residue in all three reductases and replacement with a glutamine residue results in a large decrease in V_{max} without a significant change in the K_m values for the C_1 carrier. For eMTHFR, the K_m values of the Glu28Gln mutant have not been characterized, but the V_{max} is reduced from 4 U/mg to 0.0004 U/mg. It has also been proposed that Glu28 is the key catalytic residue involved in the protonation of methylene-H_4F to activate the C_1 unit for the reaction (*122*). In hMfr, the Glu9Gln mutant showed a decrease in the maximal reaction rate from about 18 U/mg to about 0.04 U/mg and the Glu6Gln mutant of jMer showed a decrease from around 500 U/mg to 2 U/mg . Notably, neither mutant showed a significant increase in the K_m for their respective C_1 carrier, suggesting that Glu6 in jMer and Glu9 in hMfr are only marginally involved in the binding of the C_1 carrier and are in fact the key catalytic residues for both reductases. To exclude that the exchange of the glutamate residues at position A in jMer and hMfr resulted in a perturbation of the active site, the apoenzyme crystal structures of jMer_E6Q and hMfr_E9Q were determined (Table S3) and comparison with the wild type structures revealed no differences in the active site architectures (Figure S10). These results supported the hypothesis that the key catalytic residue of all three

methylene-tetrahydropterin reductases is the same, that the geometry required for the catalytic mechanism is very similar, and that all three reductases share a common catalytic mechanism.

Table 5: Kinetic constants for the different mutants of eMTHFR, hMfr and jMer. The constants for eMTHFR were obtained from the literature and V_{max} was calculated using the given k_{cat} values and a molecular weight of 33.103 kDa for eMTHFR. Where the given k_{cat} values were not specified with respect to the substrate, the resulting values were placed in the middle of the corresponding row. References for the eMTHFR mutants are listed below the mutant name in parenthesis. nd = not determined.

Position	Enzyme	Mutation	Substrate	K_m [µM]	V_{max} [µmole min^{-1}mg^{-1}]	k_{cat} [min^{-1}]	k_{cat}/K_m [min^{-1}µmole^{-1}]
Wild type	eMTHFR	WT (*153*)	Methylene-H_4F	0.4 ± 0.1	4	132 ± 12	330
			NADH	3.5 ± 0.6	nd	nd	nd
	hMfr	WT	Methylene-H_4F	163 ± 62	18.1 ± 2.6	594 ± 68	3.9 ± 0.8
			NADH	16.0 ± 3.1	16.6 ± 0.7	545 ± 19	34.7 ± 4.4
	jMer	WT	Methylene-H_4MPT	57.7 ± 29.7	514 ± 137	18165 ± 3968	351 ± 90
			F_{420}	4.6 ± 0.1	199 ± 1	7037 ± 31	1525 ± 23
A	eMTHFR	Glu28Gln (*122*)	Methylene-H_4F	nd	0.0004	0.012	nd
			NADH	nd			nd
	hMfr	Glu9Gln	Methylene-H_4F	254 ± 59	0.041 ± 0.004	1.3 ± 0.1	0.005 ± 0.001
			NADH	42.8 ± 11.7	0.035 ± 0.004	1.1 ± 0.1	0.028 ± 0.004
	jMer	Glu6Gln	Methylene-H_4MPT	33.5 ± 9.6	2.0 ± 0.3	71.0 ± 8.4	2.2 ± 0.3
			F_{420}	4.3 ± 1.4	1.0 ± 0.1	36.4 ± 2.4	8.9 ± 1.8
B	eMTHFR	Phe223Ala (*159*)	Methylene-H_4F	93 ± 16	5.3	174 ± 30	nd
			NADH	140 ± 7			nd
		Phe223Leu (*159*)	Methylene-H_4F	8 ± 2	25.4	840 ± 120	nd
			NADH	236 ± 36			nd

	hMfr	Leu221Phe	Methylene-H_4F	357 ± 28	5.6 ± 0.2	184 ± 6	0.51 ± 0.02
			NADH	3.4 ± 0.8	2.7 ± 0.1	88.9 ± 1.4	26.9 ± 5.1
		Leu221Ala	Methylene-H_4F	706 ± 121	3.8 ± 0.4	126 ± 11	0.18 ± 0.01
			NADH	5.2 ± 0.5	1.2 ± 0.0	38.0 ± 0.3	7.3 ± 0.6
	jMer	Phe233Ala	Methylene-H_4MPT	104 ± 50	63.2 ± 18.7	2233 ± 541	23.1 ± 4.2
			F_{420}	1.8 ± 2.1	13.2 ± 2.2	467 ± 63	377 ± 814
		Phe233Leu	Methylene-H_4MPT	154 ± 96	377 ± 163	13327 ± 4714	97.9 ± 23.4
			F_{420}	3.1 ± 2.6	48.4 ± 8.4	1710 ± 242	1379 ± 1311
C	eMTHFR	Gln183Glu (*161*)	Methylene-H_4F	108 ± 36	4.9	162 ± 30	nd
			NADH	6.6 ± 0.7			nd
		Gln183Ala (*161*)	Methylene-H_4F	104 ± 13	0.5	17.4 ± 0.6	nd
			NADH	< 10			nd
	hMfr	Gln177Glu	Methylene-H_4F	384 ± 32	3.0 ± 0.1	98.6 ± 3.4	0.26 ± 0.01
			NADH	123 ± 38	3.2 ± 0.6	107 ± 15	0.9 ± 0.1
		Gln177Ala	Methylene-H_4F	565 ± 57	1.7 ± 0.1	55.7 ± 2.6	0.1 ± 0.0
			NADH	28.2 ± 7.1	0.7 ± 0.1	24.1 ± 1.4	0.9 ± 0.1
	jMer	Gln178Glu	Methylene-H_4MPT	19.8 ± 5.0	12.1 ± 1.1	429 ± 31	22.3 ± 3.1
			F_{420}	27.3 ± 6.8	14.3 ± 1.8	507 ± 53	18.9 ± 1.9
		Gln178Ala	Methylene-H_4MPT	23 ± 10	0.1 ± 0.0	3.3 ± 0.5	0.2 ± 0.0
			F_{420}	61 ± 67	0.2 ± 0.1	6.1 ± 3.7	0.03 ± 0.17
D	eMTHFR	Asp120Asn (*153*)	Methylene-H_4F	17 ± 3	0.01	0.44 ± 0.04	0.026
			NADH	< 3.5	0.001		
	hMfr	Glu55Gln	Methylene-H_4F	176 ± 64	5.5 ± 0.8	181 ± 20	1.1 ± 0.2
			NADH	5.6 ± 1.1	4.1 ± 0.1	134 ± 2	24.5 ± 3.7
	jMer	Asp96Asn	Methylene-H_4MPT	142 ± 27	19.6 ± 1.7	692 ± 49	4.9 ± 0.4
			F_{420}	1.6 ± 2.8	2.4 ± 0.3	84.7 ± 8.9	4.8 ± 47.7

After the systematic mutational analysis, it was possible to extend the model of the catalytic mechanism of MTHFR (*122*) to Mer and Mfr. The mechanism consists of two distinct steps, first a protonation of the C_1 carrier to activate the molecule, followed by a hydride transfer from the hydride donor to the activated C_1 unit (Figure 21). As the methylene group in

methylene-H_4F and methylene-H_4MPT is chemically a rather unreactive aminal, it is unlikely that a hydride can be directly transferred to this chemical species. Therefore, the key glutamate residue must first protonate the N10 of the tetrahydropterin C_1 carrier. This leads to the opening of the 5-membered imidazolidine ring and the formation of a positively charged intermediate iminium cation. The positive charge can be delocalized via the pterin ring system, stabilizing this intermediate state. In contrast to the uncharged methylene group, the positively charged iminium cation is a good hydride acceptor, which can be transferred from either $FADH_2$ in MTHFR, $F_{420}H_2$ in Mer or NADH in Mfr. This hydride transfer produces the product methyl-tetrahydropterin.

Several arguments are favoring the iminium cation hypothesis. The catalytic mechanism is similar to that of iminium catalysis, which belongs to organocatalysis and describes a catalyzed reaction pathway that starts with the formation of a catalytic iminium cation from a carbonyl substrate and an amine (*162*). The resulting iminium cation is more electrophilic and hence reactive than the initial carbonyl group and can undergo several reactions like 1,2-addition, 1,4-addition or cycloaddition. After successful reaction the initial amine is regained (*162*). In the case of the methylene-tetrahydropterin reductases, it is clearly not a classical iminium catalysis since no carbonyl substrate and no amine are directly involved in the reaction. However, the oxidation state of the methylene group in methylene-H_4F and methylene-H_4MPT corresponds to the oxidation state of formaldehyde, and the methylene derivatives can be generated by the reaction of formaldehyde with H_4F and H_4MPT, respectively. Furthermore, the formaldehyde-activating enzyme Fae catalyzes this condensation reaction in methylotrophic bacteria and probably in other archaea (*163*, *164*). It has also been shown that the formation of methylene-H_4F from H_4F and formaldehyde probably involves an iminium cation (*113*). Thus, the methylene group can be considered a biologically converted formaldehyde, which corresponds to the carbonyl substrate in iminium catalysis. The secondary amines in H_4F and H_4MPT then correspond to potential catalytic amines, and in particular the N5 is important as it is postulated to carry the iminium cation in the catalytic mechanism. Protonation by the key catalytic glutamate residue converts the methylene group to the active iminium cation form, which can undergo various reaction pathways, but in the case of methylene-tetrahydropterin reductases is limited to reduction by the hydride. This further suggests that activation to a 5-iminium cation is likely to be the key step in other methylene-H_4F or methylene-H_4MPT using enzymes. For the methylene-H_4F-using enzyme thymidylate synthase, it has also been postulated that a general acid converts methylene-H_4F to a reactive iminium cation (*165*). In addition, a 5-OH-methylene-tetrahydrofolate was found in the crystal structure of the

thymidylate synthase. This molecule is the product of the activated 5-iminium cation and an added water molecule (*114*). In the structure of the serine hydroxymethyltransferase, which generates a methylene group from the serine side chain in order to form methylene-H_4F, a glutamate is located near N10 (*166*) and the exchange of this glutamate for glutamine renders the enzyme inactive by maintaining the K_m values (*167*) suggesting a similar effect as for methylene-tetrahydropterin reductases.

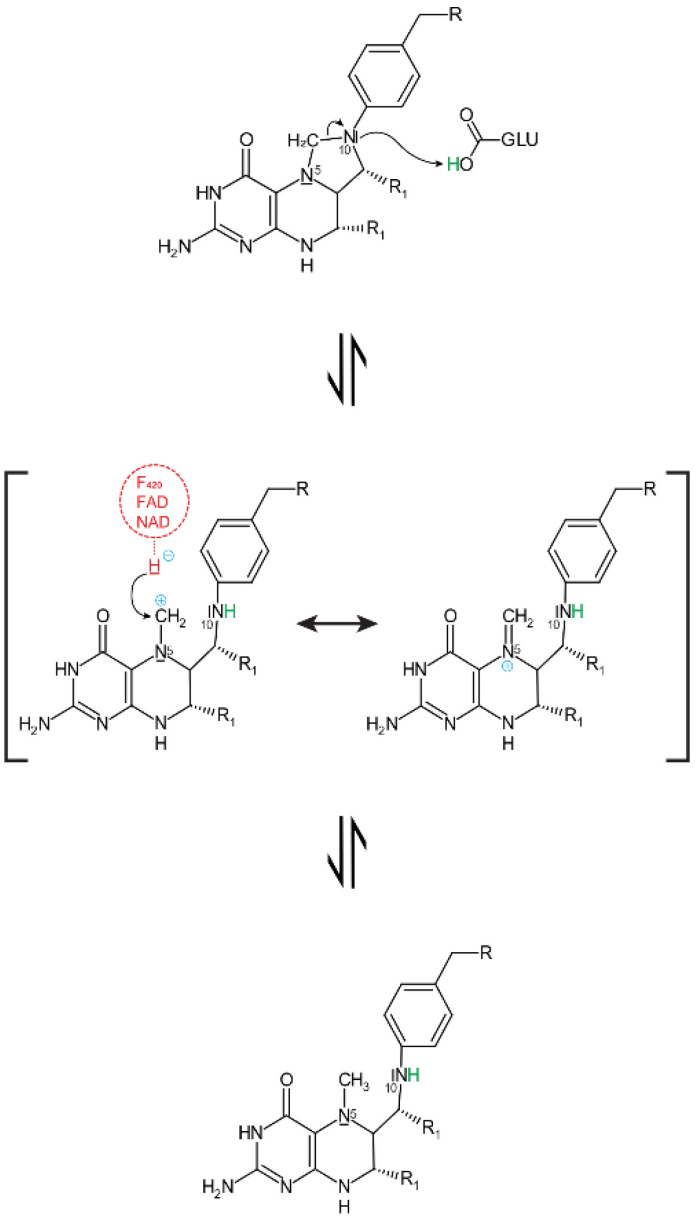

Figure 21: Postulated common catalytic mechanism for all methylene-tetrahydropterin reductases. In the first step, N10 of the pterin part of the C_1 carrier is protonated leading to the formation of an iminium cation. The positive charge of the iminium cation is delocalized over the pterin ring system, presumably stabilizing the intermediate state. The positively charged iminium cation is an excellent hydride acceptor. After hydride transfer, the reaction product is obtained.

Taken together, the mutational analyses showed that most of the amino acid residues have the same function in all three reductases and that the catalytic mechanism probably involves the formation of a positively charged iminium cation.

Docking of NADH and methylene-H_4F into hMfr

The knowledge of the involvement of different amino acids in the binding of the C_1 carrier was used to dock methylene-H_4F and NADH into the apoenzyme structure of hMfr. In the first step, NADH was docked into the Mfr-methyl-H_4F complex structure, where the methyl-H_4F was transferred from the aligned eMTHFR_E28Q methyl-H_4F complex (Figure 19C and D). Methylene-H_4F was then docked into the Mfr structure and two plausible poses were obtained, both with estimated binding affinities of –9 kcal/mol (Figure 22).

Model 1 resembles the ternary complex structure of eMTHFR and the modelled ternary complex of hMfr obtained by replacing FAD with NADH and rotating the methyl-H_4F-NADH pair (Figure 19E and F). The tip of the pterin ring of methylene-H_4F points upwards towards the active site ceiling. However, the pterin tip is also tilted towards the ribose moiety of NADH, resulting in some overlap. In model 2, the pterin ring of methylene-H_4F is tilted approximately 90° to the side, occupying a pocket present in the active site. In both models the distance between C11 and the hydride carrying atom of NADH is at a plausible distance, the Glu9 residue is close to N10 and all amino acids tested can in principle interact with methylene-H_4F, except Glu55 as mentioned above. The fact that in model 1 the geometry of NADH and methylene-H_4F leads to a slight overlap of the two molecules favors model 2 as a better representation of the actual binding mode. However, it does not exclude model 1, since the overlap is small and can be eliminated by a slightly different angle of the pterin ring system. In summary, the docked models are highly consistent with the models obtained from the functional alignment and represent a refined state of model building.

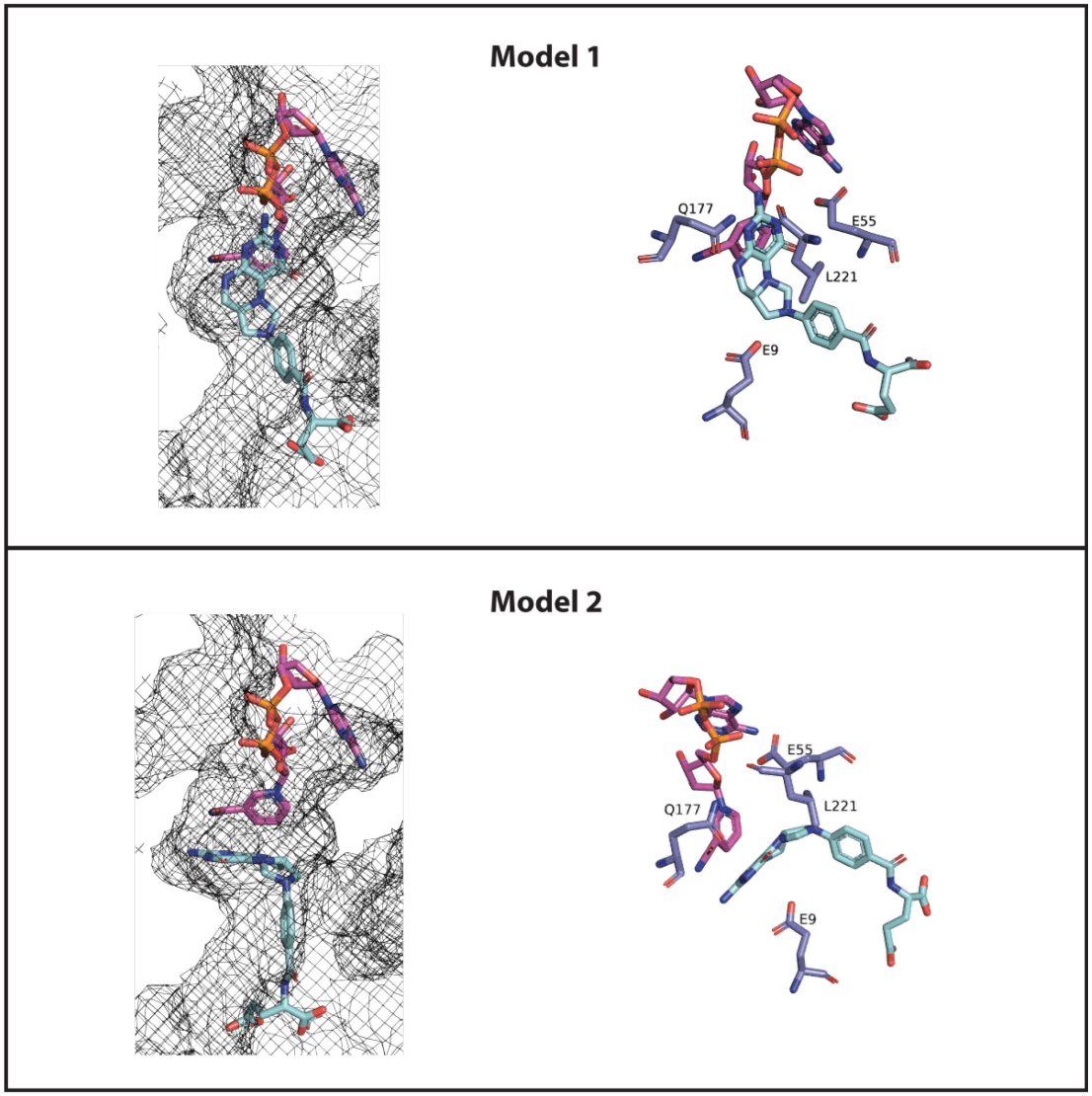

Figure 22: Docking models of hMfr. The docked NADH molecules are shown as a ball-and-stick models with purple colored carbon atoms, while the docked methylene-H_4F molecule has light blue colored carbon atoms. Amino acid residues are shown with dark blue carbon atoms. The putative active site cavity is shown as a black mesh. Model 1 and model 2 differ in the orientation of the pterin ring system. In model 1, the pterin points to the upper ceiling, while in model 2 it points to the left boundary.

Phylogenetic analyses of methylene-tetrahydropterin reductases

The surprising similarities in the active site geometries of the three methylene-tetrahydropterin reductases Mer, MTHFR and Mfr, together with the fact that they share a common catalytic mechanism, raise the question of their evolutionary relationship. There are several possible scenarios, depending on which feature is chosen as the common feature. In one scenario, Mer, MTHFR and Mfr could have evolved from one common ancestor.

Uncertainties in this scenario are very high because the ancient C_1-carrying pterin is unknown, as is the catalytic mechanism. However, the fact that the FAD-dependent MTHFR is present in most bacteria and eukaryotes provides an almost irrefutable argument for the presence of an FAD- or at least flavin-dependent MTHFR in the last universal common ancestor. From this point of view, the question arises whether Mer and Mfr are homologs of flavin-dependent MTHFRs or whether these two enzymes have evolved from convergent evolution. In the case of a common ancestor, this means that the origin of the three methylene-tetrahydropterin reductases would lie in a flavin-dependent enzyme that, for unknown reasons, used a ping-pong mechanism. In the bacterial lineage, this ancestral enzyme evolved into the modern FAD-dependent MTHFR, the modern FMN-dependent MTHFR found in acetogens and the flavin-independent Mfr. Accordingly, Mer also evolved from this ancestor, losing the prosthetic group, adapting a ternary complex mechanism and different C_1 carrier and reductant binding sites. In another scenario, the origin could be in an H_4MPT- and an H_4F-using ancestor. The ancestral version of a flavin-dependent MTHFR could be the H_4F-dependent enzyme that evolved into modern flavin-dependent MTHFRs and Mfrs, while Mer could have evolved separately. To shed some light on these possible scenarios, a phylogenetic tree was constructed. Seed sequences from the bacterial luciferase family (Table S4Table S4: Seed sequences for the Superfamily of Bacterial Luciferases.) and the FAD-linked reductase superfamily (Table S5) together with the amino acid sequence of hMfr were used for separate BLAST searches against the clustered non-redundant protein sequence database. The results were filtered to exclude any cluster with more than 90% sequence identity, and all clusters containing at least 3 members were selected. The query sequences were reinserted into the dataset and sequences marked as partial were removed. A multiple sequence alignment was performed using MUSCLE (*168*) and a maximum likelihood tree was constructed using IQTree (*169*). The best fitting evolutionary model was found to be WAG+F+I+G4 and the ultra-fast bootstrap method (*170*) was used to incorporate bootstrap values.

The constructed phylogenetic tree shows strong evidence for the clustering of several different protein families without a strong relationship between these families (Figure 23). The part of the tree containing F_{420}-dependent enzymes is consistent with previously reported trees. This places Mer in a direct relationship with bacterial luciferases and F_{420}-dependent dehydrogenases, as previously reported (*64*). Surprisingly, the proline dehydrogenases, which belong to the superfamily of FAD-linked reductases, split into an eukaryotic cluster and a prokaryotic cluster, the latter being close to the bacterial luciferases. The MTHFR cluster, consisting of prokaryotic and eukaryotic FAD-dependent MTHFRs, and the mycobacterial Mfr

cluster are isolated in the tree with no reliable connection to any other cluster. The tree is therefore an indication that Mfr, Mer and MTHFR are not directly related. However, since the eukaryotic and prokaryotic MTHFRs reliably cluster together, the tree supports the hypothesis of a flavin-dependent MTHFR in the last universal common ancestor. The evolutionary relationship between the C_1 carriers H_4MPT and H_4F and the whole pathway of C_1 unit reduction may help to resolve this issue, but remains elusive. It has been argued in the past that the biosynthesis of H_4MPT and H_4F is unrelated, although several steps are highly similar (*12*, *15*, *171*). This has also been suggested for the reduction series for C_1 units bound to H_4F and H_4MPT, for which most enzymes perform similar functions but are considered to be non-homologous (*15*, *172*). Recently, it has also been postulated that the last common archaeal ancestor, rather than the last common ancestor of all three domains, is the origin of the C_1 reduction pathway and that this H_4MPT-dependent pathway was then transferred to methylotrophic bacteria (*173*).

Taken together, the putative relationship between MTHFR, Mfr and Mer can neither be confirmed nor ruled out. The phylogenetic tree argues against a direct relationship, but a distant relationship seems more plausible. The fact that the flavin-dependent MTHFRs, and especially the FAD-dependent MTHFRs, occur in both bacteria and eukaryotes is a very strong indication of a common flavin-dependent ancestor. This would explain why flavin-dependent MTHFRs are found in acetogens, which together with methanogens are considered to be one of the oldest species on the planet (*172*, *174*). The pressing question of why most organisms on this planet carry an FAD-dependent MTHFR, while there seems to be no obvious benefit from this prosthetic group, is probably very closely related to the various FMN-dependent MTHFRs in acetogens and their physiological function. It may be that the original purpose of flavin-dependent MTHFRs was different and that the discovery of the physiological mechanism of acetogenic MTHFRs will resolve this issue. From this initial state, the most common FAD-dependent MTHFR may have evolved, retaining FAD as an evolutionary artefact, and for some unknown reason the flavin was replaced by NADH in mycobacteria. The fact that the MTHFR and Mfr clusters are isolated in the tree may indicate that links are missing. The data set is heavily unbalanced towards the bacterial luciferase superfamily, simply because of the amount of known family members. The other extreme is Mfr, which has not even crossed the boundary of the order *Mycobacteriales*, as no other order has been investigated. Therefore, a future investigation of Mfr in orders related to *Mycobacteriales* is of utmost importance, together with the investigation of the relationship between the two C_1 carriers H_4MPT and H_4F. Another important point is to investigate the common ancestor of the bacterial luciferase family. If Mer

or a Mer-like methylene-H_4MPT reductase is at the root of this family, this would be an argument favoring the evolution of Mer from flavin-dependent MTHFRs. If Mer evolved from another family member whose function was not the reduction of methylene-H_4MPT, this is a very strong argument for a separate evolution of Mer.

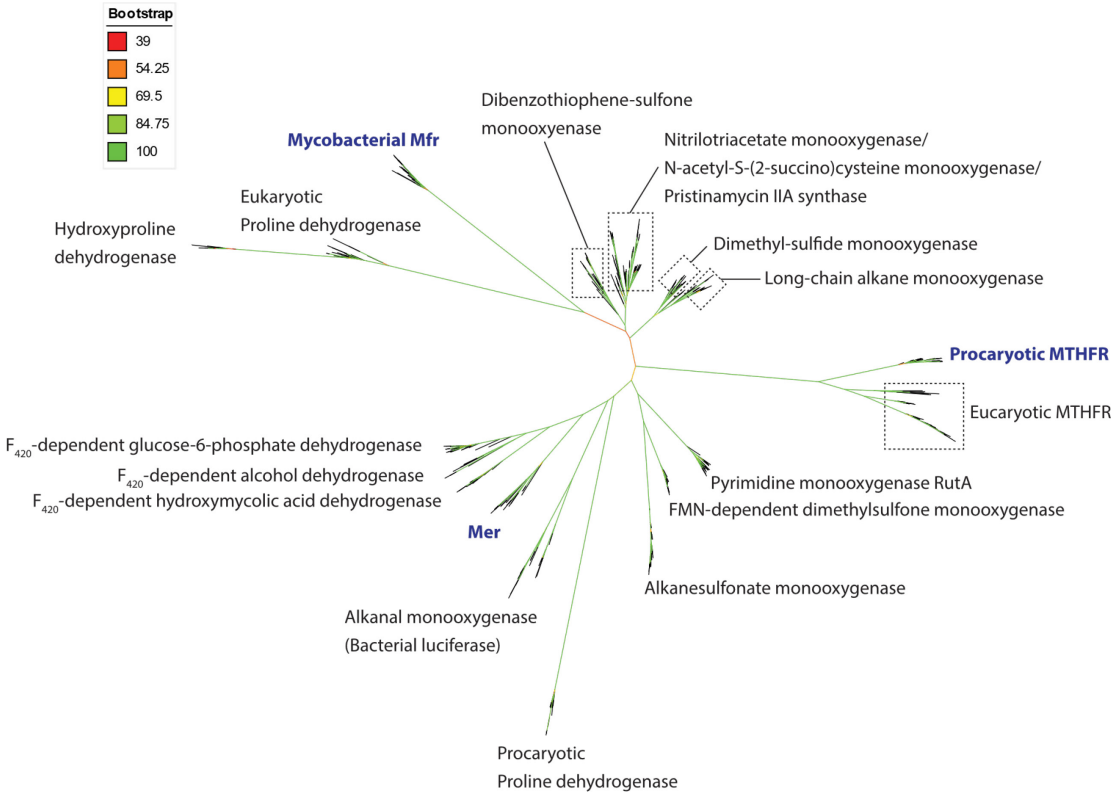

Figure 23: Unrooted phylogenetic tree of bacterial luciferase superfamily members, flavin-linked oxidoreductase superfamily members and Mfr members. The bootstrap values are indicated by a color scheme. The central part of the tree does not allow conclusions about the basal relationship between the tree superfamilies.

Accordingly, at this stage, nothing further can be deduced for the evolutionary questions from the data presented. However, the findings on the common catalytic mechanism are of importance for the construction of an Hmd mutant capable of reducing methylene-H_4MPT by cleavage of H_2.

Construction of Hmd mutants to enable the reduction of methylene-H_4MPT

The gained knowledge about the catalytic mechanism of methylene-tetrahydropterin reductases helps to construct Hmd mutants that might be able to reduce methylene-H_4MPT to methyl-H_4MPT. The basic concept involves the facts that the substrate first has to be protonated at N10 and the 5-membered imidazolidine ring has to open in order to form the reactive iminium cation. That implies that the Hmd mutant should have an acidic function in suitable proximity to N10 and enough space in the active site to enable the ring opening and the formation of the 5-iminium-H_4MPT cation.

The active site of Hmd in the closed protein conformation is located deep inside the protein, where methenyl- or methylene-H_4MPT are each embedded between the FeGP cofactor and two highly conserved methionine residues (Met252 and Met321) (Figure 24). The active site of Hmd is tailor-made to accommodate the H_4MPT derivates which are found in a planar conformation in the crystal structures (*41*). Thus, probably there is not enough space in the active site for a ring opening reaction and Met321 should be exchanged to a smaller residue like alanine or glycine. Furthermore, the side chain of the second methionine Met252 virtually shields the amine parts of the pterin rings from polar residues that might be able to protonate N10. Replacing Met252 with glutamate or aspartate could therefore allow the formation of the reactive iminium cation. Modelling of an exemplary double mutant, Hmd_M252D_M321G, showed that the removal of the methionine group at position 321 results in a significantly larger cavity than in the wild type. Furthermore, the acidic function of the introduced aspartate residues seems to be in a suitable position for protonation of the substrate (Figure 24).

In conclusion, using the knowledge of the catalytic mechanism of methylene-tetrahydropterin reductases, several Hmd mutants can be constructed that will be tested in the future for their ability to reduce methylene-H_4MPT. For this purpose, a detection method other than the UV/visible spectral change must be developed, as it is unlikely to be sufficient to detect low initial methylene-H_4MPT reduction activity. The design of a mass spectrometry-based method using purified H_4MPT, methylene-H_4MPT and methyl-H_4MPT as standards has been started.

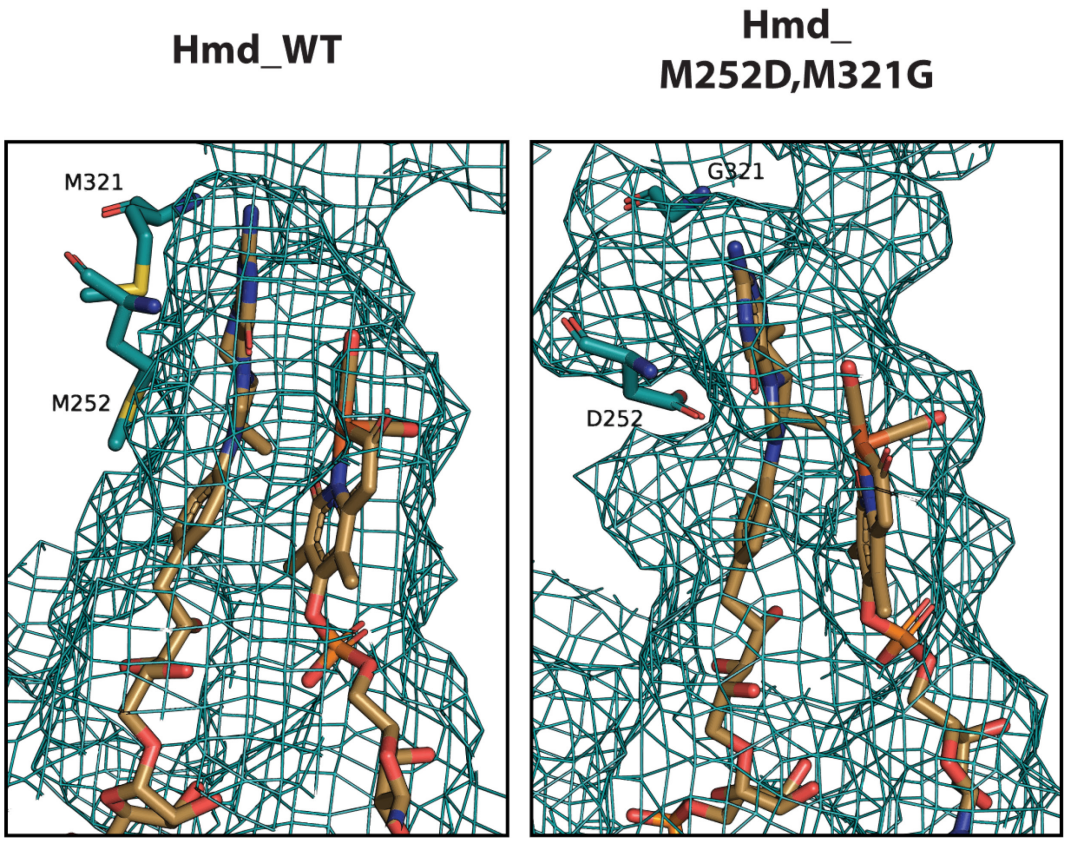

Figure 24: Construction of Hmd mutants designed to catalyze the reduction of methylene-H_4MPT. The mesh represents the active site cavity. The exchange of M321 to glycine presumably results in a larger cavity around the pterin ring of methylene-H_4MPT. The exchange of M252 to aspartate places an acidic function near N10 of methylene-H_4MPT that may protonate and thus activate methylene-H_4MPT for a second reduction step.

Conclusions and Outlook

In my Ph.D. thesis I addressed the question why the [Fe]-hydrogenase Hmd binds and catalyzes methylene-H_4MPT as a substrate in the H_2-generating reaction, but does not use H_2 in a reduction to methyl-H_4MPT. To this end, we first investigated whether the substrate of the native Hmd reduction, methenyl-H_4MPT^+, might possess special chemical properties that enable catalysis and are absent in a putative reduction of methylene-H_4MPT. For this purpose, a new NMR method based on the PHIP effect was applied in collaboration with researchers at the MPI Göttingen. The results showed for the first time that the reaction catalyzed by Hmd generates PHIP signals and that in the catalytic cycle of Hmd two different intermediate states polarize the bound H_2. Furthermore, we showed that a non-classical hydride binds to the iron ion of the FeGP cofactor. These results indicate that the methenyl character of methenyl-H_4MPT^+ is not required for catalysis.

The next step of my Ph.D. project was to investigate the catalytic mechanism of methylene-tetrahydropterin reductases, including the methylene-H_4MPT reductase Mer. Mer natively catalyzes the reduction of methylene-H_4MPT to methyl-H_4MPT, but unlike Hmd it is not a hydrogenase and therefore uses $F_{420}H_2$ as reducing agent. In a comparative study, the properties of the three types of methylene-tetrahydropterin reductases were investigated. For this purpose, the crystal structures of Mer as apoenzyme and in complex with the reducing agent F_{420}, as well as the apoenzyme structure of the flavin-independent methylene-H_4F reductase Mfr, were solved. Functional three-dimensional alignment revealed amino acid residues in the active sites of all three reductases that occur at the same position. In a systematic mutation study, these amino acids were mutated and the effects on the kinetic constants of the enzymes were compared with the values already known from the literature for the FAD-dependent MTHFR. It was found that most of the amino acids have the same function in all three reductases. Furthermore, the catalytic key residue was identified as glutamate by mutational analysis, leading to the extension of the postulated mechanism of FAD-dependent MTHFR to all methylene-tetrahydropterin reductases. The accumulated knowledge of amino acid functions was used to construct two different docking models of Mfr in complex with NADH and methylene-H_4F. Docking of methylene-H_4MPT into the jMer binary complex structure is planned for the future. Since the commonalities found in the active sites contrasted strongly with the low sequence identities and unshared sequence motifs, a phylogenetic analysis was performed to infer the relatedness of the reductases.

The knowledge gained was then used to design Hmd mutants that might catalyze the desired reaction in the future. For this purpose, a suitable detection method is required, since a simple UV/*Vis* measurement is not sufficient to detect the probably low activity. For this purpose, an MS-based method has already been developed. In the next step, the Hmd mutants will be purified and reconstituted with the isolated FeGP cofactor. The reduction assays will then be analyzed by MS for the increase in methyl-H_4MPT. If one or more mutants show the desired activity, they will be used as a starting point for semi-rational protein engineering. Furthermore, the exact function of the mutated methionine residues Met252 and Met321 is not known. However, since they are strictly conserved, an important function can be assumed. Therefore, the Hmd mutants will not only be tested for their ability to reduce methylene-H_4MPT, but also the kinetic constants for the native Hmd reactions will be determined and the mutants will be tested for changes in PHIP effects using the developed NMR method. Furthermore, the NMR method has already been applied to study the F_{420}-reducing [NiFe]-hydrogenase Frh. First promising results showed PHIP effects similar to those observed with Hmd and can be used to find similarities as well as differences in the H_2 binding of the two hydrogenases.

Material and Methods

Chemicals and gases

All chemicals used in this work were purchased from either Sigma-Aldrich Chemie GmbH (Darmstadt, Germany) or Carl Roth GmbH + Co. KG (Karlsruhe, Germany). Gases were purchased from either Air liquide Deutschland GmbH (Düsseldorf, Germany) or Westfalen AG (Münster, Germany). Deionized water was prepared using the Purelab Flex water purifier (ServApure, Bay City, MI, USA). Methylene-H_4F and methyl-H_4F were obtained from Schircks Laboratories (Bauma, Switzerland).

Chemically competent *E. coli* cells and transformation

To meet the needs of the mutation projects, chemically competent *E. coli* cells were prepared based on the chemically competent cells of *E. coli* Top10 (Invitrogen), BL21 Star (DE3) (Invitrogen) and ArcticExpress (DE3) (Agilent). 200 ml of LB medium were inoculated with a cryoculture of the desired strain and incubated at 37 °C and 120 rpm. After reaching an OD_{600} of 0.4, the culture was cooled in an ice bath for 10 min and the solution was centrifuged at 3200 × g for 10 min at 4 °C using an Avanti JXN-26 centrifuge with a Beckmann JLA 10.500 rotor. The supernatant was discarded and the cell pellet was resuspended in 100 ml of 100 mM $CaCl_2$ solution. After an incubation period of 30 min at 4 °C, the solution was centrifuged at 3200 × g for 10 min at 4 °C using an Avanti JXN-26 centrifuge with a Beckmann JLA 10.500 rotor and the supernatant was discarded again. Finally, the cell pellet was suspended in 5 ml of 100 mM $CaCl_2$ solution supplemented with 15% (v/v) glycerol and aliquots of 100 µl were snap frozen and stored at −75 °C.

Irrespective of the strain, all chemically competent cells were transformed using the same procedure. 100 ng of the desired plasmid was mixed with 100 µl of chemically competent cells and incubated on ice for 30 min. The mixture was placed in a water bath at 42 °C for 45 s. The mixture was allowed to cool on ice for 10 min before 900 µl of 37 °C super optimal broth with catabolite repression medium (SOC) was added. The cells were then incubated at 37 °C with slow shaking for 1 h before plating on agar plates supplemented with the appropriate antibiotics.

Anaerobic solutions

For the preparation of anaerobic solutions, such as buffers used for anaerobic protein purification, assay buffers or anaerobic water, the solutions were either boiled for 15 min with a constant stream of 100% nitrogen gas or subjected to alternating cycles of vacuum and 100% nitrogen gas for 1 h with constant stirring. After both procedures, the solutions were transferred to an anaerobic chamber (Coy Laboratories, Grass Lake, MI, USA) filled with forming gas (N_2/H_2, 95%/5%) and equipped with a platinum catalyst to reduce molecular oxygen to water and silica gels to remove moisture from the chamber. Finally, the solutions were stirred overnight in the anaerobic chamber to remove traces of oxygen.

Cultivation of *Methanothermobacter marburgensis*

Methanothermobacter marburgensis (DSM 2133) was obtained from Deutsche Sammlung für Mikroorganismen und Zellkulturen (DSMZ). The strain was grown anaerobically in 10 l fermenters under continuous gas flow of 1.5 l/min with H_2/CO_2 (80%/20%) and H_2S (0.1%). The medium consisted of 40 mM NH_4Cl, 50 mM KH_2PO_4, 24 mM Na_2CO_3, 0.5 mM NTA, 0.2 mM $MgCl_2 \cdot 6\ H_2O$, 1 µM $CoCl_2 \cdot 6\ H_2O$, 1 µM $Na_2MoO_4 \cdot 2\ H_2O$, 20 µM resazurin, 50 µM $FeCl_2$. In the nickel-sufficient condition, 5 µM $NiCl_2$ was added to the medium. In the nickel-limited condition, $NiCl_2$ was omitted and double-distilled water was used for the preparation of the medium. When the culture reached an OD_{600} of 5-6, the fermenters were cooled in an ice bath and the cells harvested anaerobically by continuous flow centrifugation using a Heraeus 3049 continuous flow rotor at 15 000 rpm under a constant stream of N_2 and at 4 °C. The cells were transferred to glass bottles and sealed with butyl rubber stoppers in an anaerobic chamber. The glass bottles were filled with N_2 to ensure overpressure and stored at −75 °C.

Purification of H_4MPT derivatives and F_{420}

Approximately 130 g of *M. marburgensis* cells cultured under nickel-sufficient conditions were suspended in 130 ml of anoxic 50 mM MOPS/NaOH pH 6.8, filled into a brown amber bottle and sealed with a butyl rubber stopper. The bottle containing the cell suspension

was incubated at 60 °C in a water bath. In parallel, an anaerobic aqueous solution of 5% cetrimonium bromide (CTAB) was heated to 60 °C in a water bath. The warm CTAB solution was then added to the flask containing the cell suspension to a final concentration of 0.25 ml CTAB per 1 g cells. The solution was incubated at 60 °C for 6 min with constant swirling. After the 6 min incubation period, the flask was placed in an ice bath and allowed to cool for 30 min. The suspension was transferred to an anaerobic chamber and all subsequent steps were carried out there. The pH of the cell suspension was adjusted to pH 3 using 100% formic acid. The suspension was centrifuged thereafter at 13 000 × g for 40 min at 4 °C in an Avanti JXN-26 centrifuge with a Beckmann JLA 10.500 rotor. The supernatant is termed the CTAB supernatant and contains H_4MPT, while the debris is termed the CTAB pellet and contains F_{420}.

The CTAB supernatant was applied to a Serdolit PAD II column (50 ml column volume) equilibrated with 380 mM formic acid/NaOH buffer pH 3.0 (XAD buffer). The column was washed with 300 ml XAD buffer and elution was performed as a one-step gradient with 600 ml XAD buffer supplemented with 15% methanol. Fractions of 100 ml were taken and the UV/*Vis* spectrum was used to identify fractions containing H_4MPT. These fractions were pooled and completely evaporated under vacuum. 50 ml of water was added to the dried preparation and the pH was adjusted to pH 3.0 with formic acid. The solution was applied to a Serdolit PAD I column (50 ml column volume) equilibrated with XAD buffer. The column was washed with an aqueous solution of 0.1% (v/v) formic acid and eluted in a single step gradient using 100 ml of an aqueous solution containing 30% (v/v) methanol and 0.1% (v/v) formic acid. Fractions of 10 ml were taken and H_4MPT was identified from the UV/*Vis* spectra. The fractions were pooled and dried by evaporation at 4 °C. After the addition of water, the H_4MPT solution was stored in aliquots at −20 °C.

Methylene-H_4MPT was generated from H_4MPT by the addition of formaldehyde. Typically, 500 µl of a 2 mM H_4MPT solution was mixed with 15 µl of 200 mM formaldehyde. After incubation for 10 min at room temperature, the solution was completely dried by evaporation at 4 °C and 500 µl of water was added. Methylene-H_4MPT was stored at −20 °C.

To purify methenyl-H_4MPT^+ instead of H_4MPT, formaldehyde was added to the cell suspension together with CTAB. The formaldehyde converts H_4MPT to methylene-H_4MPT and the Hmd activity in the cell suspension oxidizes methylene-H_4MPT to methenyl-H_4MPT^+. The subsequent purification steps are identical to those described above for H_4MPT.

For the purification of F_{420}, three CTAB pellets were combined and diluted 1:4 in anaerobic water. The suspension was sonicated using a SONOPLUS GM200 (Bandelin) with a VS-70-T tip attached at 80% power of 100 W for the whole period of 15 min. The suspension was mixed 1:1 with 100% acetone, which was cooled at –20 °C for several hours, and the mixture was stirred in an ice bath for 30 min. The mixture was centrifuged on an Avanti JXN-26 centrifuge with a Beckmann JLA 10.500 rotor at 13 000 × g and 4 °C for 20 min. The supernatant was transferred to another vessel and the extraction was repeated twice by adding 50% (v/v) aqueous acetone cooled to –20 °C so that the solution diluted the cell debris 1:1. Finally, the three supernatants were combined and evaporated at 4 °C until the volume has decreased by at least half. The solution was then centrifuged again using an Avanti JXN-26 centrifuge with a Beckmann JLA 10.500 rotor at 13 000 × g for 20 min at 4 °C and applied to a QAE Sephadex A25 column (GE Healthcare) equilibrated with 500 ml of 50 mM Tris/HCl pH 7.5. The column was first washed with 500 ml 50 mM Tris/HCl pH 7.5 and then with 500 ml 300 mM formic acid in water. Elution was performed with a single step gradient of 500 ml 50 mM HCl in water. The F_{420} containing fraction was identified by recording a UV/*Vis* spectrum and comparing the change in absorption maximum under acidic and basic conditions. The combined fractions were evaporated at 4 °C until a small volume remained. The concentrate was desalted using a Sephadex G-10 column (Cytiva Life Sciences) equilibrated with water. The F_{420} solution was stored in aliquots at –20 °C.

Purification of native Hmd from *M. marburgensis* (mHmd)

Approximately 100 g of *M. marburgensis* cells were suspended in 200 ml of 50 mM potassium phosphate buffer at pH 7.0 and sonicated (80% power of 100 W with 6 times of 8 min on/7 min off cycles) using a SONOPLUS GM200 instrument (Bandelin) with a VS-70-T tip attached. The suspension was centrifuged at 30 000 × g for 30 min at 4 °C using an Avanti JXN-26 centrifuge with a Beckmann JA 25.50 rotor. Ammonium sulfate was added to the supernatant until 60% saturation was reached. After stirring in ice water for 20 min, the supernatant was centrifuged at 13 000 × g for 20 min at 4 °C using an Avanti JXN-26 centrifuge and a Beckmann JA 25.50 rotor. Ammonium sulfate was added to the supernatant to 90% saturation. After stirring for a further 20 min in ice water, the suspension was centrifuged at 13 000 × g for 20 min at 4 °C using an Avanti JXN-26 centrifuge and a Beckmann JA 25.50 rotor. The pellet was then dissolved in 15 ml of 50 mM MOPS/KOH at pH 7.0 and the

suspension dialyzed overnight at 4 °C against 50 mM citrate/NaOH using a 30 kDa cut-off dialysis tube. The dialyzed solution was centrifuged at 13 000 × g for 20 min at 4 °C using an Avanti JXN-26 centrifuge and a Beckmann JA 25.50 rotor and then applied to a Source 30Q column (300 ml column volume, Cytiva Life Sciences, USA) equilibrated with 50 mM citrate/NaOH pH 5.0. The column was washed with 50 mM citrate/NaOH pH 5.0 with 200 mM NaCl. Elution was performed with a linear NaCl gradient from 200 mM to 500 mM. Fractions of 10 ml were taken and neutralized immediately with 1.5 ml of 1 M MOPS/KOH pH 7.5. The fractions were assayed for Hmd activity and the corresponding fractions containing mHmd were pooled and concentrated on an Amicon Ultra-4 (30 kDa cut-off). The buffer was then exchanged to anaerobic H_2O using a Sephadex G-25 column (Cytiva Life Sciences, USA) equilibrated with anaerobic H_2O. The fractions containing mHmd were pooled and concentrated using an Amicon Ultra-4 (30 kDa cut-off). Finally, the purified mHmd was snap frozen in liquid nitrogen and stored at −75 °C.

Activity assay of Hmd

As the reaction of Hmd is reversible depending on the pH and the presence of molecular hydrogen, two types of Hmd assays can be used, an oxidative assay which monitors the oxidation of methylene-H_4MPT and a reductive assay which monitors the reduction of methenyl-H_4MPT^+.

For the oxidative assay, a 1 ml quartz cuvette (1 cm light path) containing 680 µl of anoxic 120 mM potassium phosphate buffer pH 6.0 with 1 mM EDTA under 100% N_2 was pre-incubated at 40 °C for 5 min. A final concentration of 20 µM methylene-H_4MPT was added and the assay was started by adding 10 µl of enzyme solution. The increase in absorbance at 336 nm was measured and activity was calculated from the extinction coefficient of methenyl-H_4MPT^+ (ε_{336} = 21.6 $mM^{-1}cm^{-1}$). The production of 1 µmole of methenyl-H_4MPT^+ in 1 min was defined as 1 unit.

For the reductive assay, a 1 ml quartz cuvette (1 cm light path) containing 680 µl of anoxic 120 mM potassium phosphate buffer pH 7.5 with 1 mM EDTA under 100% H_2 was pre-incubated at 40 °C for 5 min. A final concentration of 20 µM methenyl-H_4MPT^+ was added and the assay was started by adding 10 µl of enzyme solution. The decrease in absorbance at 336 nm was measured and the activity could be calculated from the extinction coefficient of methenyl-

H_4MPT^+ (ε_{336} = 21.6 mM^{-1}-cm^{-1}). The consumption of 1 µmole of methenyl-H_4MPT^+ within 1 minute was defined as 1 unit.

Extraction of the FeGP cofactor from mHmd

In order to extract the FeGP cofactor from the native mHmd enzyme, an extraction mixture was prepared. The mixture contained the following final concentrations: 60% (v/v) methanol, 1 mM 2-mercaptoethanol, 1% (v/v) ammonia and a maximum amount of 48 mg mHmd so that the protein concentration did not exceed 4 mg/ml in a total volume of 12 ml. The solution was incubated at 40 °C for 15 min and then cooled on ice. Proteins were separated from the FeGP cofactor trough filtration using an Amicon Ultra-4 (10 kDa cut-off). The flow through was collected and evaporated under vacuum to remove the methanol. Finally, the FeGP cofactor was dissolved and stored in 10 mM ammonium carbonate pH 9.0 with 1 mM 2-mercaptoethanol. The cofactor solution was stored in amber bottles in liquid nitrogen in a Dry Shipper CX-100 (MiTeGen).

To determine the concentration of the FeGP cofactor, the Hmd holoenzyme was reconstituted by mixing an excess of the Hmd apoenzyme from *M. jannaschii* jHmd (1 mg/ml final concentration) and 10 µl of the extracted FeGP cofactor in the assay solution in a 1 ml quartz cuvette (1 cm light path) at 40 °C. The oxidative Hmd reaction of the reconstituted holoenzyme was started by addition of 20 µM methenyl-H_4MPT^+. The FeGP cofactor concentration was calculated from the volumetric activity, assuming that 12 000 U/ml is equivalent to 1 mM FeGP cofactor, which is calculated as a possible specific activity of 300 U/mg of reconstituted jHmd.

Production of the jHmd apoenzyme

The untagged jHmd apoenzyme was produced in *E. coli* BL21(DE3) (New England Biolabs) and treated aerobically. Cells carrying the plasmid pET-24b(+) containing the *jhmd* gene under the control of an inducible T7lac promoter (*175*) were transferred from a cryo stock to a preculture of 100 ml Luria-Bertani (LB) medium containing 50 µg/ml kanamycin. The pre-culture was incubated overnight at 37 °C and used to inoculate 2 l of tryptone phosphate (TP) medium containing 50 µg/ml kanamycin. When the culture reached an OD of 1, *jhmd*

expression was induced with a final concentration of 1 mM isopropyl-β-D-thiogalactopyranoside (IPTG). After 3 h of expression, cells were harvested by centrifugation using an Avanti JXN-26 centrifuge and a Beckmann JLA 10.500 rotor at 13 000 × g for 5 min at 4 °C. Cells were stored at −20 °C unless immediately used for purification.

Cells that produced jHmd were suspended in 50 mM MOPS/KOH pH 7.0 supplemented with 2 mM DTT and disrupted by sonication (80% power of 100 W with 2 cycles of 5 min on/5 min off) using a SONOPULS GM200 sonicator (Bandelin) with a KE76 tip. The debris was removed by centrifugation at 30 000 × g for 40 min at 4 °C using an Avanti JXN-26 centrifuge with a Beckmann JA 25.50 rotor. The supernatant was heated in a water bath at 70 °C for 15 min. Denatured proteins were removed by centrifugation at 13 000 × g for 20 min at 4 °C using an Avanti JXN-26 centrifuge and a Beckmann JA 25.50 rotor. Ammonium sulfate was added slowly to a final concentration of 2 M. The precipitated proteins were removed by centrifugation at 13 000 × g for 20 min at 4 °C using an Avanti JXN-26 centrifuge and a Beckmann JA 25.50 rotor. The supernatant was applied to a Phenyl-Sepharose High Performance column (75 ml column volume, Cytiva Life Sciences) equilibrated with 50 mM MOPS/KOH with 2 mM DTT and 2 M ammonium sulfate. Elution was performed with a 200 ml linear gradient from 2 M to 0 M ammonium sulfate. Fractions of 10 ml were collected. The fractions containing jHmd were pooled and concentrated to 10 ml using Amicon Ultra-4 centrifugation filters (30 kDa cut-off). The solution was then desalted using a HiPrep G25 column (Cytiva Life Sciences) equilibrated with 50 mM MOPS/KOH pH 7.0 with 2 mM DTT. The apoenzyme was stored at −75 °C.

Reconstitution of the jHmd holoenzyme

For reconstitution of the jHmd holoenzyme, the apoenzyme and purified FeGP cofactor were mixed in a molar ratio of 0.75:1 to obtain a small excess of FeGP cofactor over the jHmd apoenzyme. The reconstitution mixture was incubated in 50 mM Tris/HCl pH 8.5 for 15 min at 8 °C in an anaerobic chamber. To remove unincorporated FeGP cofactor, the solution was washed three times in Amicon Ultra-4 filters (cut-off 30 kDa) with 10 mM MOPS/KOH pH 7.0. The reconstituted enzyme preparation was shock frozen in liquid nitrogen and stored at −75 °C.

Mutagenesis and heterologous overproduction of jMer

Robert White (Virginia Tech University) kindly provided the vector pT7-7_jMer containing the jMer encoding gene *MJ1534*. The plasmid was used for targeted mutagenesis of several amino acids using the QuickChange mutagenesis method. The degenerated primers for mutagenesis were designed using NEBaseChanger. A PCR was performed using 10 ng pT7-7_jMer as template, 0.5 µM degenerate primers (Table 6), 1× Q5 reaction buffer (New England Biolabs), 200 µM dNTPs (Thermo Fisher Scientific) and 0.02 U/µl Q5 High-Fidelity DNA Polymerase (New England Biolabs) in a 50 µl reaction volume. Thermocycling conditions were selected according to the manufacturer's recommendations and the annealing temperature was used as recommended by the NEBaseChanger (Table 6). After PCR, the template DNA was digested with DPNI at 37 °C for 1 hour. The preparation was purified using the NucleoSpin Gel and PCR Clean-up Kit (Macherey-Nagel) and the success of the PCR was determined by the UV/*vis* spectrum using a Nanodrop. The complete DNA preparation was used for transformation into chemically competent *E. coli* Top10 cells and the cell suspension was plated on agar plates containing 100 µg/ml carbenicillin. After colony formation, 5 ml of LB medium supplemented with 100 µg/ml carbenicillin was inoculated with one colony and grown overnight at 37 °C. The plasmid was isolated using the NucleoSpin Plasmid Kit (Macherey-Nagel) and sequenced by Eurofins using pT7-7_Seq_F and pT7-7_Seq_R as sequencing primers (Table 6). After conformation of the correct ORF, the corresponding plasmid was transformed into ArcticExpress (DE3) cells and plated on agar plates containing 100 µg/ml carbenicillin and 20 µg/ml gentamicin. One colony was inoculated into 5 ml of LB medium and incubated overnight at 37 °C. A cryo-culture was prepared by mixing 1 ml of 50% glycerol with 1 ml of the overnight culture and flash frozen. Cryo-cultures were stored at –75 °C.

A cryo-culture of *E. coli* ArcticExpress(DE3) containing the desired jMer variant was used to inoculate 100 ml of LB medium supplemented with 100 µg/ml carbenicillin and 20 µg/ml gentamicin. The pre-culture was incubated overnight at 37 °C with shaking at 120 rpm. The main culture contained 2 liters of pre-warmed TB medium supplemented with 100 µg/ml carbenicillin and 20 µg/ml gentamicin and was inoculated with 100 ml of the pre-culture. The main culture was incubated at 37 °C with shaking at 600 rpm until an optical density of 0.6-0.8 was reached. At this point, the *mer* gene expression was induced with 1 mM IPTG and the culture was transferred to 21 °C. After 21 h of expression, the culture was

harvested by centrifugation at 13 000 × g for 5 minutes at 4 °C. Cells were snap frozen and stored at –20 °C.

Table 6: List of primers used for mutagenesis of jMer and sequencing of the ORF of jMer in pT7-7_jMer. The degenerated nucleotides are marked in red.

Primer name	Sequence (5‘ → 3‘)	Purpose	Annealing temperature
jMer_E6Q _F	ATTTGGTATCGCATTTGTTCCAAAC	Glu 6 Gln exchange	59 °C
jMer_E6Q _R	TTCATATGTATATCTCCTTCTTAAAG		
jMer_D96N _F	CGGTCCAGGAAATAAGGCTACTT	Asp 96 Asn exchange	63 °C
jMer_D96N _R	ATACCTAAAACAGCTCTTCCTC		
jMer_N178A_F	AGTTTTAATTGCTGCATCAAACCCAAAAG	Asn 178 Ala exchange	58 °C
jMer_N178A_R	CCATCAGCAATCATACCAG		
jMer_N178D_F	AGTTTTAATTGATGCATCAAACCC	Asn 178 Asp exchange	58 °C
jMer_N178D_R	CCATCAGCAATCATACCAG		
jMer_F233A_F	AGTTGTTGCAGCCATCGCAGCAG	Phe 233 Ala exchange	62 °C
jMer_F233A_R	GGAACTGCTGCCTGCTTA		
jMer_F233L_F	AGTTGTTGCATTGATCGCAGCAG	Phe 233 Leu exchange	66 °C
jMer_F233L_R	GGAACTGCTGCCTGCTTA		
pT7-7_Seq_F	TAATACGACTCACTATAGGG	Sequencing of jMer	Not applicable
pT7-7_Seq_R	TTGATACCCTTCCTCAGAA		

Purification of jMer

For crystallization, approximately 40 g of cells were suspended in 160 ml of 50 mM Tris/HCl pH 7.5 with 2 mM DTT. The cell suspension was sonicated using a SONOPULS GM200 (Bandelin) with a 50% cycle and 160 W for 5 min per cycle and 5 min pause using a

TZ76 tip. A total of 2 cycles were performed. The disrupted cells were fractionated by centrifugation at 30 000 × g for 30 min at 4 °C. The supernatant was heated at 80 °C for 20 min and precipitated proteins were separated by centrifugation at 13 000 × g for 20 min at 4 °C. Ammonium sulfate was added to the supernatant to 60% saturation and the solution was stirred at 4 °C for 20 min. Precipitated proteins were removed by centrifugation at 13 000 × g for 20 min at 4 °C. The supernatant was applied to a Phenyl-Sepharose HP column (15 ml column volume) equilibrated with 50 mM Tris/HCl pH 7.5 containing 2 mM DTT and 2 M ammonium sulfate (buffer A). Buffer B contained 50 mM Tris/HCl pH 7.5 with 2 mM DTT and 10% (v/v) glycerol. The column was thoroughly washed with 20% buffer B. Elution was performed with a linear gradient from 20% to 100% buffer B in eight column volumes. jMer was eluted from 137 mS/cm to 5 mS/cm conductivity. The corresponding fractions were collected and desalted on a HiPrep G-25 column equilibrated with 50 mM Tris/HCl pH 7.5 containing 2 mM DTT. The desalted solution was applied to a ResourceQ column (6 ml column volume) equilibrated with 50 mM Tris/HCl pH 7.5 with 2 mM DTT. jMer was eluted by a linear gradient of 0-250 mM NaCl over fifteen column volumes. The jMer-containing fractions were collected and applied to a HiPrep Sephacryl S-200 HR equilibrated with 50 mM Tris/HCl pH 7.5 containing 150 mM NaCl and 2 mM DTT. The jMer-containing fractions were either used directly for crystallization or, after the addition of 5% (v/v) glycerol, were snap frozen in liquid nitrogen and stored at −75 °C.

A shorter protocol was developed for the characterization of jMer variants. Approximately 10 g of cells were suspended in 40 ml of 50 mM Tris/HCl pH 7.5 containing 2 mM DTT. The cell suspension was sonicated with a TZ73 tip attached to a SONOPULS GM200 (Bandelin) with a 50% cycle and 160 W for 5 min per cycle and 5 min pause. A total of 2 cycles were performed. The disrupted cells were fractionated by centrifugation at 30 000 × g for 30 min at 4 °C. The supernatant was heated at 80 °C for 20 min and precipitated proteins were separated by centrifugation at 13 000 × g for 20 min at 4 °C. The supernatant was diluted 1:1 in 50 mM Tris/HCl pH 7.5 with 2 mM DTT and applied directly to a ResourceQ column (6 ml column volume) equilibrated with 50 mM Tris/HCl pH 7.5 with 2 mM DTT. jMer was eluted by a linear gradient of 0-250 mM NaCl over fifteen column volumes. The jMer-containing fractions were collected and used for the kinetic characterization.

Activity assay of jMer

Master mixes for the activity assays were prepared in an anaerobic chamber. For preparing the master mix of the enzyme assay, brown serum bottles were filled with 100 mM Tris/HCl pH 8.0 supplemented with 10 µM 2-mercaptoethanol, the desired amount of purified F_{420}, the desired amount of H_4MPT and 3 mM sodium dithionite. The master mixes were incubated for 15 minutes at 55 °C in a water bath, in which F_{420} was reduced to $F_{420}H_2$. The enzyme assay was performed in an 500 µl anaerobic quartz cuvette (1 cm light path) with a final volume of 200 µl master mix. After preheating at 55 °C for 5 min, 15 mM formaldehyde (final concentration) was added, by which methylene-H_4MPT was generated from H_4MPT and residual dithionite was quenched. The enzyme reaction was started by the addition of 10 µl of enzyme solution. The reaction was monitored by measuring the oxidation of F_{420} by increase in absorbance at 401 nm. The catalytic activity was calculated from the extinction coefficient of F_{420} (ε_{401} = 25.9 mM^{-1}-cm^{-1}). One unit of jMer activity yields one µmole of F_{420} per minute.

Crystallization and structure determination of jMer

All crystallization experiments were carried out in an anaerobic chamber with a 95%/5% (N_2/H_2) atmosphere using the sitting drop vapor diffusion method and 96-well two-drop MRC crystallization plates (Molecular Dimensions). The plates were filled with reservoir outside the anaerobic chamber and carefully transferred inside. After 1 h of incubation, the plates were sealed with crystal clear tape (Duck) and incubated for one week before use. The final protein concentration in each drop was 20 mg/ml. For the drops containing F_{420}, a final F_{420} concentration of 2 mM was used. The crystal of the apoenzyme grew in a drop consisting of 35% (v/v) 2-methyl-2,4-pentanediol and 100 mM sodium acetate pH 4.5 and could be frozen directly in liquid nitrogen without additional cryoprotectant. The best crystal of the binary complex grew in a drop consisting of 25% (v/v) polyethylene glycol monomethyl ether 550, 100 mM MES pH 6.5 and 10 mM zinc sulfate. Prior to freezing, the crystal was treated with a cryoprotectant solution consisting of the reservoir solution mixed with 20% polyethylene glycol monomethyl ether 550 and F_{420} to a final concentration of 2 mM. A large number of experiments were also carried out using F_{420} in combination with either methylene-H_4MPT or methyl-H_4MPT at concentrations ranging from 2 mM to 10 mM substrate concentration in the droplets. Substrates were prepared as described above and buffers were normally exchanged

with pure water using a Sephadex G-10 column (Cytiva Life Sciences). Unfortunately, none of these conditions yielded a jMer complex bound to the C_1 carrier.

The diffraction experiments were performed at 100 K on the SLS beamline X10SA (Villigen, Switzerland) equipped with a Dectris Eiger2 16 M detector. The data set was processed with XDS and scaled with XSCALE (*176*). The phase problem was solved by the molecular replacement method using PHASER (*177*) with the structure of Mer from *Methanopyrus kandleri* as a search model (*55*). The model was built and improved in COOT (*178*) and refined using Phenix.refine (*179*) and Refmac (*180*). The final model was validated using the MolProbity (*181*) implementation of Phenix (*179*). Data collection, refinement statistics and PDB code for the deposited structure are listed in Table S1 and Table S3.

Construction, mutagenesis and heterologous overproduction of hMfr

The sequence of a gene encoding Mfr from *Mycolicibacterium hassiacum* (Uniprot accession number: K5BDY6) was optimized for *E. coli* codon usage and synthesized by GenScript as described below:

atgaccctgaataccattgcgctggaactggtgccgccgaatagcgatggcccggacggtggtcgtgaacaagcggttgaggatgcg
cgtaaggtgctgcgttgcgcggcggagaccggtctggcgggtcgtatcggccacgttatgatcccgggtatgattgaggaagacccg
gatcgtccgattccgatgaagccgaaaatggacgtgctggatttctggaccatcattcgtccggagctgccgggtatccgtggcctgtg
cacccaggttaccgcgtttctggacgaaccggcgctgcgtcgtcgtctgggtgacctgagcgcggcgggttttgatggcattgcgtttgt
gggtgttccgcgtaccatgaacgatggtgaaggtcatggtgttgcgccgaccgatgcgctgagcatgttcgcggatctggttccgaacc
gtggcgcgatcctgattccgacccgtgacggtgaacagggccgtttcgagtttaagtgcgaacgtggtgcgacctacggcatgaccca
actgctgtatagcgacgcgatcgtgggtttcctgcgtgagtttgcgcgtcgtaccgatcaccgtccggaaattctgctgagcttcggttttg
tgccgaagctggaagcgaaagttggcctgatcaactggctgattcaagatccgggtaacccggcggtggcggcggagcaagaattc
gttcgtcgtctggcgggtctggagccggcggacaagcgtaaactgatggttgatctgtacaaacgtgtgatcgacggtgttgcggatct
gggctttccgctgagcgtgcacctggaagcgacctatggtgttagcgtgccggcgtttgaaacctttgcggagatgctggcgtattgga
gcccgggtcagggttaa

The synthesized gene was cloned into pET-24b(+) between the NdeI and SalI restriction sites. The resulting plasmid was named pET-24b(+)_Mfr and was the starting point for the generation of Mfr mutants. Mfr mutants were generated by GenScript. All Mfr constructs were transformed into chemically competent *E. coli* BL21 Star (DE3) cells, the plasmids were

isolated and confirmed by sequencing as described above. Cryo-cultures were prepared as described above and stored at −75°C.

A cryo-culture was used to inoculate 100 ml of LB medium supplemented with 50 µg/ml kanamycin sulfate as a pre-culture. 100 ml of the pre-culture was used to inoculate two liters of pre-warmed TB medium supplemented with 50 µg/ml kanamycin. The culture was agitated at 600 rpm and cultivated at 37 °C until an OD_{600} of 0.6-0.8 was reached. Gene expression was induced by the addition of 1 mM IPTG. After 3 hours of induction at 37 °C, the cells were cooled in an ice bath and centrifuged at 13 000 × g for 5 minutes using an Avanti JXN-26 centrifuge and a Beckmann JLA 10.500 rotor. Cell pellets were stored at −20 °C until use.

Purification of hMfr

For the purpose of crystallization, approximately 3 g of cells were suspended in 12 ml of 50 mM Mops/KOH pH 7.0 supplemented with 2 mM DTT. The cell suspension was sonicated using a SONOPULS GM200 (Bandelin) with a 50% cycle and 160 W for 2 min per cycle and 2 min pause using a TZ73 tip. A total of 5 cycles were performed. The disrupted cells were fractionated by centrifugation at 30 000 × g for 30 min at 4 °C. The supernatant was heated at 50 °C for 20 min and precipitated proteins were separated by centrifugation at 13 000 × g for 20 min at 4 °C. Ammonium sulfate was added to the supernatant to 40% saturation and the solution was stirred at 4 °C for 20 min. Precipitated proteins were removed by centrifugation at 13 000 × g for 20 min at 4 °C. The supernatant was applied to a Phenyl-Sepharose HP column (10 ml column volume) equilibrated with 50 mM Mops/KOH pH 7.0 with 2 mM DTT and 1.6 M ammonium sulfate. The elution buffer contained 50 mM Mops/KOH pH 7.0 with 2 mM DTT. The column was thoroughly washed with 1.1 M ammonium sulfate in the equilibration buffer. Elution was performed with a gradient of 0.7 M ammonium sulfate in 50 mM Mops/KOH pH 7.0 containing 2 mM DTT. The corresponding fractions were collected and desalted on a HiPrep G-25 column equilibrated with 50 mM Mops/KOH pH 7.0 containing 2 mM DTT. The desalted solution was applied to a ResourceQ column (6 ml column volume) equilibrated with 50 mM Mops/KOH pH 7.0 with 2 mM DTT. Mfr was eluted by a linear gradient of 0-250 mM NaCl over fifteen column volumes. The Mfr-containing fractions were collected and applied to a HiPrep Sephacryl S-100 HR equilibrated with 20 mM MOPS/KOH pH 7.0 containing 2 mM DTT, 150 mM NaCl and 5% (v/v) glycerol. The Mfr-containing

fractions were either used directly for crystallization or snap frozen in liquid nitrogen and stored at –75 °C.

For the characterization of Mfr variants, a shorter protocol was designed. Approximately 3 g of cells were suspended in 12 ml of 50 mM Mops/KOH pH 7.0 with 2 mM DTT. The cell suspension was sonicated using a SONOPULS GM200 (Bandelin) at 50% cycle and 160 W for 2 min per cycle and 2 min pause using a TZ73 tip. A total of 5 cycles were performed. The disrupted cells were fractionated by centrifugation at 30 000 ×g for 30 min at 4 °C. The supernatant was heated at 50 °C for 20 min and precipitated proteins were separated by centrifugation at 13 000 × g for 20 min at 4 °C. The supernatant was diluted 1:1 with 50 mM Mops/KOH pH 7.0 with 2 mM DTT and applied directly to a ResourceQ column (6 ml column volume) equilibrated with 50 mM Mops/KOH pH 7.0 with 2 mM DTT. Mfr was eluted by a linear gradient of 0-250 mM NaCl over fifteen column volumes. The fractions containing Mfr were collected and used for characterization.

Activity assay of hMfr

The activity assay of Mfr was performed in 1 ml quartz cuvettes filled with 0.7 ml of 100 mM Mops/NaOH pH 7.0 under an N_2 atmosphere and incubated at 40 °C. In the standard assay, NADH and methylene-H_4F were added to final concentrations of 100 µM and 300 µM, respectively. For the kinetic analysis, the concentration of NADH and methylene-H_4F was set as the standard condition and the concentration of the counter substrate was varied. The assay was started by adding Mfr. The decrease in NADH absorbance at 340 nm was measured (ε_{340} = 6.22 $mM^{-1}cm^{-1}$). To determine the temperature dependence, the standard conditions were used and the cuvettes were incubated at different temperatures. For inhibition assays, isonicotinic acid, pyrazinoic acid and prothionamide were prepared as 10 mM stock solutions in anaerobic water and added to the enzyme assay described above to a final concentration of 1 mM.

Crystallization and structure determination of hMfr

Crystallization was carried out in an anaerobic chamber filled with a N_2/H_2 (95%/5%) gas mixture at 8 °C. For the sitting drop vapor diffusion method, 96-well screening plates (MRC 2 Well UVP, Hampton Research) were filled with 90 µl of reservoir solution and 48-well

optimization plates (MRC Maxi 48-well Crystallization Plate (Swissci), Hampton Research) were filled with 200 µl of reservoir solution. The crystallization plates filled with the reservoir solutions were placed in the chamber one week before crystallization to make the solution anaerobic. Initial crystals were found in several solutions of JB Screen Classic 1 (Jena Bioscience), for example 25% polyethylene glycol (PEG) monomethyl ether 2000. During optimization, small rod-shaped crystals and thin plates appeared in several PEG solutions (PEG1000-PEG 8000) in a concentration range between 10-30% (v/v) without additives and without buffers. The best diffraction crystal was a thin plate grown in 15% (v/v) PEG 6000 with a final concentration of 30 mg/ml Mfr in the drop over the course of 4 weeks. The best crystal was transferred to the reservoir solution supplemented with 30% (v/v) glycerol and frozen.

The diffraction experiments were performed at 100 K on the SLS beamline X10SA (Villigen, Switzerland) equipped with a Dectris Eiger2 16 M detector, the data set was processed with XDS and scaled with XSCALE (*176*). The phase problem was solved by the molecular replacement method using PHASER (*177*) with an AlphaFold (*148*) model of Mfr. The AlphaFold model was generated by the Colab Notebook (*182*) integrated in the CCP4 suite (*183*). The model was built and improved in COOT (*178*) and refinement was performed using Phenix.refine (*179*) and Refmac (*180*). The final model was validated using the MolProbity (*181*) implementation of Phenix (*179*). The data collection, refinement statistics and PDB code for the deposited structure are listed in Table S2 and Table S3.

Kinetic data processing and figure generation

The graphs and analyses of the kinetic constants were carried out using Python 3.7 with Jupyter Notebook (version 6.1.4) (*184*) as the development environment and the following packages: os, pandas (*185*), seaborn (*186*), matplotlib (*187*), numpy (*188*), scipy (*189*). The determination of the kinetic constants is based on the experimentally determined mean values of the specific activity and the corresponding standard deviation from three replicates per measurement point. The Michaelis-Menten equation (vi = vmax * substrate/(km + substrate)) was used as the corresponding function for scipy.curve_fit. The resulting standard deviations for the curve fitting process were calculated from the output of the pcov parameter from scipy.cuve_fit by calculating the diagonal of the resulting array and then taking the square root of the diagonal. The chemical structures were created using ChemSketch and edited using

Adobe Illustrator. The code can be found at my GitHub repository (https://github.com/ManuelGehl).

Molecular docking of NADH and methylene-H_4F into hMfr

Two different docking methods were used to dock the two substrates, methylene-H_4F and NADH into hMfr. NADH was docked by CB-Dock2 (*190*) into the Mfr-methyl-H_4F complex structure where the methyl-H_4F was transferred from the aligned eMTHFR_E28Q methyl-H_4F complex (*121*). Methylene-H_4F was docked into the Mfr structure using Autodock Vina (*191*)implemented in AMDock (*192*).

Phylogenetic tree construction

Seed sequences from the bacterial luciferase family (Table S4) and the FAD-linked reductase superfamily (Table S5) together with the amino acid sequence of hMfr were used for separate BLAST searches against the clustered non-redundant protein sequence database. The results were filtered to exclude any cluster with more than 90% sequence identity, and all clusters containing at least 3 members were selected. The query sequences were reinserted into the dataset and sequences marked as partial were removed. A multiple sequence alignment was performed using MUSCLE (*168*) and a maximum likelihood tree was constructed using IQTree (*169*). The best fitting evolutionary model was found to be WAG+F+I+G4 and the ultra-fast bootstrap method (*170*) was used to incorporate bootstrap values. The tree was visualized using iTOL (*193*).

Supplementary information

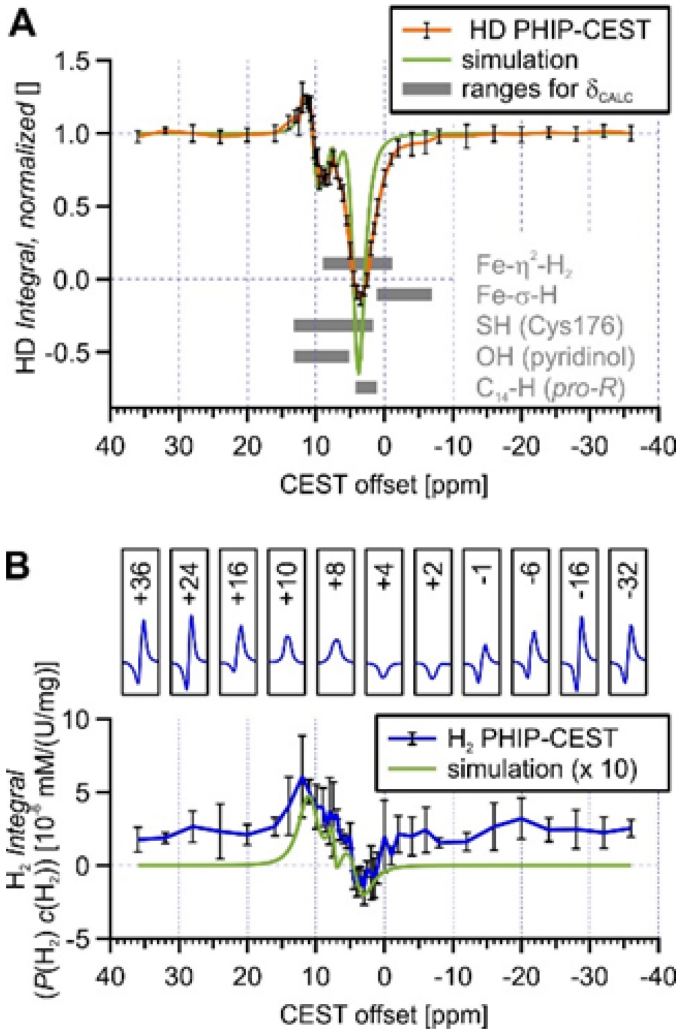

Figure S1: **(A)** The orange line represents the HD-PHIP-CEST profile obtained from multiple quantum filtered experiments averaged from five samples with error bars representing the standard deviation. An 8-second saturation with a γB1 value of 666 Hz was applied. The HD signal integral, normalized to the off-resonance integral, was measured at -36 ppm. A simulated HD-PHIP-CEST profile is superimposed in green. The grey shading indicates the computed chemical shift ranges (δ_{CALC}) derived from various QM/MM models for the corresponding chemical species. **(B)** The H_2-PHIP-CEST experiment involved a 2-second saturation with a γB1 value of 1333 Hz. The top portion of the figure displays the observed H_2 line shape at different offsets after irradiation. The bottom section illustrates the H_2-line integral, which has been normalized by the sample activity for hydrogen isotope exchange. The average data from three samples is presented, with error bars representing standard deviations. A simulated profile, obtained using the same simulation parameters as panel A, is displayed in green. Figure adapted from (*135*).

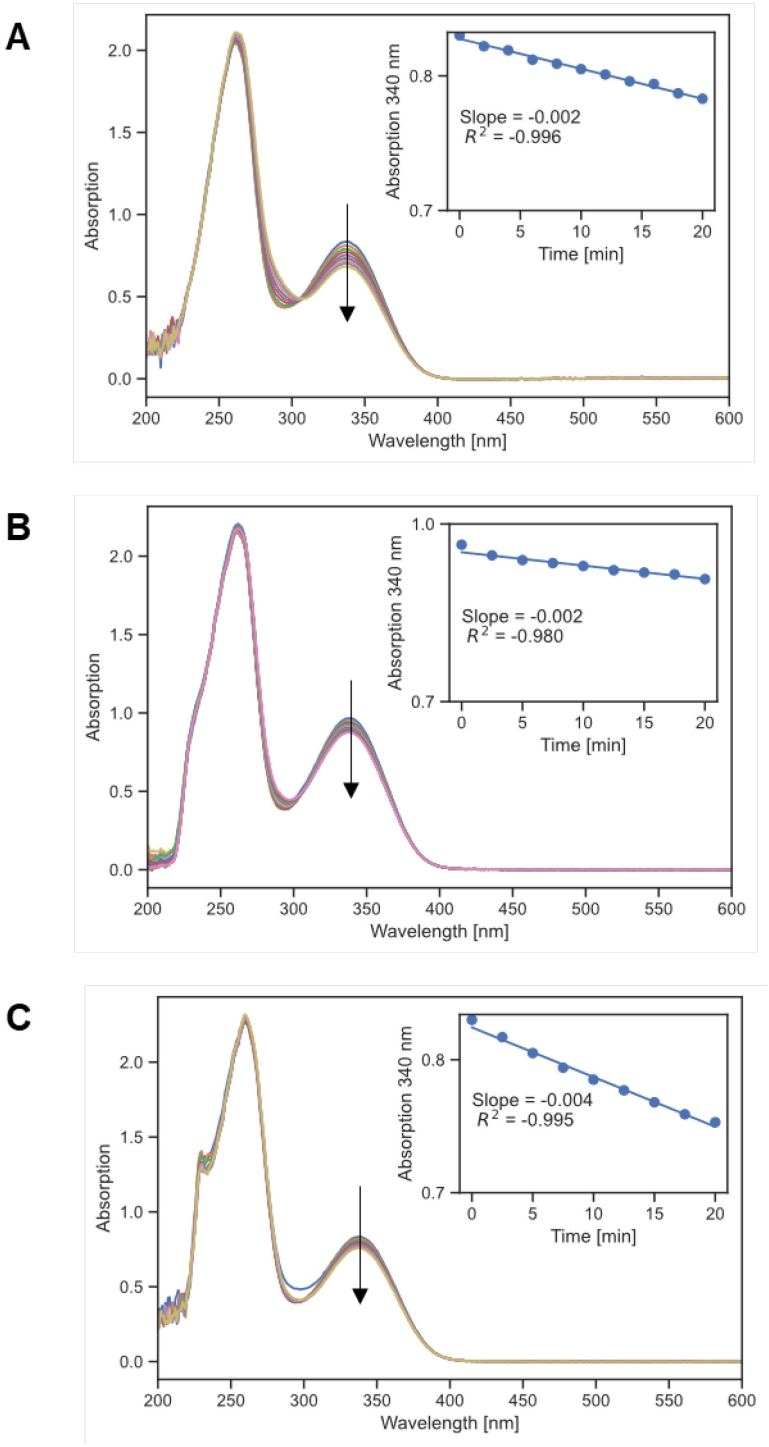

Figure S2: UV/*vis* spectrum change of 150 µM NADPH, 150 µM methylglyoxal and 0.2 mg/ml **(A)** or 2 mg/ml **(B)** jMer preparation. The negative control **(C)** consisting of 150 µM NADPH and 150 µM methylglyoxal without enzyme shows no differences in absorption decrease at 340 nm. The inlets show the extracted absorption at 340 nm over time for 20 min, the corresponding slope and the coefficient of determination.

Table S1: Structure determination statistics for jMer apoenzyme and the binary complex of jMer and F_{420}.

	jMer Apoenzyme	**jMer + F_{420}**
Resolution range (Å)	46.25 - 1.8 (1.864 - 1.8)	31.39 - 1.902 (1.97 - 1.902)
Space group	*P* 2_1 2_1 2_1	*P* 4_1 2_1 2
Unit cell dimensions a, b, c (Å) α, β, γ (°)	 96.66, 96.28, 166.78 90, 90, 90	 95.91, 95.91, 166.02 90, 90, 90
Unique reflections [a]	144123 (14203)	60825 (5895)
Completeness (%) [a]	99.84 (99.54)	98.83 (97.16)
Wilson B-factor	33.65	47.64
Reflections used in refinement	144109 (14202)	60822 (5895)
Reflections used for R-free	2002 (200)	1998 (194)
R-work (%) [b]	17.86 (27.11)	21.95 (32.62)
R-free (%) [b]	19.64 (29.09)	25.25 (33.64)
Protein residues	1324	657
RMSD bond lengths (Å) [c]	0.008	0.014
RMSD bond angles (°) [c]	1.07	1.36
Ramachandran favored (%)	97.02	96.01
Ramachandran allowed (%)	2.45	3.84
Ramachandran outliers (%)	0.54	0.15
Rotamer outliers (%)	0.19	1.16
Clash score	4.11	6.58
Average B-factor	53.52	60.38

[a] Values relative to the highest resolution shell are within parentheses. [b] R_{free} was calculated as the R_{work} for 5% of the reflections that were not included in the refinement. [c] rmsd, root mean square deviation.

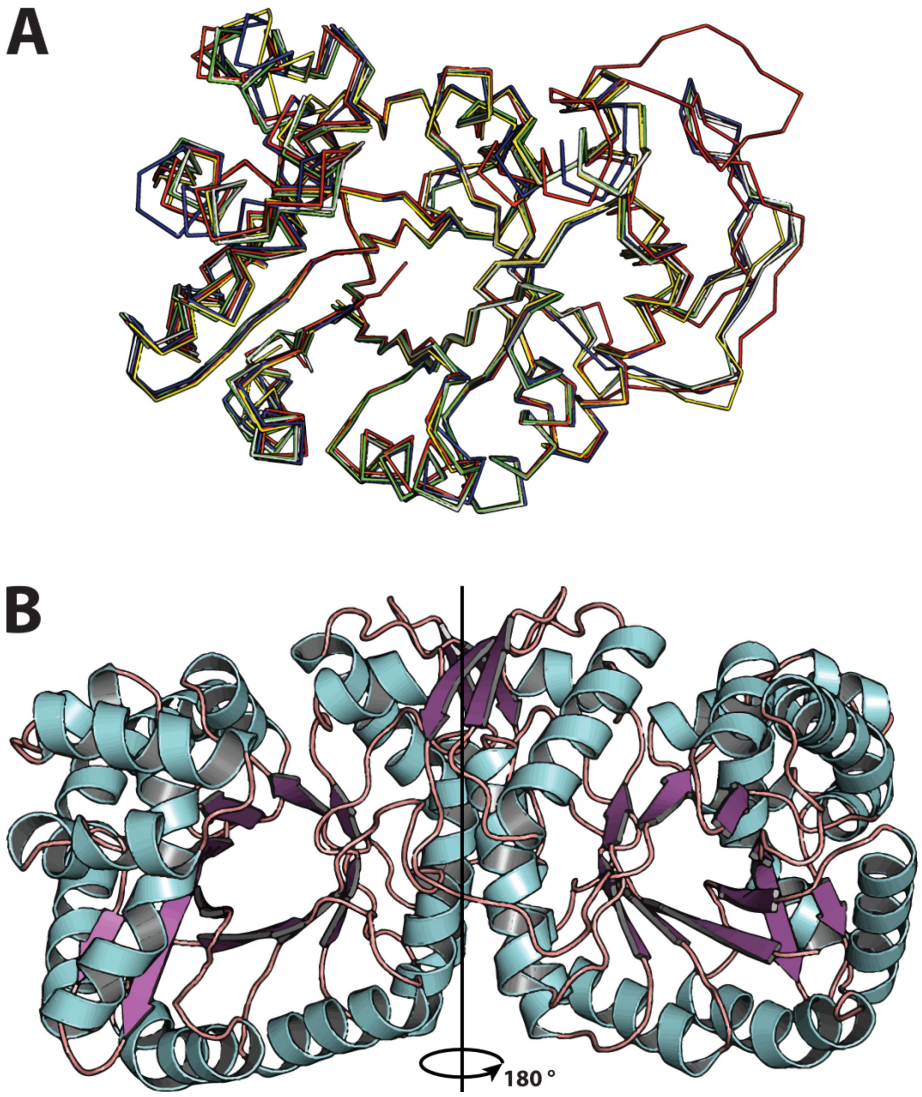

Figure S3: **(A)** Structural comparison of jMer (green) with Mer from *Methanopyrus kandleri* (red), from *Methanosarcina barkeri* (blue) and *Methanothermobacter marburgensis* (yellow). Only Cα chains are shown. The main structural differences are found in the loops. **(B)** Structure of the jMer apoenzyme dimer. The homodimer is the physiological form of jMer and is formed by a two-fold rotational axis located at the center of the protein-protein interface. The active site is located in the C-terminal half of the barrel core and is therefore on the opposite side in relation to each monomer.

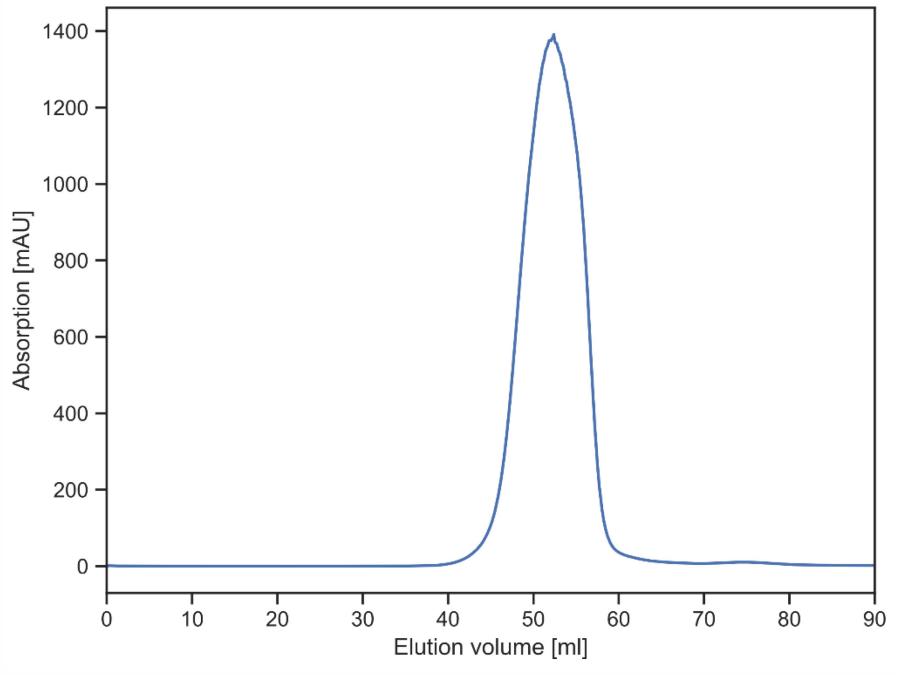

Figure S4: Size-exclusion chromatography of jMer using a HiPrep Sephacryl S-200 HR column. The peak centered around 50 ml elution volume corresponds to jMer and to a molecular mass of approximately 80 kDa.

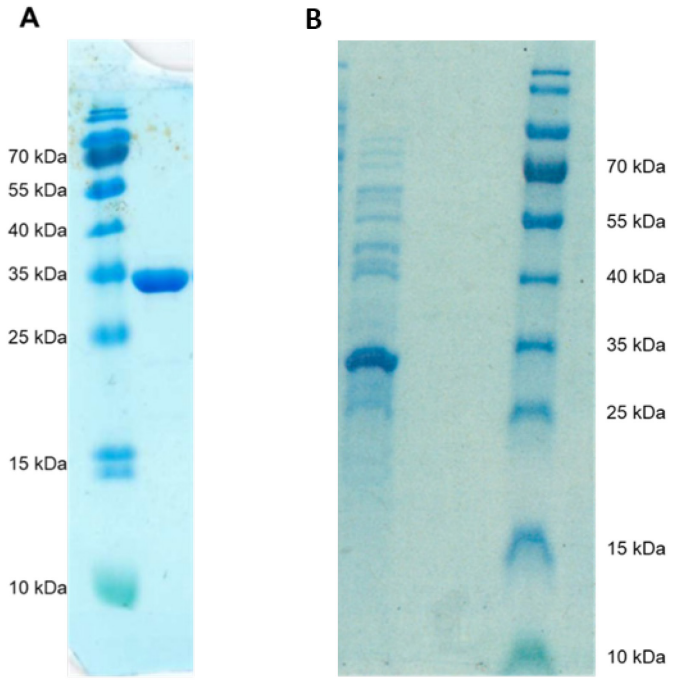

Figure S5: SDS-PAGEs of the different hMfr preparations. **(A)** Final preparation after the full-length purification method consisting of a total of three chromatographic steps. **(B)** Preparation using the shorter purification method with one chromatographic step. Both gels were loaded with 2 mg of the enzyme preparation.

Table S2: Structure determination statistics for hMfr.

	hMfr
Data collection	
Wavelength (Å)	1.0
Space group	*P* 4_3 2_1 2
Resolution (Å)	37.32 - 1.8 (1.9 - 1.8)
Cell dimensions a, b, c (Å) α, β, γ (°)	45.79, 45.79, 257.41 90, 90, 90
R_{sym} (%)[a]	9.3 (111.4)
$CC_{1/2}$[a]	0.996 (0.851)
I/σ_I[a]	9.0 (2.0)
Completeness (%)[a]	94.95 (87.48)
Redundancy[a]	4.3 (3.4)
Number of unique reflections[a]	25392 (2248)
Refinement	
Resolution (Å)	37.31-1.8
Number of reflections	25373
R_{work}/R_{free}[b] **(%)**	22.6/24.8
Number of non-hydrogen atoms	2487
Protein	2279
Ligands/ions	0
Solvent	208
Mean B-value ($Å^2$)	36.38
Molprobity clash score, all atoms	1.55
Ramachandran plot	
Favored regions (%)	99.65
Outlier regions (%)	0
RMSD[c] **bond lengths (Å)**	0.003
RMSD[c] **bond angles (°)**	0.59
PDB code	8BGR

[a] Values relative to the highest resolution shell are within parentheses. [b] R_{free} was calculated as the R_{work} for 5% of the reflections that were not included in the refinement. [c] rmsd, root mean square deviation.

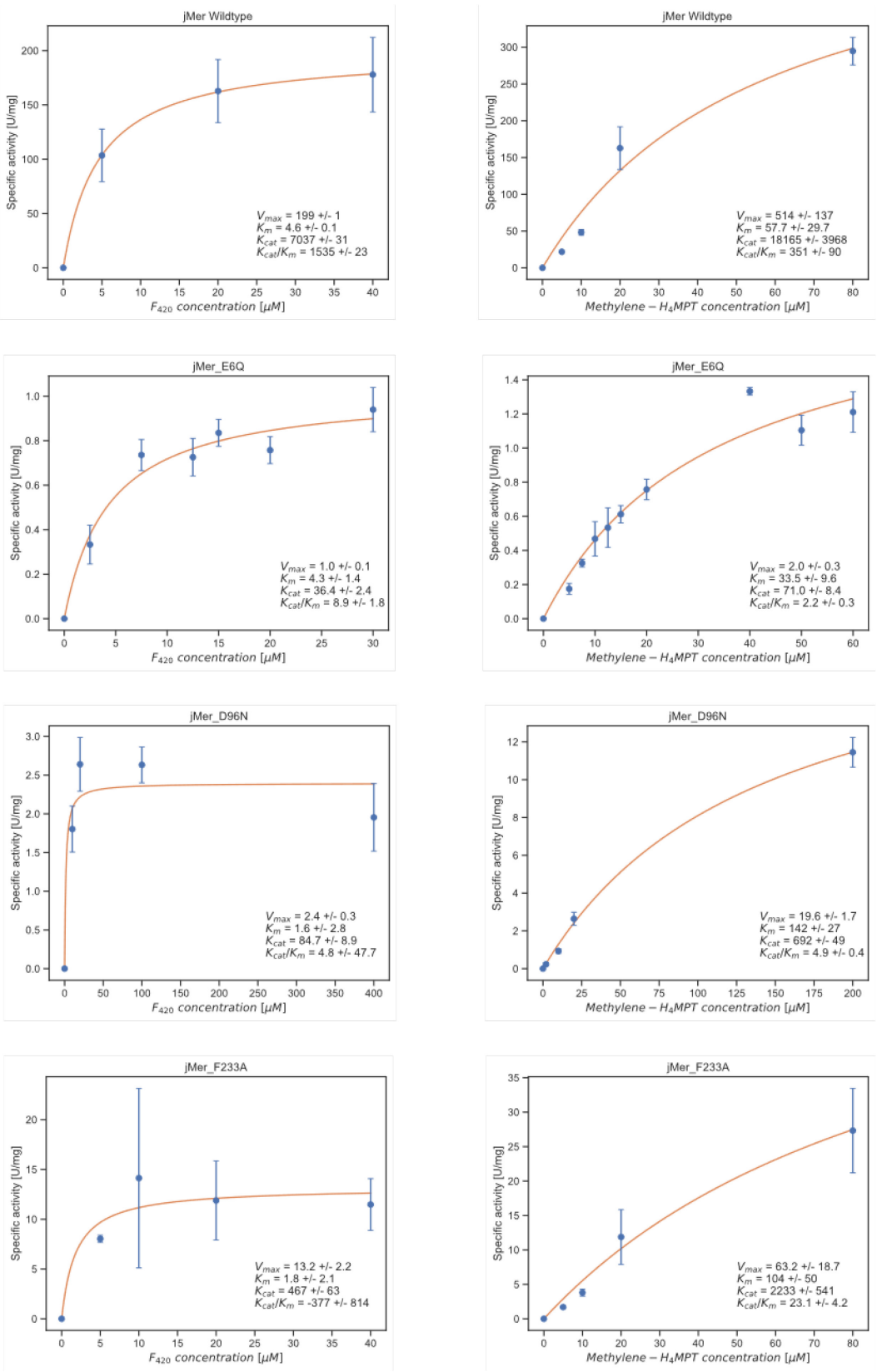

Figure S6: Kinetic fitting for the measurements of jMer wild type, jMer_E6Q, jMer_D96N, and jMer_F233A. Each measurement point consists of three independent measurements and the corresponding error bars are the standard deviation of the measurements. The kinetic constants are shown with the corresponding standard deviations derived from the kinetic fit (V_{max}, K_m) or from the calculation of the mean values (k_{cat}, k_{cat}/K_m).

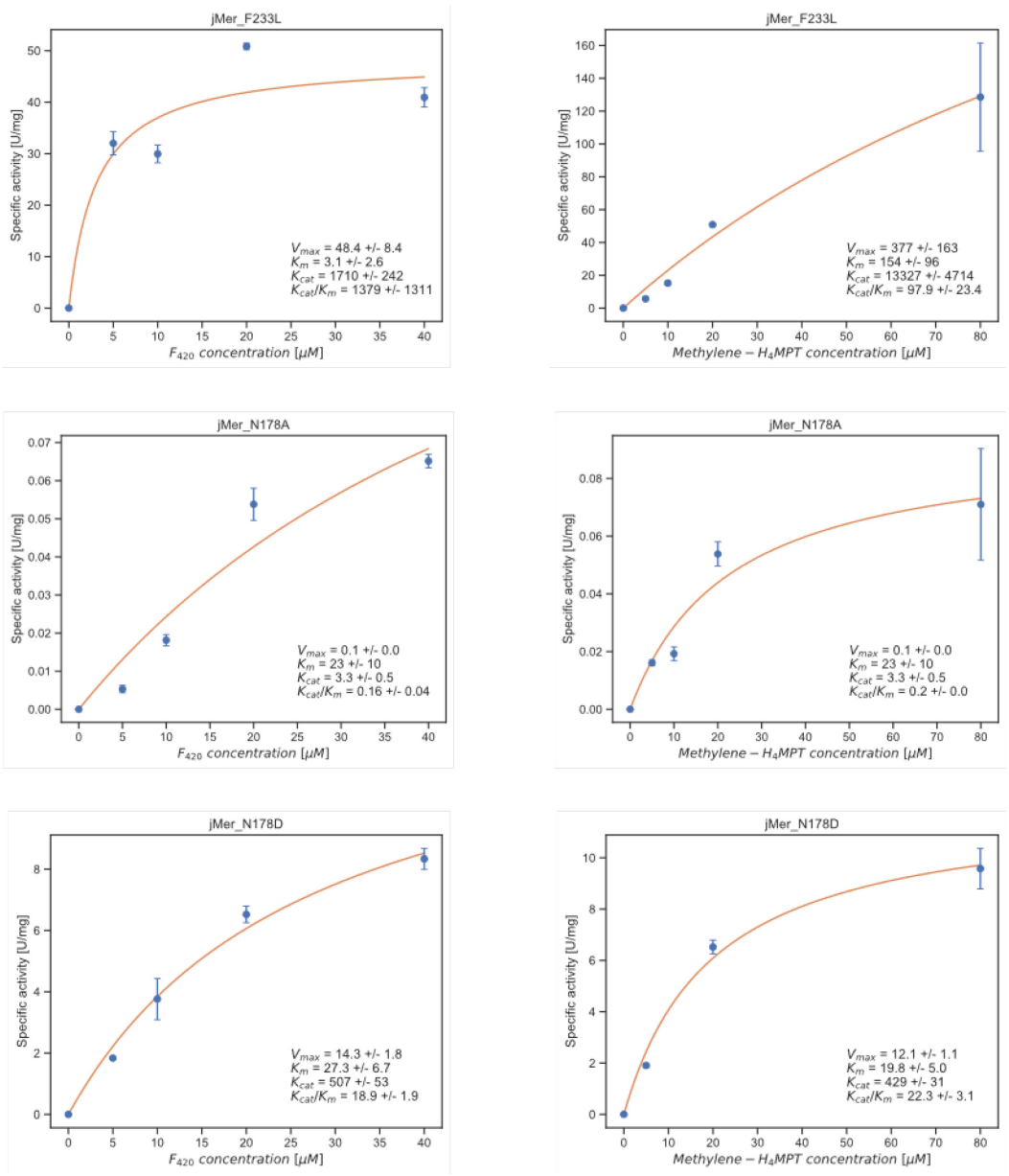

Figure S7: Kinetic fitting for the measurements of jMer_F233L, jMer_N178A, and jMer_N178D. Each measurement point consists of three independent measurements and the corresponding error bars are the standard deviation of the measurements. The kinetic constants are shown with the corresponding standard deviations derived from the kinetic fit (V_{max}, K_m) or from the calculation of the mean values (k_{cat}, k_{cat}/K_m).

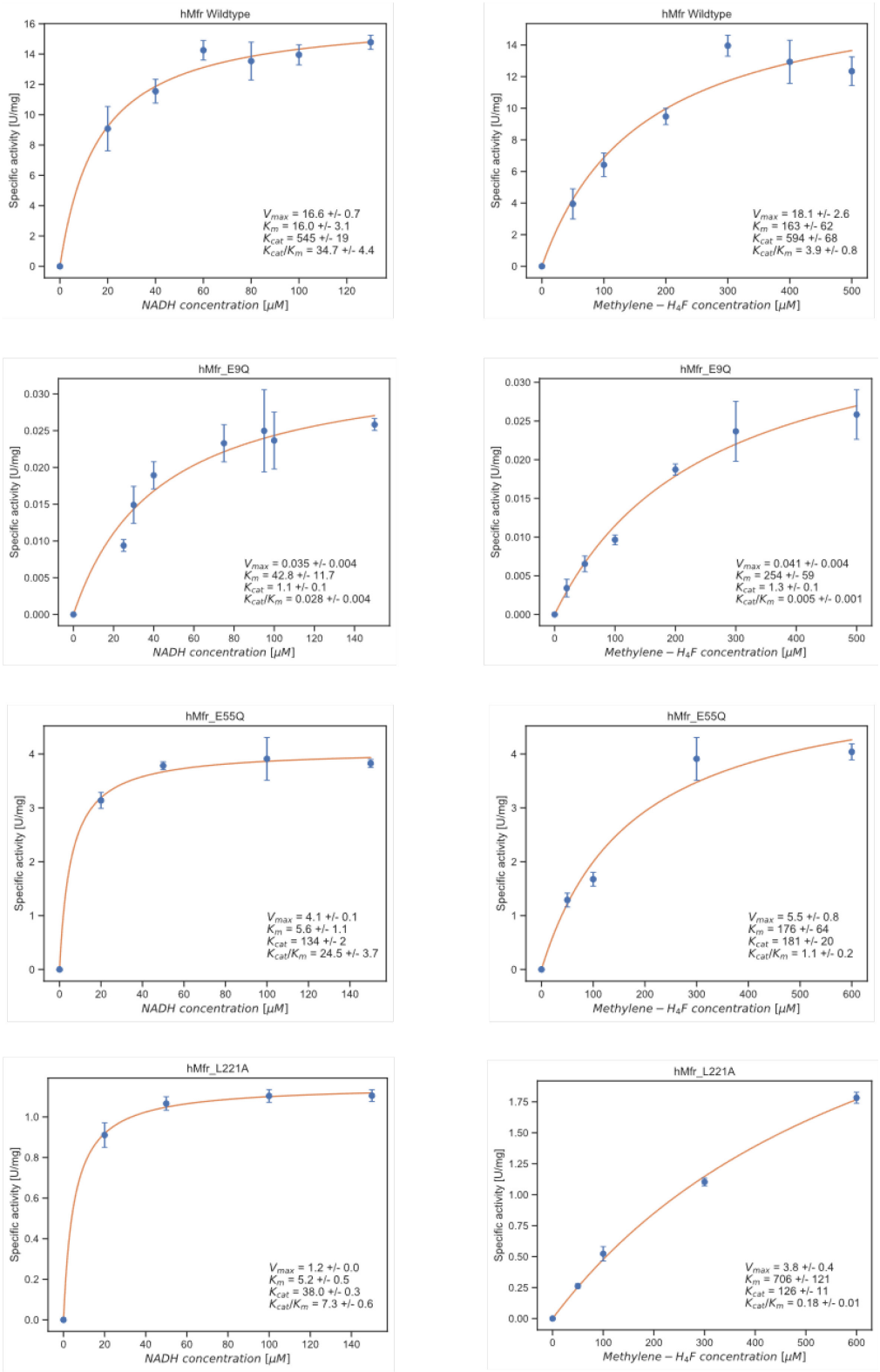

Figure S8: Kinetic fitting for the measurements of hMfr wild type, hMfr_E9Q, hMfr_E55Q and hMfr_L221A. Each measurement point consists of three independent measurements and the corresponding error bars are the standard deviation of the measurements. The kinetic constants are shown with the corresponding standard deviations derived from the kinetic fit (V_{max}, K_m) or from the calculation of the mean values (k_{cat}, k_{cat}/K_m).

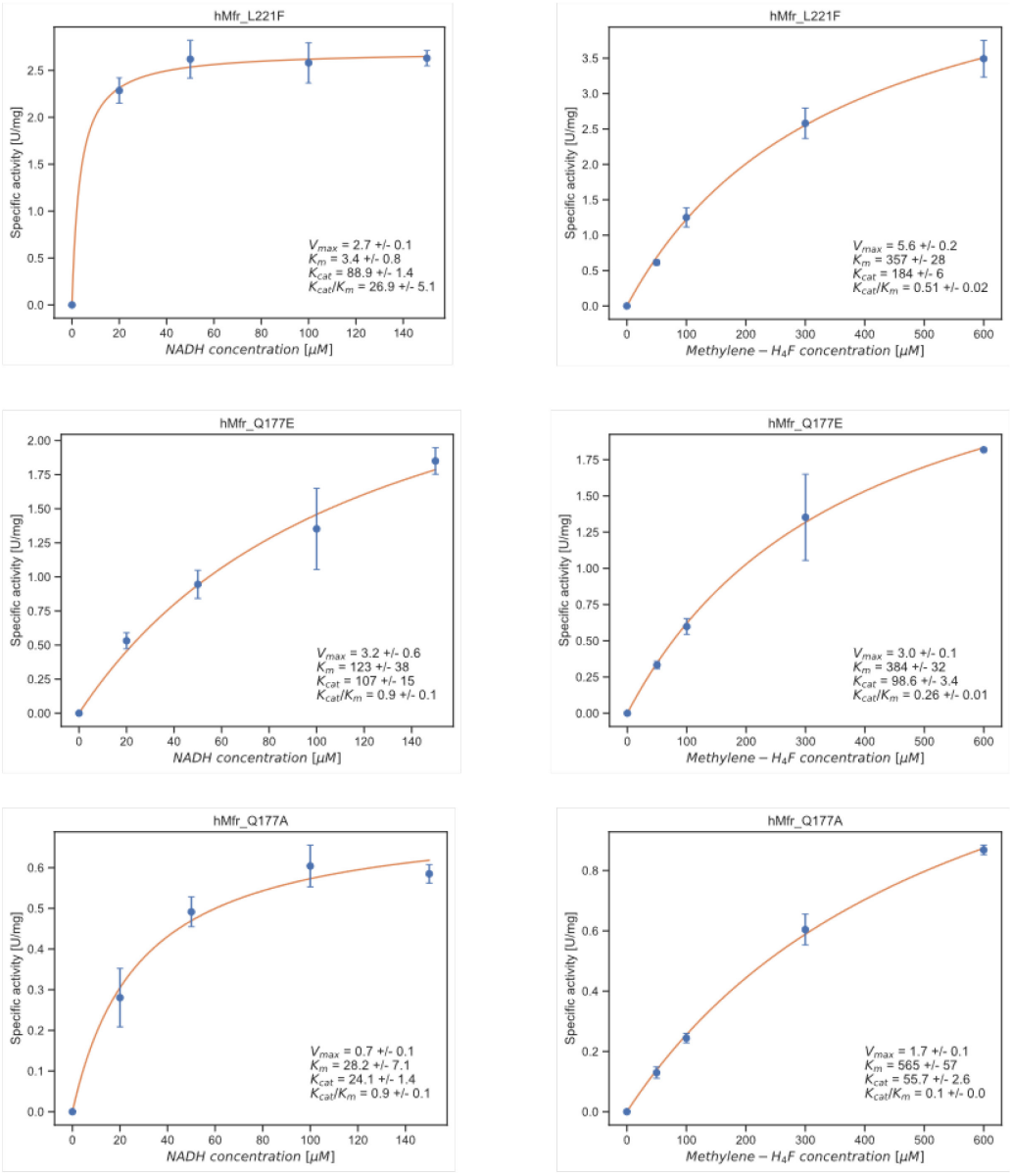

Figure S9: Kinetic fitting for the measurements of hMfr_L221F, hMfr_Q177E, and hMfr_Q177A. Each measurement point consists of three independent measurements and the corresponding error bars are the standard deviation of the measurements. The kinetic constants are shown with the corresponding standard deviations derived from the kinetic fit (V_{max}, K_m) or from the calculation of the mean values (k_{cat}, k_{cat}/K_m).

Table S3: Structure determination statistics for jMer_E6Q and Mfr_E9Q.

	jMer_E9Q	Mfr_E9Q
Resolution range (Å)	36.66 - 2.0 (2.072 - 2.0)	45.8 - 1.75 (1.813 - 1.75)
Space group	$I\,4_1\,2\,2$	$P\,4_3$
Unit cell dimensions a, b, c (Å) α, β, γ (°)	98, 98, 200.78 90, 90, 90	45.8, 45.8, 254.6 90, 90, 90
Unique reflections [a]	33180 (3259)	51862 (5183)
Completeness (%) [a]	99.07 (98.72)	98.91 (99.58)
Wilson B-factor	46.17	25.15
Reflections used in refinement	33124 (3237)	51850 (5183)
Reflections used for R-free	1998 (196)	1998 (196)
R-work (%) [b]	19.29 (39.87)	19.97 (33.18)
R-free (%) [b]	23.44 (43.02)	23.15 (39.49)
Protein residues	331	586
RMSD bond lengths (Å) [c]	0.007	0.006
RMSD bond angles (°) [c]	0.90	0.84
Ramachandran favored (%)	96.96	98.79
Ramachandran allowed (%)	2.74	1.21
Ramachandran outliers (%)	0.30	0.00
Rotamer outliers (%)	0.77	0.00
Clash score	6.54	3.39
Average B-factor	64.45	33.79

[a] Values relative to the highest resolution shell are within parentheses. [b] R_{free} was calculated as the R_{work} for 5% of the reflections that were not included in the refinement. [c] rmsd, root mean square deviation.

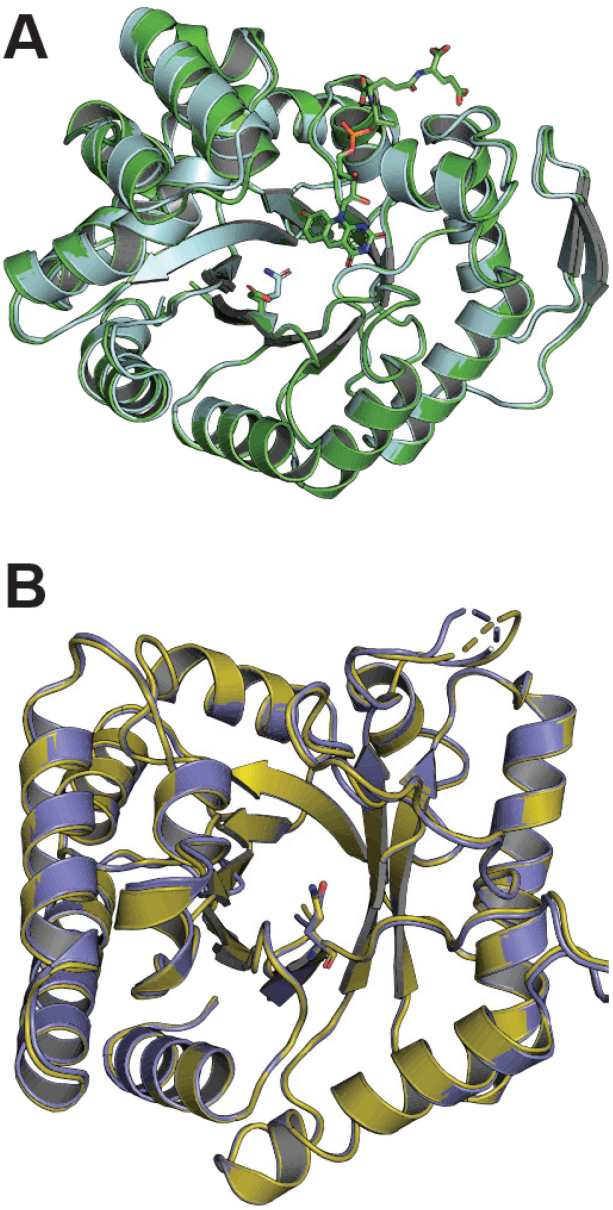

Figure S10: **(A)** Comparison of the structures of jMer wild type (green) and jMer_E6Q (light blue). **(B)** Comparison of the structures of hMfr wild type (dark blue) and hMfr_E9Q (yellow). The glutamate residues are depicted as ball-and-stick model

Table S4: Seed sequences for the Superfamily of Bacterial Luciferases.

Family	Seed	Organism	Structural prototype	NPCP bond	Reducing agent
Bacterial luciferase/NFP (IPR002103)	Alkanal monooxygenase alpha chain (P07740)	*Vibrio harveyi*	PDB: 1LUC	A74-A75	FMN
	Alkanal monooxygenase beta chain (P07739)	*Vibrio harveyi*	PDB: 1LUC	No	None
Nitrilotriacetate monooxygenase component A/pristinamycin IIA synthase subunit A (IPR016215)	Long-chain alkane monooxygenase (A4IU28)	*Geobacillus thermodenitrificans*	PDB: 3B9N, 3B9O	No	FMN
	Dimethyl-sulfide monooxygenase (E9JFX9)	*Hyphomicrobium sulfonivorans*	PDB: 6AK1	No	FMN
	N-acetyl-S-(2-succino)cysteine monooxygenase (P54950)	*Bacillus subtilis*	AlphaFold: AF-P54950-F1	No	FMN?
	Nitrilotriacetate monooxygenase component A (P54989)	*Aminobacter aminovorans*	PDB: 3sdo	No	FMN?
	Pristinamycin IIA synthase subunit A (P54991)	*Streptomyces pristinaespiralis*	AlphaFold: AF-P54991-F1	No	FMN?
	Dibenzothiophene-sulfone monooxygenase (Q6WNP3)	*Rhodococcus erythropolis*	PDB: 5TLC	No	FMN
Alkanesulphonate monooxygenase, FMN-dependent (IPR019911)	Alkanesulfonate monooxygenase (A1A9L2)	*Escherichia coli*	PDB: 1M41	No	FMN
Pyrimidine monooxygenase RutA (IPR019914)	Pyrimidine monooxygenase RutA (A1A9R7)	*Escherichia coli*	PDB: 5WAN	No	FMN
TAT-translocated F420-dependent dehydrogenase, FGD2 family (IPR031017)	F420-dependent hydroxymycolic acid dehydrogenase (P96809)	*Mycobacterium tuberculosis*	AlphaFold: AF-P96809-F1	G111-V112	F_{420}
FMNH(2)-dependent dimethylsulfone monooxygenase SfnG (IPR024014)	FMNH(2)-dependent dimethylsulfone monooxygenase (Q65YW9)	*Pseudomonas putida*	AlphaFold: AF-Q65YW9-F1	No	FMN

5,10-methylenetetrahydromethanopterin reductase (IPR019946)	5,10-methylenetetrahydromethanopterin reductase (Q58929)	*Methanocaldococcus jannaschii*	This work	G61-V62	F_{420}
F420-dependent glucose-6-phosphate dehydrogenase (IPR019944)	F420-dependent glucose-6-phosphate dehydrogenase (A0QLV0)	*Mycobacterium avium*	PDB: 3B4Y	S73-V74	F_{420}
F420-dependent glucose-6-phosphate dehydrogenase-related (IPR019945)	Luciferase-like domain-containing protein (F420-dependent alcohol dehydrogenase Afd) (O93734)	*Methanoculleus thermophilus*	PDB: 1RHC	C72-I73	F_{420}

Table S5: Seed sequences for the Superfamily of FAD-linked reductases.

Family name	Seed	Organism
Proline oxidase family (IPR015659)	Hydroxyproline dehydrogenase (A6QQ74)	*Bos taurus*
	Proline dehydrogenase 1 (O32179)	*Bacillus subtilis*
	Proline dehydrogenase 1, mitochondrial (O43272)	*Homo sapiens*
Eukaryotic-type methylenetetrahydrofolate reductase (IPR004621)	Methylenetetrahydrofolate reductase (O80585)	*Arabidopsis thaliana*
	Methylenetetrahydrofolate reductase (P46151)	*Saccharomyces cerevisiae*
	Methylenetetrahydrofolate reductase (P42898)	*Homo sapiens*
5,10-methylenetetrahydrofolate reductase (IPR004620)	5,10-methylenetetrahydrofolate reductase (P0AEZ1)	*Escherichia coli*

References

1. R. Conrad, The global methane cycle: recent advances in understanding the microbial processes involved. *Environ. Microbiol. Rep.* **1**, 285–292 (2009).

2. Z. Lyu, N. Shao, T. Akinyemi, W. B. Whitman, Methanogenesis. *Curr Biol*. **28**, R727–R732 (2018).

3. R. K. Thauer, A.-K. Kaster, H. Seedorf, W. Buckel, R. Hedderich, Methanogenic archaea: ecologically relevant differences in energy conservation. *Nat. Rev. Microbiol.* **6**, 579–591 (2008).

4. J. G. Ferry, Methanosarcina acetivorans: A Model for Mechanistic Understanding of Aceticlastic and Reverse Methanogenesis. *Front. Microbiol.* **11** (2020).

5. J. M. Kurth, H. J. M. Op den Camp, C. U. Welte, Several ways one goal—methanogenesis from unconventional substrates. *Appl. Microbiol. Biotechnol.* **104**, 6839–6854 (2020).

6. C. P. Bueno de Mesquita, D. Wu, S. G. Tringe, Methyl-Based Methanogenesis: an Ecological and Genomic Review. *Microbiol. Mol. Biol. Rev.*, e00024-22 (2023).

7. D. Mayumi, H. Mochimaru, H. Tamaki, K. Yamamoto, H. Yoshioka, Y. Suzuki, Y. Kamagata, S. Sakata, Methane production from coal by a single methanogen. *Science*. **354**, 222–225 (2016).

8. F. Enzmann, F. Mayer, M. Rother, D. Holtmann, Methanogens: biochemical background and biotechnological applications. *AMB Express*. **8**, 1 (2018).

9. L. Jürgensen, E. A. Ehimen, J. Born, J. B. Holm-Nielsen, Dynamic biogas upgrading based on the Sabatier process: Thermodynamic and dynamic process simulation. *Bioresour. Technol.* **178**, 323–329 (2015).

10. G. Borrel, P. S. Adam, S. Gribaldo, Methanogenesis and the Wood–Ljungdahl Pathway: An Ancient, Versatile, and Fragile Association. *Genome Biol. Evol.* **8**, 1706–1711 (2016).

11. Y. Zheng, L. C. Cantley, Toward a better understanding of folate metabolism in health and disease. *J. Exp. Med.* **216**, 253–266 (2018).

12. B. E. Maden, Tetrahydrofolate and tetrahydromethanopterin compared: functionally distinct carriers in C1 metabolism. *Biochem J*. **350 Pt 3**, 609–29 (2000).

13. L. Chistoserdova, J. A. Vorholt, R. K. Thauer, M. E. Lidstrom, C1 Transfer Enzymes and Coenzymes Linking Methylotrophic Bacteria and Methanogenic Archaea. *Science*. **281**, 99–102 (1998).

14. B. Buchenau, R. K. Thauer, Tetrahydrofolate-specific enzymes in Methanosarcina barkeri and growth dependence of this methanogenic archaeon on folic acid or p-aminobenzoic acid. *Arch Microbiol*. **182**, 313–25 (2004).

15. F. L. Sousa, W. F. Martin, Biochemical fossils of the ancient transition from geoenergetics to bioenergetics in prokaryotic one carbon compound metabolism. *Biochim. Biophys. Acta BBA - Bioenerg.* **1837**, 964–981 (2014).

16. S. W. Ragsdale, E. Pierce, Acetogenesis and the Wood–Ljungdahl pathway of CO2 fixation. *Biochim. Biophys. Acta BBA - Proteins Proteomics*. **1784**, 1873–1898 (2008).

17. J. G. Ferry, Acetate Metabolism in Anaerobes from the Domain Archaea. *Life*. **5**, 1454–1471 (2015).

18. J. A. Vorholt, R. K. Thauer, The Active Species of 'CO2' Utilized by Formylmethanofuran Dehydrogenase from Methanogenic Archaea. *Eur. J. Biochem.* **248**, 919–924 (1997).

19. T. Wagner, U. Ermler, S. Shima, The methanogenic CO_2 reducing-and-fixing enzyme is bifunctional and contains 46 [4Fe-4S] clusters. *Science*. **354**, 114–117 (2016).

20. J. Breitung, G. Börner, S. Scholz, D. Linder, K. O. Stetter, R. K. Thauer, Salt dependence, kinetic properties and catalytic mechanism of N-formylmethanofuran:tetrahydromethanopterin formyltransferase from the extreme thermophile Methanopyrus kandleri. *Eur. J. Biochem.* **210**, 971–981 (1992).

21. A. A. DiMarco, M. I. Donnelly, R. S. Wolfe, Purification and properties of the 5,10-methenyltetrahydromethanopterin cyclohydrolase from Methanobacterium thermoautotrophicum. *J. Bacteriol.* **168**, 1372–1377 (1986).

22. B. W. J. te Brömmelstroet, W. J. Geerts, J. T. Keltjens, C. van der Drift, G. D. Vogels, Purification and properties of 5,10-methylenetetrahydromethanopterin dehydrogenase and 5,10-methylenetetrahydromethanopterin reductase, two coenzyme F420-dependent enzymes, from Methanosarcina barkeri. *Biochim. Biophys. Acta BBA - Protein Struct. Mol. Enzymol.* **1079**, 293–302 (1991).

23. C. Zirngibl, W. Van Dongen, B. Schworer, R. Von Bunau, M. Richter, A. Klein, R. K. Thauer, H2-forming methylenetetrahydromethanopterin dehydrogenase, a novel type of hydrogenase without iron-sulfur clusters in methanogenic archaea. *Eur J Biochem*. **208**, 511–20 (1992).

24. R. Grinter, C. Greening, Cofactor F420: an expanded view of its distribution, biosynthesis and roles in bacteria and archaea. *FEMS Microbiol Rev*. **45**, fuab021 (2021).

25. J. A. Fox, D. J. Livingston, W. H. Orme-Johnson, C. T. Walsh, 8-Hydroxy-5-deazaflavin-reducing hydrogenase from Methanobacterium thermoautotrophicum: 1. Purification and characterization. *Biochemistry*. **26**, 4219–4227 (1987).

26. S. Vitt, K. Ma, E. Warkentin, J. Moll, A. J. Pierik, S. Shima, U. Ermler, The F(4)(2)(0)-reducing [NiFe]-hydrogenase complex from Methanothermobacter marburgensis, the first X-ray structure of a group 3 family member. *J Mol Biol*. **426**, 2813–26 (2014).

27. D. J. Mills, S. Vitt, M. Strauss, S. Shima, J. Vonck, De novo modeling of the F(420)-reducing [NiFe]-hydrogenase from a methanogenic archaeon by cryo-electron microscopy. *Elife*. **2**, e00218 (2013).

28. K. Ma, R. K. Thauer, N5, N10-Methylenetetrahydromethanopterin reductase from Methanosarcina barkeri. *FEMS Microbiol. Lett.* **70**, 119–123 (1990).

29. G. Gottschalk, R. K. Thauer, The Na+-translocating methyltransferase complex from methanogenic archaea. *Biochim. Biophys. Acta BBA - Bioenerg.* **1505**, 28–36 (2001).

30. K. Schlegel, V. Müller, Evolution of Na+ and H+ bioenergetics in methanogenic archaea. *Biochem. Soc. Trans.* **41**, 421–426 (2013).

31. R. K. Thauer, Methyl (Alkyl)-Coenzyme M Reductases: Nickel F-430-Containing Enzymes Involved in Anaerobic Methane Formation and in Anaerobic Oxidation of Methane or of Short Chain Alkanes. *Biochemistry*. **58**, 5198–5220 (2019).

32. W. Buckel, R. K. Thauer, Energy conservation via electron bifurcating ferredoxin reduction and proton/Na+ translocating ferredoxin oxidation. *Biochim. Biophys. Acta BBA - Bioenerg.* **1827**, 94–113 (2013).

33. W. Buckel, R. K. Thauer, Flavin-Based Electron Bifurcation, A New Mechanism of Biological Energy Coupling. *Chem. Rev.* **118**, 3862–3886 (2018).

34. T. Wagner, J. Koch, U. Ermler, S. Shima, Methanogenic heterodisulfide reductase (HdrABC-MvhAGD) uses two noncubane [4Fe-4S] clusters for reduction. *Science*. **357**, 699–703 (2017).

35. G. Huang, T. Wagner, U. Ermler, S. Shima, Methanogenesis involves direct hydride transfer from H2 to an organic substrate. *Nat. Rev. Chem.* **4**, 213–221 (2020).

36. S. Shima, G. Huang, T. Wagner, U. Ermler, Structural Basis of Hydrogenotrophic Methanogenesis. *Annu. Rev. Microbiol.* **74**, 713–733 (2020).

37. C. Zirngibl, R. Hedderich, R. K. Thauer, N5,N10-Methylenetetrahydromethanopterin dehydrogenase from Methanobacterium thermoautotrophicum has hydrogenase activity. *FEBS Lett.* **261**, 112–116 (1990).

38. C. Afting, A. Hochheimer, R. K. Thauer, Function of H2-forming methylenetetrahydromethanopterin dehydrogenase from Methanobacterium thermoautotrophicum in coenzyme F420 reduction with H2. *Arch. Microbiol.* **169**, 206–210 (1998).

39. E. L. Hendrickson, J. A. Leigh, Roles of Coenzyme F420-Reducing Hydrogenases and Hydrogen- and F420-Dependent Methylenetetrahydromethanopterin Dehydrogenases in Reduction of F420 and Production of Hydrogen during Methanogenesis. *J. Bacteriol.* **190**, 4818–4821 (2008).

40. T. Hiromoto, K. Ataka, O. Pilak, S. Vogt, M. S. Stagni, W. Meyer-Klaucke, E. Warkentin, R. K. Thauer, S. Shima, U. Ermler, The crystal structure of C176A mutated [Fe]-hydrogenase suggests an acyl-iron ligation in the active site iron complex. *FEBS Lett.* **583**, 585–590 (2009).

41. G. Huang, T. Wagner, M. D. Wodrich, K. Ataka, E. Bill, U. Ermler, X. Hu, S. Shima, The atomic-resolution crystal structure of activated [Fe]-hydrogenase. *Nat. Catal.* **2**, 537–543 (2019).

42. S. Shima, E. J. Lyon, R. K. Thauer, B. Mienert, E. Bill, Mössbauer Studies of the Iron−Sulfur Cluster-Free Hydrogenase: The Electronic State of the Mononuclear Fe Active Site. *J. Am. Chem. Soc.* **127**, 10430–10435 (2005).

43. S. Shima, O. Pilak, S. Vogt, M. Schick, M. S. Stagni, W. Meyer-Klaucke, E. Warkentin, R. K. Thauer, U. Ermler, The Crystal Structure of [Fe]-Hydrogenase Reveals the Geometry of the Active Site. *Science*. **321**, 572–575 (2008).

44. S. Shima, M. Schick, J. Kahnt, K. Ataka, K. Steinbach, U. Linne, Evidence for acyl–iron ligation in the active site of [Fe]-hydrogenase provided by mass spectrometry and infrared spectroscopy. *Dalton Trans*. **41**, 767–771 (2012).

45. B. Schwörer, V. M. Fernandez, C. Zirngibl, R. K. Thauer, H2-forming N5,N10-methylenetetrahydromethanopterin dehydrogenase from Methanobacterium thermoautotrophicum. Studies of the catalytic mechanism of H2 formation using hydrogen isotopes. *Eur. J. Biochem.* **212**, 255–261 (1993).

46. A. Berkessel, Activation of dihydrogen without transition metals. *Curr. Opin. Chem. Biol.* **5**, 486–490 (2001).

47. A. Berkessel, R. K. Thauer, On the Mechanism of Catalysis by a Metal-Free Hydrogenase from Methanogenic Archaea: Enzymatic Transformation of H2 without a Metal and Its Analogy to the Chemistry of Alkanes in Superacidic Solution. *Angew. Chem. Int. Ed. Engl.* **34**, 2247–2250 (1995).

48. R. K. Thauer, A. R. Klein, G. C. Hartmann, Reactions with Molecular Hydrogen in Microorganisms: Evidence for a Purely Organic Hydrogenation Catalyst. *Chem. Rev.* **96**, 3031–3042 (1996).

49. G. A. Olah, N. Hartz, G. Rasul, G. K. S. Prakash, Electrophilic Substitution of Methane Revisited. *J. Am. Chem. Soc.* **117**, 1336–1343 (1995).

50. T. Hiromoto, E. Warkentin, J. Moll, U. Ermler, S. Shima, The crystal structure of an [Fe]-hydrogenase-substrate complex reveals the framework for H2 activation. *Angew Chem Int Ed Engl*. **48**, 6457–60 (2009).

51. H. Tamura, M. Salomone-Stagni, T. Fujishiro, E. Warkentin, W. Meyer-Klaucke, U. Ermler, S. Shima, Crystal structures of [Fe]-hydrogenase in complex with inhibitory isocyanides: implications for the H2-activation site. *Angew Chem Int Ed Engl*. **52**, 9656–9 (2013).

52. S. W. Aufhammer, E. Warkentin, U. Ermler, C. H. Hagemeier, R. K. Thauer, S. Shima, Crystal structure of methylenetetrahydromethanopterin reductase (Mer) in complex with coenzyme F420: Architecture of the F420/FMN binding site of enzymes within the nonprolyl cis-peptide containing bacterial luciferase family. *Protein Sci.* **14**, 1840–1849 (2005).

53. A. A. DiMarco, T. A. Bobik, R. S. Wolfe, Unusual Coenzymes of Methanogenesis. *Annu. Rev. Biochem.* **59**, 355–394 (1990).

54. R. A. Schmitz, D. Linder, K. O. Stetter, R. K. Thauer, N5,N10-Methylenetetrahydromethanopterin reductase (coenzyme F420-dependent) and

formylmethanofuran dehydrogenase from the hyperthermophile Archaeoglobus fulgidus. *Arch. Microbiol.* **156**, 427–434 (1991).

55. S. Shima, E. Warkentin, W. Grabarse, M. Sordel, M. Wicke, R. K. Thauer, U. Ermler, Structure of Coenzyme F420 Dependent Methylenetetrahydromethanopterin Reductase from Two Methanogenic Archaea. *J. Mol. Biol.* **300**, 935–950 (2000).

56. D. V. Miller, M. Ruhlin, W. K. Ray, H. Xu, R. H. White, N(5) ,N(10) -methylenetetrahydromethanopterin reductase from Methanocaldococcus jannaschii also serves as a methylglyoxal reductase. *FEBS Lett*. **591**, 2269–2278 (2017).

57. K. Ma, D. Linder, K. O. Stetter, R. K. Thauer, Purification and properties of N5,N10-methylenetetrahydromethanopterin reductase (coenzyme F420-dependent) from the extreme thermophile Methanopyrus kandleri. *Arch Microbiol*. **155**, 593–600 (1991).

58. K. Ma, R. K. Thauer, Purification and properties of N5, N10-methylenetetrahydromethanopterin reductase from Methanobacterium thermoautotrophicum (strain Marburg). *Eur. J. Biochem.* **191**, 187–193 (1990).

59. B. W. te Brömmelstroet, C. M. Hensgens, J. T. Keltjens, C. van der Drift, G. D. Vogels, Purification and properties of 5,10-methylenetetrahydromethanopterin reductase, a coenzyme F420-dependent enzyme, from Methanobacterium thermoautotrophicum strain delta H. *J. Biol. Chem.* **265**, 1852–1857 (1990).

60. M. Vaupel, R. K. Thauer, Coenzyme F420-Dependent N5,N10-Methylenetetrahydromethanopterin Reductase (Mer) from Methanobacterium Thermoautotrophicum Strain Marburg. *Eur. J. Biochem.* **231**, 773–778 (1995).

61. L. D. Eirich, G. D. Vogels, R. S. Wolfe, Distribution of coenzyme F420 and properties of its hydrolytic fragments. *J. Bacteriol.* **140**, 20–27 (1979).

62. K. Ma, R. K. Thauer, Single step purification of methylenetetrahydromethanopterin reductase fromMethanobacterium thermoautotrophicumby specific binding to Blue Sepharose CL-6B. *FEBS Lett.* **268**, 59–62 (1990).

63. R. k Wierenga, The TIM-barrel fold: a versatile framework for efficient enzymes. *FEBS Lett.* **492**, 193–198 (2001).

64. M. L. Mascotti, M. Juri Ayub, M. W. Fraaije, On the diversity of F420-dependent oxidoreductases: A sequence- and structure-based classification. *Proteins Struct. Funct. Bioinforma.* **89**, 1497–1507 (2021).

65. M. V. Shah, J. Antoney, S. W. Kang, A. C. Warden, C. J. Hartley, H. Nazem-Bokaee, C. J. Jackson, C. Scott, Cofactor F420-Dependent Enzymes: An Under-Explored Resource for Asymmetric Redox Biocatalysis. *Catalysts*. **9**, 868 (2019).

66. A. D. Goldman, J. T. Beatty, L. F. Landweber, The TIM Barrel Architecture Facilitated the Early Evolution of Protein-Mediated Metabolism. *J. Mol. Evol.* **82**, 17–26 (2016).

67. G. N. Ramachandran, A. K. Mitra, An explanation for the rare occurrence of cis peptide units in proteins and polypeptides. *J. Mol. Biol.* **107**, 85–92 (1976).

68. A. Jabs, M. S. Weiss, R. Hilgenfeld, Non-proline Cis peptide bonds in proteins. *J. Mol. Biol.* **286**, 291–304 (1999).

69. D. Pal, P. Chakrabarti, Cis peptide bonds in proteins: residues involved, their conformations, interactions and locations. *J. Mol. Biol.* **294**, 271–288 (1999).

70. T. B. Thompson, J. B. Thoden, T. O. Baldwin, I. Rayment, The 1.5-Å Resolution Crystal Structure of Bacterial Luciferase in Low Salt Conditions. *J. Biol. Chem.* **271**, 21956–21968 (1996).

71. S. W. Aufhammer, E. Warkentin, H. Berk, S. Shima, R. K. Thauer, U. Ermler, Coenzyme Binding in F420-Dependent Secondary Alcohol Dehydrogenase, a Member of the Bacterial Luciferase Family. *Structure*. **12**, 361–370 (2004).

72. G. Bashiri, C. J. Squire, N. J. Moreland, E. N. Baker, Crystal structures of F420-dependent glucose-6-phosphate dehydrogenase FGD1 involved in the activation of the anti-tuberculosis drug candidate PA-824 reveal the basis of coenzyme and substrate binding. *J. Biol. Chem.* **283**, 17531–17541 (2008).

73. L. Li, X. Liu, W. Yang, F. Xu, W. Wang, L. Feng, M. Bartlam, L. Wang, Z. Rao, Crystal Structure of Long-Chain Alkane Monooxygenase (LadA) in Complex with Coenzyme FMN: Unveiling the Long-Chain Alkane Hydroxylase. *J. Mol. Biol.* **376**, 453–465 (2008).

74. H.-Y. Cao, P. Wang, M. Peng, X. Shao, X.-L. Chen, C.-Y. Li, Crystal structure of the dimethylsulfide monooxygenase DmoA from Hyphomicrobium sulfonivorans. *Acta Crystallogr. Sect. F Struct. Biol. Commun.* **74**, 781–786 (2018).

75. M. Okai, W. C. Lee, L.-J. Guan, T. Ohshiro, Y. Izumi, M. Tanokura, Crystal structure of dibenzothiophene sulfone monooxygenase BdsA from Bacillus subtilis WU-S2B. *Proteins Struct. Funct. Bioinforma.* **85**, 1171–1177 (2017).

76. E. Eichhorn, C. A. Davey, D. F. Sargent, T. Leisinger, T. J. Richmond, Crystal Structure of Escherichia coli Alkanesulfonate Monooxygenase SsuD. *J. Mol. Biol.* **324**, 457–468 (2002).

77. T. Mukherjee, Y. Zhang, S. Abdelwahed, S. E. Ealick, T. P. Begley, Catalysis of a Flavoenzyme-Mediated Amide Hydrolysis. *J. Am. Chem. Soc.* **132**, 5550–5551 (2010).

78. Y.-T. Kao, C. Saxena, T.-F. He, L. Guo, L. Wang, A. Sancar, D. Zhong, Ultrafast Dynamics of Flavins in Five Redox States. *J. Am. Chem. Soc.* **130**, 13132–13139 (2008).

79. L. H. Hall, M. L. Bowers, C. N. Durfor, Further consideration of flavin coenzyme biochemistry afforded by geometry-optimized molecular orbital calculations. *Biochemistry*. **26**, 7401–7409 (1987).

80. J. D. Walsh, A.-F. Miller, Flavin reduction potential tuning by substitution and bending. *J. Mol. Struct. THEOCHEM*. **623**, 185–195 (2003).

81. F. Jacobson, C. Walsh, Properties of 7,8-didemethyl-8-hydroxy-5-deazaflavins relevant to redox coenzyme function in methanogen metabolism. *Biochemistry*. **23**, 979–988 (1984).

82. K. Ceh, U. Demmer, E. Warkentin, J. Moll, R. K. Thauer, S. Shima, U. Ermler, Structural Basis of the Hydride Transfer Mechanism in F420-Dependent Methylenetetrahydromethanopterin Dehydrogenase. *Biochemistry*. **48**, 10098–10105 (2009).

83. E. Warkentin, B. Mamat, M. Sordel-Klippert, M. Wicke, R. K. Thauer, M. Iwata, S. Iwata, U. Ermler, S. Shima, Structures of F420H2:NADP+ oxidoreductase with and without its substrates bound. *EMBO J.* **20**, 6561–6569 (2001).

84. C. Öppinger, F. Kremp, V. Müller, Is reduced ferredoxin the physiological electron donor for MetVF-type methylenetetrahydrofolate reductases in acetogenesis? A hypothesis. *Int. Microbiol.* **25**, 75–88 (2022).

85. J. Yi, H. Huang, J. Liang, R. Wang, Z. Liu, F. Li, S. Wang, A Heterodimeric Reduced-Ferredoxin-Dependent Methylenetetrahydrofolate Reductase from Syngas-Fermenting Clostridium ljungdahlii. *Microbiol Spectr*. **9**, e0095821 (2021).

86. S. Sah, K. Lahry, C. Talwar, S. Singh, U. Varshney, Monomeric NADH-Oxidizing Methylenetetrahydrofolate Reductases from Mycobacterium smegmatis Lack Flavin Coenzyme. *J Bacteriol*. **202** (2020), doi:10.1128/JB.00709-19.

87. J. F. Yu, J. T. Xu, S. S. Yang, M. N. Gao, H. R. Si, D. Y. Xiong, J. Gu, Z. L. Wu, J. Zhou, J. Y. Deng, Decreased Methylenetetrahydrofolate Reductase Activity Leads to Increased Sensitivity to para-Aminosalicylic Acid in Mycobacterium tuberculosis. *Antimicrob Agents Chemother*. **66**, e0146521 (2022).

88. J. Bertsch, C. Öppinger, V. Hess, J. D. Langer, V. Müller, Heterotrimeric NADH-Oxidizing Methylenetetrahydrofolate Reductase from the Acetogenic Bacterium Acetobacterium woodii. *J. Bacteriol.* **197**, 1681–1689 (2015).

89. J. E. Clark, L. G. Ljungdahl, Purification and properties of 5,10-methylenetetrahydrofolate reductase, an iron-sulfur flavoprotein from Clostridium formicoaceticum. *J. Biol. Chem.* **259**, 10845–10849 (1984).

90. J. Mock, S. Wang, H. Huang, J. Kahnt, R. K. Thauer, Evidence for a Hexaheteromeric Methylenetetrahydrofolate Reductase in Moorella thermoacetica. *J. Bacteriol.* **196**, 3303–3314 (2014).

91. C. A. Sheppard, E. E. Trimmer, R. G. Matthews, Purification and properties of NADH-dependent 5, 10-methylenetetrahydrofolate reductase (MetF) from Escherichia coli. *J Bacteriol*. **181**, 718–25 (1999).

92. F. T. Hatch, A. R. Larrabee, R. E. Cathou, J. M. Buchanan, Enzymatic synthesis of the methyl group of methionine. I. Identification of the enzymes and cofactors involved in the system isolated from Escherichia coli. *J. Biol. Chem.* **236**, 1095–1101 (1961).

93. D. S. Rosenblatt, "Inherited Disorders of Folate and Cobalamin" in *Homocysteine Metabolism: From Basic Science to Clinical Medicine*, I. Graham, H. Refsum, I. H. Rosenberg, P. M. Ueland, J. M. Shuman, Eds. (Springer US, Boston, MA, 1997), vol. 196 of *Developments in Cardiovascular Medicine*, pp. 61–68.

94. D. S. Froese, B. Fowler, M. R. Baumgartner, Vitamin B12, folate, and the methionine remethylation cycle—biochemistry, pathways, and regulation. *J. Inherit. Metab. Dis.* **42**, 673–685 (2019).

95. Y.-H. Lee, D. Ren, B. Jeon, H. Liu, S-Adenosylmethionine: more than just a methyl donor. *Nat. Prod. Rep.* (2023), doi:10.1039/D2NP00086E.

96. B. M. Hoffman, W. E. Broderick, J. B. Broderick, *Annu. Rev. Biochem.*, in press, doi:10.1146/annurev-biochem-052621-090638.

97. S. Raghubeer, T. E. Matsha, Methylenetetrahydrofolate (MTHFR), the One-Carbon Cycle, and Cardiovascular Risks. *Nutrients*. **13**, 4562 (2021).

98. B. Regland, B. V. Johansson, B. Grenfeldt, L. T. Hjelmgren, M. Medhus, Homocysteinemia is a common feature of schizophrenia. *J. Neural Transm. Gen. Sect. JNT*. **100**, 165–169 (1995).

99. J. L. Mills, Y. J. Lee, M. R. Conley, P. N. Kirke, J. M. McPartlin, D. G. Weir, J. M. Scott, Homocysteine metabolism in pregnancies complicated by neural-tube defects. *The Lancet*. **345**, 149–151 (1995).

100. I. M. Graham, Plasma Homocysteine as a Risk Factor for Vascular Disease: The European Concerted Action Project. *JAMA*. **277**, 1775 (1997).

101. A. G. Bostom, B. F. Culleton, Hyperhomocysteinemia in Chronic Renal Disease. *J. Am. Soc. Nephrol.* **10**, 891 (1999).

102. J. W. Eikelboom, E. Lonn, J. Genest, G. Hankey, S. Yusuf, Homocyst(e)ine and Cardiovascular Disease: A Critical Review of the Epidemiologic Evidence. *Ann. Intern. Med.* **131**, 363–375 (1999).

103. J. G. Ray, C. A. Laskin, Folic Acid and Homocyst(e)ine Metabolic Defects and the Risk of Placental Abruption, Pre-eclampsia and Spontaneous Pregnancy Loss: A Systematic Review. *Placenta*. **20**, 519–529 (1999).

104. T. Bottiglieri, M. Laundy, R. Crellin, B. K. Toone, M. W. P. Carney, E. H. Reynolds, Homocysteine, folate, methylation, and monoamine metabolism in depression. *J. Neurol. Neurosurg. Psychiatry*. **69**, 228–232 (2000).

105. B. Schwahn, R. Rozen, Polymorphisms in the Methylenetetrahydrofolate Reductase Gene. *Am. J. Pharmacogenomics*. **1**, 189–201 (2001).

106. B. C. Schwahn, Z. Chen, M. D. Laryea, U. Wendel, S. Lussier-Cacan, J. Genest, M. Mar, S. H. Zeisel, C. Castro, T. Garrow, R. Rozen, Homocysteine-betaine interactions in a murine model of 5,10-methylenetetrahydrofolate reductase deficiency. *FASEB J.* **17**, 1–25 (2003).

107. P. Burda, A. Schäfer, T. Suormala, T. Rummel, C. Bürer, D. Heuberger, M. Frapolli, C. Giunta, J. Sokolová, H. Vlášková, V. Kožich, H. G. Koch, B. Fowler, D. S. Froese, M. R. Baumgartner, Insights into Severe 5,10-Methylenetetrahydrofolate Reductase Deficiency: Molecular Genetic and Enzymatic Characterization of 76 Patients. *Hum. Mutat.* **36**, 611–621 (2015).

108. G. S. Ducker, J. D. Rabinowitz, One-Carbon Metabolism in Health and Disease. *Cell Metab.* **25**, 27–42 (2017).

109. E. E. Trimmer, D. P. Ballou, R. G. Matthews, Methylenetetrahydrofolate reductase from Escherichia coli: elucidation of the kinetic mechanism by steady-state and rapid-reaction studies. *Biochemistry*. **40**, 6205–15 (2001).

110. S. Igari, A. Ohtaki, Y. Yamanaka, Y. Sato, M. Yohda, M. Odaka, K. Noguchi, K. Yamada, Properties and crystal structure of methylenetetrahydrofolate reductase from Thermus thermophilus HB8. *PLoS One*. **6**, e23716 (2011).

111. G. Wohlfarth, G. Diekert, Thermodynamics of methylenetetrahydrofolate reduction to methyltetrahydrofolate and its implications for the energy metabolism of homoacetogenic bacteria. *Arch. Microbiol.* **155** (1991), doi:10.1007/bf00243458.

112. J. S. Sumner, R. G. Matthews, Stereochemistry and mechanism of hydrogen transfer between NADPH and methylenetetrahydrofolate in the reaction catalyzed by methylenetetrahydrofolate reductase from pig liver. *J. Am. Chem. Soc.* **114**, 6949–6956 (1992).

113. R. G. Kallen, W. P. Jencks, The Mechanism of the Condensation of Formaldehyde with Tetrahydrofolic Acid. *J. Biol. Chem.* **241**, 5851–5863 (1966).

114. K. M. Perry, C. W. Carreras, L. C. Chang, D. V. Santi, R. M. Stroud, Structures of thymidylate synthase with a C-terminal deletion: Role of the C-terminus in alignment of 2'-deoxyuridine 5'-monophosphate and 5,10-methylenetetrahydrofolate. *Biochemistry*. **32**, 7116–7125 (1993).

115. S. Roje, H. Wang, S. D. McNeil, R. K. Raymond, D. R. Appling, Y. Shachar-Hill, H. J. Bohnert, A. D. Hanson, Isolation, Characterization, and Functional Expression of cDNAs Encoding NADH-dependent Methylenetetrahydrofolate Reductase from Higher Plants *. *J. Biol. Chem.* **274**, 36089–36096 (1999).

116. R. K. Raymond, E. K. Kastanos, D. R. Appling, Saccharomyces cerevisiae expresses two genes encoding isozymes of methylenetetrahydrofolate reductase. *Arch. Biochem. Biophys.* **372**, 300–308 (1999).

117. P. Goyette, J. S. Sumner, R. Milos, A. M. V. Duncan, D. S. Rosenblatt, R. G. Matthews, R. Rozen, Human methylenetetrahydrofolate reductase: isolation of cDNA, mapping and mutation identification. *Nat. Genet.* **7**, 195–200 (1994).

118. B. D. Guenther, C. A. Sheppard, P. Tran, R. Rozen, R. G. Matthews, M. L. Ludwig, The structure and properties of methylenetetrahydrofolate reductase from Escherichia coli suggest how folate ameliorates human hyperhomocysteinemia. *Nat. Struct. Biol.* **6**, 359–365 (1999).

119. D. S. Froese, J. Kopec, E. Rembeza, G. A. Bezerra, A. E. Oberholzer, T. Suormala, S. Lutz, R. Chalk, O. Borkowska, M. R. Baumgartner, W. W. Yue, Structural basis for the regulation of human 5,10-methylenetetrahydrofolate reductase by phosphorylation and S-adenosylmethionine inhibition. *Nat. Commun.* **9**, 2261 (2018).

120. K. Yamada, J. Mendoza, M. Koutmos, 5-Formyltetrahydrofolate promotes conformational remodeling in a methylenetetrahydrofolate reductase active site and inhibits its activity. *J. Biol. Chem.* **299**, 102855 (2023).

121. R. Pejchal, R. Sargeant, M. L. Ludwig, Structures of NADH and CH3-H4folate complexes of Escherichia coli methylenetetrahydrofolate reductase reveal a spartan strategy for a ping-pong reaction. *Biochemistry*. **44**, 11447–57 (2005).

122. E. E. Trimmer, D. P. Ballou, M. L. Ludwig, R. G. Matthews, Folate activation and catalysis in methylenetetrahydrofolate reductase from Escherichia coli: roles for aspartate 120 and glutamate 28. *Biochemistry*. **40**, 6216–26 (2001).

123. G. Wohlfarth, G. Geerligs, G. Diekert, Purification and properties of a NADH-dependent 5,10-methylenetetrahydrofolate reductase from Peptostreptococcus productus. *Eur J Biochem*. **192**, 411–7 (1990).

124. D. B. Young, I. Comas, L. P. de Carvalho, Phylogenetic analysis of vitamin B12-related metabolism in Mycobacterium tuberculosis. *Front Mol Biosci*. **2**, 6 (2015).

125. C. J. L. Murray, K. S. Ikuta, F. Sharara, L. Swetschinski, G. Robles Aguilar, A. Gray, C. Han, C. Bisignano, P. Rao, E. Wool, S. C. Johnson, A. J. Browne, M. G. Chipeta, F. Fell, S. Hackett, G. Haines-Woodhouse, B. H. Kashef Hamadani, E. A. P. Kumaran, B. McManigal, S. Achalapong, R. Agarwal, S. Akech, S. Albertson, J. Amuasi, J. Andrews, A. Aravkin, E. Ashley, F.-X. Babin, F. Bailey, S. Baker, B. Basnyat, A. Bekker, R. Bender, J. A. Berkley, A. Bethou, J. Bielicki, S. Boonkasidecha, J. Bukosia, C. Carvalheiro, C. Castañeda-Orjuela, V. Chansamouth, S. Chaurasia, S. Chiurchiù, F. Chowdhury, R. Clotaire Donatien, A. J. Cook, B. Cooper, T. R. Cressey, E. Criollo-Mora, M. Cunningham, S. Darboe, N. P. J. Day, M. De Luca, K. Dokova, A. Dramowski, S. J. Dunachie, T. Duong Bich, T. Eckmanns, D. Eibach, A. Emami, N. Feasey, N. Fisher-Pearson, K. Forrest, C. Garcia, D. Garrett, P. Gastmeier, A. Z. Giref, R. C. Greer, V. Gupta, S. Haller, A. Haselbeck, S. I. Hay, M. Holm, S. Hopkins, Y. Hsia, K. C. Iregbu, J. Jacobs, D. Jarovsky, F. Javanmardi, A. W. J. Jenney, M. Khorana, S. Khusuwan, N. Kissoon, E. Kobeissi, T. Kostyanev, F. Krapp, R. Krumkamp, A. Kumar, H. H. Kyu, C. Lim, K. Lim, D. Limmathurotsakul, M. J. Loftus, M. Lunn, J. Ma, A. Manoharan, F. Marks, J. May, M. Mayxay, N. Mturi, T. Munera-Huertas, P. Musicha, L. A. Musila, M. M. Mussi-Pinhata, R. N. Naidu, T. Nakamura, R. Nanavati, S. Nangia, P. Newton, C. Ngoun, A. Novotney, D. Nwakanma, C. W. Obiero, T. J. Ochoa, A. Olivas-Martinez, P. Olliaro, E. Ooko, E. Ortiz-Brizuela, P. Ounchanum, G. D. Pak, J. L. Paredes, A. Y. Peleg, C. Perrone, T. Phe, K. Phommasone, N. Plakkal, A. Ponce-de-Leon, M. Raad, T. Ramdin, S. Rattanavong, A. Riddell, T. Roberts, J. V. Robotham, A. Roca, V. D. Rosenthal, K. E. Rudd, N. Russell, H. S. Sader, W. Saengchan, J. Schnall, J. A. G. Scott, S. Seekaew, M. Sharland, M. Shivamallappa, J. Sifuentes-Osornio, A. J. Simpson, N. Steenkeste, A. J. Stewardson, T. Stoeva, N. Tasak, A. Thaiprakong, G. Thwaites, C. Tigoi, C. Turner, P. Turner, H. R. Van Doorn, S. Velaphi, A. Vongpradith, M. Vongsouvath, H. Vu, T. Walsh, J. L. Walson, S. Waner, T. Wangrangsimakul, P. Wannapinij, T. Wozniak, T. E. M. W. Young Sharma, K. C. Yu, P. Zheng, B. Sartorius, A. D. Lopez, A. Stergachis, C. Moore, C. Dolecek, M. Naghavi, Global burden of bacterial antimicrobial resistance in 2019: a systematic analysis. *The Lancet*. **399**, 629–655 (2022).

126. J. Chakaya, M. Khan, F. Ntoumi, E. Aklillu, R. Fatima, P. Mwaba, N. Kapata, S. Mfinanga, S. E. Hasnain, P. Katoto, A. N. H. Bulabula, N. A. Sam-Agudu, J. B. Nachega,

S. Tiberi, T. D. McHugh, I. Abubakar, A. Zumla, Global Tuberculosis Report 2020 - Reflections on the Global TB burden, treatment and prevention efforts. *Int J Infect Dis*. **113 Suppl 1**, S7–S12 (2021).

127. E. J. Lyon, S. Shima, R. Boecher, R. K. Thauer, F. W. Grevels, E. Bill, W. Roseboom, S. P. Albracht, Carbon monoxide as an intrinsic ligand to iron in the active site of the iron-sulfur-cluster-free hydrogenase H2-forming methylenetetrahydromethanopterin dehydrogenase as revealed by infrared spectroscopy. *J Am Chem Soc*. **126**, 14239–48 (2004).

128. O. Pilak, B. Mamat, S. Vogt, C. H. Hagemeier, R. K. Thauer, S. Shima, C. Vonrhein, E. Warkentin, U. Ermler, The Crystal Structure of the Apoenzyme of the Iron–Sulphur Cluster-free Hydrogenase. *J. Mol. Biol.* **358**, 798–809 (2006).

129. M. Korbas, S. Vogt, W. Meyer-Klaucke, E. Bill, E. J. Lyon, R. K. Thauer, S. Shima, The iron-sulfur cluster-free hydrogenase (Hmd) is a metalloenzyme with a novel iron binding motif. *J Biol Chem*. **281**, 30804–13 (2006).

130. J. Schleucher, C. Griesinger, B. Schwoerer, R. K. Thauer, H2-Forming N5,N10-Methylenetetrahydromethanopterin Dehydrogenase from Methanobacterium thermoautotrophicum Catalyzes a Stereoselective Hydride Transfer As Determined by Two-Dimensional NMR Spectroscopy. *Biochemistry*. **33**, 3986–3993 (1994).

131. J. Schleucher, B. Schwoerer, R. K. Thauer, C. Griesinger, Elucidation of the Stereochemical Course of Chemical Reactions by Magnetic Labeling. *J. Am. Chem. Soc.* **117**, 2941–2942 (1995).

132. S. B. Duckett, R. E. Mewis, Application of Parahydrogen Induced Polarization Techniques in NMR Spectroscopy and Imaging. *Acc. Chem. Res.* **45**, 1247–1257 (2012).

133. D. O. Zakharov, K. Chernichenko, K. Sorochkina, S. Yang, V.-V. Telkki, T. Repo, V. V. Zhivonitko, Parahydrogen-Induced Polarization in Hydrogenation Reactions Mediated by a Metal-Free Catalyst. *Chem. – Eur. J.* **28**, e202103501 (2022).

134. A. S. Kiryutin, G. Sauer, A. V. Yurkovskaya, H.-H. Limbach, K. L. Ivanov, G. Buntkowsky, Parahydrogen Allows Ultrasensitive Indirect NMR Detection of Catalytic Hydrogen Complexes. *J. Phys. Chem. C*. **121**, 9879–9888 (2017).

135. L. Kaltschnee, A. N. Pravdivtsev, M. Gehl, G. Huang, G. L. Stoychev, C. Riplinger, M. Keitel, F. Neese, J.-B. Hövener, A. A. Auer, C. Griesinger, S. Shima, S. Glöggler, Sensitivity-enhanced magnetic resonance reveals hydrogen intermediates during active [Fe]-hydrogenase catalysis (2023), p. 2023.05.10.540199, , doi:10.1101/2023.05.10.540199.

136. M. Ferrer, T. N. Chernikova, M. M. Yakimov, P. N. Golyshin, K. N. Timmis, Chaperonins govern growth of Escherichia coli at low temperatures. *Nat. Biotechnol.* **21**, 1266–1267 (2003).

137. G. K. Farber, G. A. Petsko, The evolution of α/β barrel enzymes. *Trends Biochem. Sci.* **15**, 228–234 (1990).

138. H. Seedorf, J. Kahnt, A. J. Pierik, R. K. Thauer, Si-face stereospecificity at C5 of coenzyme F420 for F420H2 oxidase from methanogenic Archaea as determined by mass spectrometry. *FEBS J.* **272**, 5337–5342 (2005).

139. J. Kunow, B. Schwörer, K. O. Stetter, R. K. Thauer, A F420-dependent NADP reductase in the extremely thermophilic sulfate-reducing Archaeoglobus fulgidus. *Arch. Microbiol.* **160**, 199–205 (1993).

140. A. R. Klein, H. Berk, E. Purwantini, L. Daniels, R. K. Thauer, Si-Face Stereospecificity at C5 of Coenzyme F420 for F420-Dependent Glucose-6-Phosphate Dehydrogenase from Mycobacterium smegmatis and F420-Dependent Alcohol Dehydrogenase from Methanoculleus thermophilicus. *Eur. J. Biochem.* **239**, 93–97 (1996).

141. A. R. Klein, R. K. Thauer, Re-Face Specificity at C14a of Methylenetetrahydromethanopterin and Si-Face Specificity at C5 of Coenzyme F420 for Coenzyme F420-Dependent Methylenetetrahydromethanopterin Dehydrogenase from Methanogenic Archaea. *Eur. J. Biochem.* **227**, 169–174 (1995).

142. N. L. Schauer, J. G. Ferry, J. F. Honek, W. H. Orme-Johnson, C. Walsh, Mechanistic studies of the coenzyme F420-reducing formate dehydrogenase from Methanobacterium formicicum. *Biochemistry*. **25**, 7163–7168 (1986).

143. S. Yamazaki, L. Tsai, T. C. Stadtman, F. S. Jacobson, C. Walsh, Stereochemical studies of 8-hydroxy-5-deazaflavin-dependent NADP+ reductase from Methanococcus vannielii. *J. Biol. Chem.* **255**, 9025–9027 (1980).

144. J. Kunow, B. Schwörer, E. Setzke, R. K. Thauer, Si-face stereospecificity at C5 of coenzyme F420 for F420-dependent N5,N10-methylenetetrahydromethanopterin dehydrogenase, F420-dependent N5,N10-methylenetetrahydromethanopterin reductase and F420H2:dimethylnaphthoquinone oxidoreductase. *Eur. J. Biochem.* **214**, 641–646 (1993).

145. D. J. Creighton, N. S. R. K. Murthy, Stereochemistry of Enzyme-Catalyzed Reactions at Carbon. *The Enzymes*. **19**, 323–421 (1990).

146. K. Schöning-Stierand, K. Diedrich, R. Fährrolfes, F. Flachsenberg, A. Meyder, E. Nittinger, R. Steinegger, M. Rarey, ProteinsPlus: interactive analysis of protein–ligand binding interfaces. *Nucleic Acids Res.* **48**, W48–W53 (2020).

147. K. Stierand, P. C. Maaß, M. Rarey, Molecular complexes at a glance: automated generation of two-dimensional complex diagrams. *Bioinformatics*. **22**, 1710–1716 (2006).

148. J. Jumper, R. Evans, A. Pritzel, T. Green, M. Figurnov, O. Ronneberger, K. Tunyasuvunakool, R. Bates, A. Žídek, A. Potapenko, A. Bridgland, C. Meyer, S. A. A. Kohl, A. J. Ballard, A. Cowie, B. Romera-Paredes, S. Nikolov, R. Jain, J. Adler, T. Back, S. Petersen, D. Reiman, E. Clancy, M. Zielinski, M. Steinegger, M. Pacholska, T. Berghammer, S. Bodenstein, D. Silver, O. Vinyals, A. W. Senior, K. Kavukcuoglu, P. Kohli, D. Hassabis, Highly accurate protein structure prediction with AlphaFold. *Nature*. **596**, 583–589 (2021).

149. L. M. Mayr, D. Willbold, P. Rösch, F. X. Schmid, Generation of a Non-prolyl cis Peptide Bond in Ribonuclease T1. *J. Mol. Biol.* **240**, 288–293 (1994).

150. K. H. Schröder, L. Naumann, R. M. Kroppenstedt, U. Reischl, Mycobacterium hassiacum sp. nov., a new rapidly growing thermophilic mycobacterium. *Int J Syst Bacteriol*. **47**, 86–91 (1997).

151. I. Tiago, A. Maranha, V. Mendes, S. Alarico, P. J. Moynihan, A. J. Clarke, S. Macedo-Ribeiro, P. J. B. Pereira, N. Empadinhas, Genome Sequence of Mycobacterium hassiacum DSM 44199, a Rare Source of Heat-Stable Mycobacterial Proteins. *J. Bacteriol.* **194**, 7010–7011 (2012).

152. M. Gehl, U. Demmer, U. Ermler, S. Shima, *Proteins Struct. Funct. Bioinforma.*, in press, doi:10.1002/prot.26504.

153. E. E. Trimmer, D. P. Ballou, L. J. Galloway, S. A. Scannell, D. R. Brinker, K. R. Casas, Aspartate 120 of Escherichia coli methylenetetrahydrofolate reductase: evidence for major roles in folate binding and catalysis and a minor role in flavin reactivity. *Biochemistry*. **44**, 6809–22 (2005).

154. R. G. Matthews, Methylenetetrahydrofolate reductase from pig liver. *Methods Enzymol.* **122**, 372–381 (1986).

155. A. N. Unissa, S. Subbian, L. E. Hanna, N. Selvakumar, Overview on mechanisms of isoniazid action and resistance in Mycobacterium tuberculosis. *Infect. Genet. Evol.* **45**, 474–492 (2016).

156. A. D. Bendre, P. J. Peters, J. Kumar, Tuberculosis: Past, present and future of the treatment and drug discovery research. *Curr Res Pharmacol Drug Discov*. **2**, 100037 (2021).

157. S. Thee, A. J. Garcia-Prats, P. R. Donald, A. C. Hesseling, H. S. Schaaf, A review of the use of ethionamide and prothionamide in childhood tuberculosis. *Tuberculosis*. **97**, 126–136 (2016).

158. T. Paysan-Lafosse, M. Blum, S. Chuguransky, T. Grego, B. L. Pinto, G. A. Salazar, M. L. Bileschi, P. Bork, A. Bridge, L. Colwell, J. Gough, D. H. Haft, I. Letunić, A. Marchler-Bauer, H. Mi, D. A. Natale, C. A. Orengo, A. P. Pandurangan, C. Rivoire, C. J. A. Sigrist, I. Sillitoe, N. Thanki, P. D. Thomas, S. C. E. Tosatto, C. H. Wu, A. Bateman, InterPro in 2022. *Nucleic Acids Res.* **51**, D418–D427 (2023).

159. M. N. Lee, D. Takawira, A. P. Nikolova, D. P. Ballou, V. C. Furtado, N. L. Phung, B. R. Still, M. K. Thorstad, J. J. Tanner, E. E. Trimmer, Functional role for the conformationally mobile phenylalanine 223 in the reaction of methylenetetrahydrofolate reductase from Escherichia coli. *Biochemistry*. **48**, 7673–85 (2009).

160. Y. Harpaz, M. Gerstein, C. Chothia, Volume changes on protein folding. *Structure*. **2**, 641–649 (1994).

161. C. Zuo, A. L. Jolly, A. P. Nikolova, D. I. Satzer, S. Cao, J. S. Sanchez, D. P. Ballou, E. E. Trimmer, A role for glutamine 183 in the folate oxidative half-reaction of

methylenetetrahydrofolate reductase from Escherichia coli. *Arch Biochem Biophys*. **642**, 63–74 (2018).

162. G. Xu, G. J. Poelarends, Unlocking New Reactivities in Enzymes by Iminium Catalysis. *Angew. Chem. Int. Ed.* **61**, e202203613 (2022).

163. P. Acharya, M. Goenrich, C. H. Hagemeier, U. Demmer, J. A. Vorholt, R. K. Thauer, U. Ermler, How an Enzyme Binds the C1 Carrier Tetrahydromethanopterin: Structure of the Tetrahydromethanopterin-dependent Formaldehyde-activating Enzyme (Fae) from Methylobacterium Extorquens AM1. *J. Biol. Chem.* **280**, 13712–13719 (2005).

164. J. A. Vorholt, C. J. Marx, M. E. Lidstrom, R. K. Thauer, Novel Formaldehyde-Activating Enzyme in Methylobacterium extorquens AM1 Required for Growth on Methanol. *J. Bacteriol.* **182**, 6645–6650 (2000).

165. J. S. Finer-Moore, D. V. Santi, R. M. Stroud, Lessons and Conclusions from Dissecting the Mechanism of a Bisubstrate Enzyme: Thymidylate Synthase Mutagenesis, Function, and Structure. *Biochemistry*. **42**, 248–256 (2003).

166. V. Trivedi, A. Gupta, V. R. Jala, P. Saravanan, G. S. J. Rao, N. A. Rao, H. S. Savithri, H. S. Subramanya, Crystal Structure of Binary and Ternary Complexes of Serine Hydroxymethyltransferase from Bacillus stearothermophilus: Insights into the Catalytic Mechanism. *J. Biol. Chem.* **277**, 17161–17169 (2002).

167. J. V. K. Rao, V. Prakash, N. A. Rao, H. S. Savithri, The role of Glu74 and Tyr82 in the reaction catalyzed by sheep liver cytosolic serine hydroxymethyltransferase. *Eur. J. Biochem.* **267**, 5967–5976 (2000).

168. R. C. Edgar, MUSCLE: multiple sequence alignment with high accuracy and high throughput. *Nucleic Acids Res*. **32**, 1792–7 (2004).

169. B. Q. Minh, H. A. Schmidt, O. Chernomor, D. Schrempf, M. D. Woodhams, A. von Haeseler, R. Lanfear, IQ-TREE 2: New Models and Efficient Methods for Phylogenetic Inference in the Genomic Era. *Mol. Biol. Evol.* **37**, 1530–1534 (2020).

170. D. T. Hoang, O. Chernomor, A. von Haeseler, B. Q. Minh, L. S. Vinh, UFBoot2: Improving the Ultrafast Bootstrap Approximation. *Mol. Biol. Evol.* **35**, 518–522 (2018).

171. V. de Crécy-Lagard, G. Phillips, L. L. Grochowski, B. E. Yacoubi, F. Jenney, M. W. W. Adams, A. G. Murzin, R. H. White, Comparative Genomics Guided Discovery of Two Missing Archaeal Enzyme Families Involved in the Biosynthesis of the Pterin Moiety of Tetrahydromethanopterin and Tetrahydrofolate. *ACS Chem. Biol.* **7**, 1807–1816 (2012).

172. W. Martin, M. J. Russell, On the origin of biochemistry at an alkaline hydrothermal vent. *Philos. Trans. R. Soc. B Biol. Sci.* **362**, 1887–1926 (2006).

173. P. S. Adam, G. Borrel, S. Gribaldo, An archaeal origin of the Wood–Ljungdahl H4MPT branch and the emergence of bacterial methylotrophy. *Nat. Microbiol.* **4**, 2155–2163 (2019).

174. A. Poehlein, S. Schmidt, A.-K. Kaster, M. Goenrich, J. Vollmers, A. Thürmer, J. Bertsch, K. Schuchmann, B. Voigt, M. Hecker, R. Daniel, R. K. Thauer, G. Gottschalk, V. Müller,

An Ancient Pathway Combining Carbon Dioxide Fixation with the Generation and Utilization of a Sodium Ion Gradient for ATP Synthesis. *PLOS ONE*. **7**, e33439 (2012).

175. G. Buurman, S. Shima, R. K. Thauer, The metal-free hydrogenase from methanogenic archaea: evidence for a bound cofactor. *FEBS Lett.* **485**, 200–204 (2000).

176. W. Kabsch, XDS. *Acta Crystallogr. Sect. D*. **66**, 125–132 (2010).

177. A. J. McCoy, R. W. Grosse-Kunstleve, P. D. Adams, M. D. Winn, L. C. Storoni, R. J. Read, Phaser crystallographic software. *J. Appl. Crystallogr.* **40**, 658–674 (2007).

178. P. Emsley, B. Lohkamp, W. G. Scott, K. Cowtan, Features and development of Coot. *Acta Crystallogr Biol Crystallogr*. **66**, 486–501 (2010).

179. D. Liebschner, P. V. Afonine, M. L. Baker, G. Bunkoczi, V. B. Chen, T. I. Croll, B. Hintze, L.-W. Hung, S. Jain, A. J. McCoy, N. W. Moriarty, R. D. Oeffner, B. K. Poon, M. G. Prisant, R. J. Read, J. S. Richardson, D. C. Richardson, M. D. Sammito, O. V. Sobolev, D. H. Stockwell, T. C. Terwilliger, A. G. Urzhumtsev, L. L. Videau, C. J. Williams, P. D. Adams, Macromolecular structure determination using X-rays, neutrons and electrons: recent developments in Phenix. *Acta Crystallogr. Sect. D*. **75**, 861–877 (2019).

180. G. N. Murshudov, P. Skubak, A. A. Lebedev, N. S. Pannu, R. A. Steiner, R. A. Nicholls, M. D. Winn, F. Long, A. A. Vagin, REFMAC5 for the refinement of macromolecular crystal structures. *Acta Crystallogr. Sect. D*. **67**, 355–367 (2011).

181. C. J. Williams, J. J. Headd, N. W. Moriarty, M. G. Prisant, L. L. Videau, L. N. Deis, V. Verma, D. A. Keedy, B. J. Hintze, V. B. Chen, S. Jain, S. M. Lewis, W. B. Arendall, J. Snoeyink, P. D. Adams, S. C. Lovell, J. S. Richardson, D. C. Richardson, MolProbity: More and better reference data for improved all-atom structure validation. *Protein Sci*. **27**, 293–315 (2018).

182. M. Mirdita, K. Schütze, Y. Moriwaki, L. Heo, S. Ovchinnikov, M. Steinegger, *bioRxiv*, in press, doi:10.1101/2021.08.15.456425.

183. M. D. Winn, C. C. Ballard, K. D. Cowtan, E. J. Dodson, P. Emsley, P. R. Evans, R. M. Keegan, E. B. Krissinel, A. G. W. Leslie, A. McCoy, S. J. McNicholas, G. N. Murshudov, N. S. Pannu, E. A. Potterton, H. R. Powell, R. J. Read, A. Vagin, K. S. Wilson, Overview of the CCP4 suite and current developments. *Acta Crystallogr. Sect. D*. **67**, 235–242 (2011).

184. T. Kluyver, B. Ragan-Kelley, F. Pérez, B. E. Granger, M. Bussonnier, J. Frederic, K. Kelley, J. B. Hamrick, J. Grout, S. Corlay, Jupyter Notebooks-a publishing format for reproducible computational workflows. **2016** (2016).

185. W. McKinney, "Data Structures for Statistical Computing in Python" in (Austin, Texas, 2010; https://conference.scipy.org/proceedings/scipy2010/mckinney.html), pp. 56–61.

186. M. L. Waskom, Seaborn: statistical data visualization. *J. Open Source Softw.* **6**, 3021 (2021).

187. J. D. Hunter, Matplotlib: A 2D Graphics Environment. *Comput. Sci. Eng.* **9**, 90–95 (2007).

188. C. R. Harris, K. J. Millman, S. J. Van Der Walt, R. Gommers, P. Virtanen, D. Cournapeau, E. Wieser, J. Taylor, S. Berg, N. J. Smith, Array programming with NumPy. *Nature*. **585**, 357–362 (2020).

189. P. Virtanen, R. Gommers, T. E. Oliphant, M. Haberland, T. Reddy, D. Cournapeau, E. Burovski, P. Peterson, W. Weckesser, J. Bright, S. J. van der Walt, M. Brett, J. Wilson, K. J. Millman, N. Mayorov, A. R. J. Nelson, E. Jones, R. Kern, E. Larson, C. J. Carey, İ. Polat, Y. Feng, E. W. Moore, J. VanderPlas, D. Laxalde, J. Perktold, R. Cimrman, I. Henriksen, E. A. Quintero, C. R. Harris, A. M. Archibald, A. H. Ribeiro, F. Pedregosa, P. van Mulbregt, SciPy 1.0 Contributors, A. Vijaykumar, A. P. Bardelli, A. Rothberg, A. Hilboll, A. Kloeckner, A. Scopatz, A. Lee, A. Rokem, C. N. Woods, C. Fulton, C. Masson, C. Häggström, C. Fitzgerald, D. A. Nicholson, D. R. Hagen, D. V. Pasechnik, E. Olivetti, E. Martin, E. Wieser, F. Silva, F. Lenders, F. Wilhelm, G. Young, G. A. Price, G.-L. Ingold, G. E. Allen, G. R. Lee, H. Audren, I. Probst, J. P. Dietrich, J. Silterra, J. T. Webber, J. Slavič, J. Nothman, J. Buchner, J. Kulick, J. L. Schönberger, J. V. de Miranda Cardoso, J. Reimer, J. Harrington, J. L. C. Rodríguez, J. Nunez-Iglesias, J. Kuczynski, K. Tritz, M. Thoma, M. Newville, M. Kümmerer, M. Bolingbroke, M. Tartre, M. Pak, N. J. Smith, N. Nowaczyk, N. Shebanov, O. Pavlyk, P. A. Brodtkorb, P. Lee, R. T. McGibbon, R. Feldbauer, S. Lewis, S. Tygier, S. Sievert, S. Vigna, S. Peterson, S. More, T. Pudlik, T. Oshima, T. J. Pingel, T. P. Robitaille, T. Spura, T. R. Jones, T. Cera, T. Leslie, T. Zito, T. Krauss, U. Upadhyay, Y. O. Halchenko, Y. Vázquez-Baeza, SciPy 1.0: fundamental algorithms for scientific computing in Python. *Nat. Methods*. **17**, 261–272 (2020).

190. Y. Liu, X. Yang, J. Gan, S. Chen, Z.-X. Xiao, Y. Cao, CB-Dock2: improved protein–ligand blind docking by integrating cavity detection, docking and homologous template fitting. *Nucleic Acids Res.* **50**, W159–W164 (2022).

191. J. Eberhardt, D. Santos-Martins, A. F. Tillack, S. Forli, AutoDock Vina 1.2.0: New Docking Methods, Expanded Force Field, and Python Bindings. *J. Chem. Inf. Model.* **61**, 3891–3898 (2021).

192. M. S. Valdés-Tresanco, M. E. Valdés-Tresanco, P. A. Valiente, E. Moreno, AMDock: a versatile graphical tool for assisting molecular docking with Autodock Vina and Autodock4. *Biol. Direct*. **15**, 12 (2020).

193. I. Letunic, P. Bork, Interactive Tree Of Life (iTOL) v5: an online tool for phylogenetic tree display and annotation. *Nucleic Acids Res.* **49**, W293–W296 (2021).

Acknowledgement

Curriculum vitae

Erklärung

Ich versichere, dass ich meine Dissertation mit dem Titel „Towards the Extension of the Substrate Spectrum of the [Fe]-Hydrogenase Hmd“ selbstständig ohne unerlaubte Hilfe angefertigt und mich dabei keiner anderen als der von mir ausdrücklich bezeichneten Quellen und Hilfsmittel bedient habe.

Diese Dissertation wurde in der jetzigen oder einer ähnlichen Form noch bei keiner anderen Hochschule eingereicht und hat noch keinen sonstigen Prüfungszwecken gedient.

Marburg, den 23.05.2023

Manuel Gehl